Development and Validation of Vascular Image Processing Techniques for Image-Guided Neurovascular Surgery

Sean Jy-Shyang Chen

Doctor of Philosophy

Department of Biomedical Engineering

McGill University

Montreal, Quebec, Canada

November 21, 2013

A thesis submitted to McGill University in partial fulfillment of the requirements of the degree of Doctor of Philosophy

DEDICATION

This thesis is dedicated to everyone, everything, and any event that helped in its creation.

ACKNOWLEDGEMENTS

In regards to the work in this thesis, I would like to acknowledge:

- Dr. D. Louis Collins: *For serving as my PhD supervisor, and providing advice and support in all aspects of this work.*
- Dr. Christian Barillot and Dr. Pierre Hellier: *For their care and support in France.*
- Dr. Pierrick Coupé, Dr. Vladimir Fonov, and Dr. Hassan Rivaz: *For all manners of insightful and pedagogical discussions.*
- Former and present members the Image Processing Laboratory, the Brain Imaging Centre, and the Montreal Neurological Institute; Dr. Berengere Aubert-Broche, Lara Bailey, Jennifer Chew, Simon Drouin, Dr. Simon Eskildsen, Dr. Daniel Garcia-Lorenzo, Anka Kochanowska, Kelvin Mok, Ellie Tobman, Yiming Xiao, Dr. Charles X. B. Yan, and Dr. Rina Zelman: *For their invaluable help, be it directly or indirectly related to this work.*
- Nicolas Guizard and Marta Kersten: *For their help in editing the manuscript, among many other things.*
- 陳澤霖，陳吳立娟，陳范玉容，陳熾昂: *For all their patience and unending support in my endeavours.*

ABSTRACT

The effectiveness of image guided neurosurgery (IGNS) depends on the presentation of accurate image data to a neurosurgeon for surgical planning and guidance. The blood vessels supplying the brain are of particular importance in IGNS, because they densely surround brain lesions and tumours, may themselves be the sites of pathologies, and need to be carefully considered during surgery.

Given the importance of visualizing and identifying vasculature for diagnosis, planning, and guidance, there is a strong need for automated vessel enhancement and registration techniques. Furthermore, tools for the characterization and validation of developed image processing methods are needed. This thesis presents the development of three separate techniques to address the above stated needs: (1) a vessel-based intraoperative image registration technique, (2) a technique for producing anatomically realistic multimodality imaging phantoms, and (3) a non-local estimator based vessel structure enhancement technique.

For intraoperative registration, where preoperative images are aligned to the patient on the operating room table, we developed a hybrid non-linear vessel-based registration algorithm. Our technique combines the benefits of feature-based and intensity-based vessel registration methods. Raw volumetric images are processed through feature enhancement to produce a set of image intensity maps for registration using cross-correlation. By not explicitly extracting discrete vessel features, we can be assured that removal of important registration information is minimized. We extensively validated our registration method for robustness and accuracy using a

large number of synthetic images, real physical phantom images, and real clinical patient images.

In validating our registration technique we realized a need for improved physical phantoms. As such, we developed a multimodal anthropomorphic brain phantom for inter-modality image processing validation. The brain phantom (1) has the mechanical properties and anatomical structures found in live human brain and (2) was made from polyvinyl alcohol cryogel. Marker spheres and inflatable catheters were also implanted to enable good registration comparisons and to simulate tissue deformation, respectively. Multiple sets of multimodal data were then acquired from this phantom and made freely available to the image processing community.

Based on our vessel registration work, we also found a need for improved vessel enhancement methods. Therefore, we developed a technique that extends Frangi's vessel enhancement method to improve background suppression. To do this, we account for larger vessel geometries over an extended area rather than solely using information from a small local region. Validation of the technique was performed on 3D synthetic images, and 2D and 3D clinical images. The results revealed that by analyzing larger image regions to improve background suppression and identify vessel-like structures, our method can effectively enhance and improve retention of thin and lower contrast vessels in comparison to Frangi's method.

The automated vessel enhancement and vessel-based image registration techniques developed in this thesis can be used to improve the effectiveness of surgical work-flows in IGNS. Our anthropomorphic phantom can be used to validate and characterize novel image processing methods.

ABRÉGÉ

L'efficacitée de la neurochirurgie guidée par l'image (IGNS) dépend de la présentation au neurochirurgien d'images précises pour la planification chirurgicale et l'orientation. Les vaisseaux sanguins cérébraux sont d'une importance particulière en IGNS, parce qu'ils entourent densément les lésions cérébrales et les tumeurs, et peuvent eux-mêmes être le siège de pathologies, et doivent être soigneusement examinés durant la chirurgie.

Compte tenu de l'importance de la visualisation et de l'identification des vaisseaux cérébraux pour la planification du diagnostique et de l'orientation, il est important de développer des techniques automatisées pour augmenter les contrastes des vaisseaux, ainsi que des méthodes de recalage des images préopératoires. De plus, des outils pour la caractérisation et la validation des méthodes de recalage et de segmentation sont nécessaires. Cette thèse présente le développement de trois techniques différentes pour prendre en comptes ces besoins: (1) une technique qui utilise les informations des vaisseaux sanguins pour le recalage des images préopératoires, (2) une technique pour produire des fantômes multimodaux avec des structures anatomiquement réalistes, et (3) une technique pour augmentater les contrastes des vaisseaux sanguins avec un estimateur non-local.

Pour le recalage d'images préopératoires, où les images sont alignées par rapport au patient sur la table de la salle d'opération, nous avons développé une approche hybride de recalage avec transformation non-linéaire. Notre technique combine les avantages des techniques de recalage basées sur l'intensité et les attributs

géométriques. La segmentation des vaisseaux sanguins est appliquée aux images volumétriques natives pour produire un ensemble de cartes d'intensité afin d'utiliser la corrélation croisée pour le recalage. En maintenant les structures sanguines comme cartes d'intensité, au lieu de l'extraction comme les caractéristiques discrètes, nous pouvons être sûr que d'importantes informations de l'image ne sont pas supprimées pour le recalage. Nous avons validé en détail la robustesse et la précision de notre recalage par vaisseaux sanguins en utilisant un grand nombre d'images de synthèse, de véritables images de fantômes physiques et de vraies images cliniques de patients.

En validant notre technique de recalage d'image, nous avons réalisé le besoin d'améliorer les fantômes multimodaux. Pour cela, nous avons développé un fantôme anthropomorphique du cerveau qui peut être efficacement utilisé pour la validation intermodalité du traitement des images. Le fantôme cérébral, qui a les proprietés mécaniques et une anatomie similaire; au cerveau humain *in vivo*, a été fait à partir d'alcool de polyvinyle cryogel. Des marqueurs sphériques et des cathéters gonflables ont également été implantés pour permettre de simuler la déformation des tissus et de comparer la qualité des recalages. Plusieurs ensembles de données multimodaux ont été acquis avec ce fantôme et ont été mis à la disposition de la communauté qui travaille sur le traitement des images.

Notre travail sur le recalage des vaisseaux sanguins nous a également révélé la nécessité d'améliorer les méthodes numérique des vaisseaux. En conséquence, nous avons développé une technique qui pousse la méthode de Frangi en augmentant le contraste et en supprimant les éléments de fond. Ainsi, pour détecter des géométries des vaisseaux sanguins plus grandes, nous considérons une zone de recherche plus

grande plutôt qu'une petite zone locale. La validation de la technique a été réalisée avec des images synthétiques 3D, et des images cliniques 2D et 3D. Les résultats ont révélé que notre approche pour augmenter le contraste en supprimant les éléments de fond pour identifier des structures comme les vaisseaux sanguins, améliore la rétention des vaisseaux sanguins fins avec des contrastes faibles par rapport à la méthode classique de Frangi.

Les techniques automatisées pour le recalage et l'augmentation des contrastes des vaisseaux sanguins développés dans cette thèse peuvent être utilisées pour améliorer l'efficacité des processus chirurgicaux en IGNS. Notre fantôme anthropomorphique peut être quant à lui utilisé pour valider et caractériser de nouvelles méthodes de traitement d'image.

TABLE OF CONTENTS

LIST OF TABLES

LIST OF FIGURES

Figure page

CHAPTER 1
Introduction

1.1 Motivation for Vascular Image Processing for Image Guided Neurosurgery

Computer assisted planning and image guidance is a critical and integral part of modern neurosurgery. Image guided neurosurgery (IGNS) involves acquiring the preoperative images of a patient's brain and evaluating the images to build a surgical plan. These images are then used by a neurosurgeon for navigation during a procedure to properly implement the treatment determined by the surgical plan [30, 202, 201, 264].

IGNS effectively augments a neurosurgical procedure by aligning pre-operative patient images with the surgical field, properly visualizing the patient's image data, and allowing fuller interaction with the images using tracked surgical instruments. These functionalities provide a neurosurgeon with important information regarding the locations and orientations of their surgical instruments in relation to the patient's anatomical structures. By using IGNS, a neurosurgeon may more confidently target pathologies while avoiding and sparing healthy tissues during a surgical procedure. IGNS can improve the precision and accuracy of the procedure, thus helping the surgeon effectively deliver treatment. This in turn can improve a patient's surgical outcome and shorten the time needed for their postoperative recovery. [30, 32, 178, 201, 264].

Along with the brain and nerve tissues, the cerebrovasculature is also of particular importance in neurosurgery. Cerebrovasculature consists of the dense network of vessels that provide tissues of the brain with a steady supply of blood to ensure their continued function. These blood vessels, both arteries and veins, must be handled with great care due to their fragility and their important physiological role of irrigating and draining brain tissue. Any unintentional disruption of healthy vasculature can result in complications to blood supply in different regions of the brain. In the worst case, such a disruption can result in the death of brain tissue.

At the same time, blood vessels may themselves be the site of abnormalities or lesions that require precise targeting for treatment. Great care must be taken with abnormal vessels as they often have weakened walls or are unstable and may rupture during surgical treatment. In general, due to its low tolerance for error, inaccuracies in neurovascular and neurosurgery could result in brain damage and neurological deficits. Such damage may worsen a patient's surgical outcome and impair also impair their physical, intellectual, and psychological function.

On the other hand, cerebral neurovasculature can also aid in neurosurgical guidance. Vascular networks and vessels may provide key distinct visual landmarks that can be used by neurosurgeons for localization and orientation within the surgical field of view. By identifying vessels directly during a neurosurgical procedure, a surgeon can mentally visualize the location of their resection and make adjustments to the path of the procedure should the need arise. Neurovascular anatomy is also taken

into consideration when determining an optimal resection corridor to deep brain lesion. Therefore, proper imaging, localization, and identification of vessels in patient medical images are of great importance in IGNS.

Various imaging modalities exist that capture neurovascular data in the form of angiographic images. However, the images themselves are often not usable in their raw and unprocessed forms for IGNS. For instance, neurovasculature from certain magnetic resonance (MR) angiographic images may not have enough contrast against the parenchymal tissue to be used directly for vessel visualization. These angiographic images require at least some degree of image processing and/or manual labelling before they can be used for surgical navigation. Preoperative and intraoperative images of various medical imaging modalities may also not be aligned, or registered, well enough for guidance. Effective vessel registration in turn relies on having well segmented or enhanced vessel datasets to correctly align medical images for surgical planning and guidance. Therefore, improving the efficacy of angiographic image enhancement and image registration methods could potentially also help improve the efficiency and accuracy of IGNS.

In this thesis, we developed, tested, and validated a set of tools to process neurovascular data for use in IGNS. First, we developed an intraoperative vessel registration method to update the position of the preoperative images and account for any changes in brain shape. Based on these experiences, we proceeded to prototype an imaging phantom to validate registration and segmentation algorithms. Finally, we developed a vessel enhancement algorithm to enhance vessel structures in preoperative angiographic medical images from their parenchymal tissue backgrounds.

1.2 Outline of Thesis

This thesis is organized as follows:

In Chapter 2, we provide a literature review on the integration of angiographic images into IGNS, the construction of physical vessel phantoms for validation, vessel-based registration, vessel feature enhancement, and related background materials relevant to this work.

In Chapter 3, we describe an image registration technique that uses segmented or enhanced vessel images for intraoperative registration of Gadolinium-enhanced T1-weighted MR images and Doppler ultrasound images. Vessel structures are highly salient in the aforementioned imaging modalities, and due to their anatomy and physical characteristics, they make for reliable features for intraoperative brain image registration. The method is a hybrid of feature and intensity-based registration that uses minimal processing to extract the vessel structures and then recovers any distortion present between the images by using non-linear registration.

In Chapter 4, we present a physical multimodal, anthropomorphic phantom that can be used to validate medical image processing methods developed for imaging using MR, computed tomography (CT), and ultrasound imaging modalities. The phantom is built from polyvinyl alcohol cryogel, a stable, rupture resistant material that can be formulated to simulate soft-tissue deformations. Due to its multimodal imaging characteristics the phantom can be used to validate multimodal registration and segmentation methods.

In Chapter 5, we present a method developed for enhancing vascular structures from 2D retinal angiographic data and 3D phase-contrast MR angiographic images

such that the resulting vessel maps can then be use for radiological diagnosis or guidance and planning in IGNS. The method uses a combination of Hessian eigenvalue analysis and non-local means weightmap PCA eigenvalue analysis to enhance vessel-like structures in angiographic images.

We conclude in Chapter 6 with a discussions of possible avenues for future work in neurovascular image processing.

1.3 Author Contributions

I am the first author of all three manuscripts included in this thesis and have performed all of the methodological developments, software implementation, experimental design, data processing, and results analysis for all experiments. The contributions of all co-authors include supervision, data acquisition, experimental setup, technical discussions, and the review of manuscripts. The following list summarizes the contributions of each author by manuscript:

Chapter 3 - Validation of a Hybrid Doppler Ultrasound Vessel-based Registration Algorithm for Neurosurgery

- Authors: Sean Jy-Shyang Chen, Ingerid Reinertsen, Pierrick Coupé, Charles X. B. Yan, Laurence Mercier, D. Rolando Del Maestro, D. Louis Collins
- Contributions: Guarantors of the study: all authors; Study concepts and design: S.J.S.C., I.R., P.C., C.X.B.Y., D.L.C.; Algorithm and implementation: S.J.S.C; Data Acquisition: S.J.S.C, I.R., L.M.; Experiments and analysis: S.J.S.C.; Guidance and supervision: D.L.C.; Manuscript preparation: S.J.S.C; Manuscript revision: all authors; Editing and final approval: S.J.S.C, D.L.C.;

Chapter 4 - An Anthropomorphic Polyvinyl Alcohol Brain Phantom Based on Colin27 for Use in Multimodal Imaging

- Authors: Sean Jy-Shyang Chen, Pierre Hellier, Maud Marchal, Jean-Yves Gauvrit, Romain Carpentier, D. Louis Collins
- Contributions: Guarantors of the study: all authors; Study concepts and design: S.J.S.C., D.L.C.; Data Acquisition: S.J.S.C, P.H., M.M., J.Y.G; Data preparation and processing: S.J.S.C, R.C.; Experiments and analysis: S.J.S.C. ; Guidance and supervision: D.L.C.; Manuscript preparation: S.J.S.C; Manuscript revision: all authors; Editing and final approval: S.J.S.C, D.L.C.;

Chapter 5 - Blood Vessel Enhancement Through Principle Component Analysis of Non-local Means Weightmaps

- Authors: Sean Jy-Shyang Chen, Pierrick Coupé, D. Louis Collins
- Contributions: Guarantors of the study: all authors; Study concepts and design: S.J.S.C., P.C.; Algorithm and implementation: S.J.S.C; Experiments and analysis: S.J.S.C.; Guidance and supervision: D.L.C.; Manuscript preparation: S.J.S.C; Manuscript revision: all authors; Editing and final approval: S.J.S.C, D.L.C.;

1.4 Original Contributions

The following are the main original contributions of this work:

1. Developed and implemented a novel image registration technique that uses hybrid feature-based and intensity-based intermodality registration methods to align MRA to Doppler ultrasound intermodality registration;

2. Designed and implemented a digital phantom that simulates US vessel volumes from extracted MR vessel structures to validate intermodality registration;
3. Extensively validated the new registration method using the digital phantom, a physical phantom, and real clinical data;
4. Developed and fabricated a physical deformable multimodal anthropomorphic phantom that can be used for validation of medical image processing methods;
5. Developed phantom material formulas for realistic rheological properties to simulate brain shift and are easily imagable in MR, computed tomography (CT), and ultrasound imaging modalities;
6. Acquired images of the phantom in ultrasound, CT, and numerous MR imaging modalities and made them available to researchers and the general public.
7. Developed and implemented a novel 2D and 3D vessel enhancement method using the non-local means (NLM) method to modify the background suppression term in Frangi's vesselness method [81];
8. Developed a method for eigenvalue analysis of the NLM weightmap to detect large regional vessel features;
9. Extensively validated the new segmentation method using synthetic data as well as real clinical 2D retinal angiographic images and 3D phase-contrast MR images;

CHAPTER 2
Background

2.1 Vessels in Image Guided Neurosurgery

Modern neurosurgery is a specialized area in surgery concerned with the treatment of the affected portions of the human nervous system, which may include the brain, spinal cord, the cranial nerves, and the peripheral nerves. Modern neurosurgery relies heavily on computer assistance to provide information to surgeons regarding the location of their instruments. This allows for more accurate and precise procedures, thus reducing morbidity and improving patient outcome. Known as image guided neurosurgery, these computer assisted techniques typically use the preoperative images of the patient's brain for (1) surgical planning and (2) surgical navigation to help in the execution of the procedure [30, 201, 264].

Neurosurgical planning often involves the identification and examination of key cerebral vasculature by the neurosurgeon in the preoperative images. This allows a surgeon to see the vessels that will be in their resection corridor, which not only helps in mentally visualizing the location and orientation of a patient's anatomy, but also allows the surgeon to avoid damaging key vessels during a procedure. Due to the benefits of the additional information provided by angiographic images, there has been increasing interest in further integrating them and other types of vessel data into IGNS for a variety of neurosurgical procedures. For example, using angiographic images in IGNS for tumour surgery can help a surgeon avoid vessels that

surround the lesion while identifying and ligating those that irrigate it. The vessel information can also be used for planning trajectories in deep brain stimulation to allow electrodes to be inserted in such a manner that critical blood vessels are not disturbed or damaged [30]. Angiographic images are also increasingly integrated into IGNS for intervention in the case of neurovascular pathologies such as in aneurysms and arteriovenous malformations (AVM). For instance, angiographic images provide general information regarding the position and orientation of the cerebral vasculature, which can help surgeon in planning for aneurysms and AVM of complex forms.

Integrating angiographic information into IGNS is particularly beneficial for locating aneurysms on smaller distal branches of cerebral arteries [117]. These lesions are typically more difficult to surgically locate due to the lack of large vascular structures combined with the high anatomical variance of these vessels in patient populations. Angiographic data enabled IGNS systems are also used to help surgeons precisely locate the necks of aneurysms and isolate vessels that may be adjacent to or surround the dome of the aneurysm. Such images were also found to be crucial when the aneurysm was embedded in a hematoma since it allowed the surgeon to remove the surrounding lesion and affected tissues without disturbing the unstable dome of the aneurysm[117, 40].

Use of angiographic images in IGNS can also aid surgeons in AVM resection by understanding the complex topology of the feeding and draining vasculature connected to the nidus. Proper integration of vascular information in IGNS helps a neurosurgeon determine which vessels to clip first and which regions to dissect for the best surgical outcome [157]. IGNS integrated with angiographic data can even

help locate and identify residual pathologies after an initial round of lesion resection, which enables removal of a residual pathologies without the need for subsequent surgery [157, 249].

Different modalities of 3D angiographic images have been used for IGNS. They include x-ray imaging modalities such as computed tomographic angiography (CTA) and rotational x-ray angiography (XA). Other common angiographic imaging modalities include magnetic resonance angiography (MRA) and ultrasound angiography using Doppler ultrasound. These techniques image neurovasculature with relatively high contrast and have been directly used for surgical guidance with limited preprocessing. However, the preoperative images can also be manually labelled by a technician for use as "vessel images", assuming that the vessels in the image are of sufficient saliency and labour is available for this intensive and tedious process. In the following subsections, we review clinical studies that examine the use of angiographic images in IGNS and the benefits that this addition information brings to the surgical procedure.

2.1.1 X-ray Modalities

Computed Tomography Angiography

Computed tomography angiography (CTA) is acquired using modern 3D helical computed tomographic imaging devices. A patient is scanned with intravenous contrast injection which effectively highlights the patient's neurovasculature that are larger than the acquired images' resolution. Modern CT scanners can achieve isotropic voxel resolutions of 0.3mm. The patient can be scanned with skin-based fiducials which can then be used to aid registration with a preoperative anatomical

image. As well, landmarks on the patient's skin can be acquired directly using a tracked pointer to identify their corresponding chosen points on the preoperatively scanned image. CTA is sometimes used in conjunction with MR images since the latter provide more detailed anatomical information for soft tissues. Registration can also be performed directly between the anatomical MR and the CTA image if sufficient corresponding anatomical landmarks such as sulcal and skin features, are visible on both angiographic and anatomical images. The neurovasculature in the CTA image can also be used as features for registration without the use of fiducials.

Due to the quality of the vascular images acquired using CTA, numerous groups have used this type of angiographic images for surgical planning and navigation in IGNS. For instance, Coenen *et al.* [46] reported their early results using 3D CTA images for IGNS on four patients with small AVMs in large hematomas. Their initial experience with this technique revealed that when the CTA was viewed with the 2D angiograms, feeding and draining vasculature to the AVM can be distinguished despite the presence of large blood clots. This allows the surgeon to accurately localize and isolate the AVM nidus from surrounding lesions and tissue, thereby decreasing surgical morbidity. Kim *et al.* [117] registered the CTA image directly to the patient using commercial neuronavigation systems to help to locate and clip aneurysms on the distal branches of the anterior cerebral artery in 12 patients. The use of IGNS with angiographic data can also ease the localization of difficult-to-find aneurysms in a hematoma cavity, thus helping to prevent premature rupture during surgery. They concluded that the use of angiographic data for IGNS enabled their neurosurgeons to identify the aneurysms and facilitated their exposure for clipping.

Their use of CTA in surgical guidance also allowed for smaller craniotomies and precise navigation enabling the surgeons to reduce the invasiveness of the surgery.

IGNS has also been performed with CTA images which have been registered and visually merged with other image modalities, such as anatomical MR images. Chibbaro and Tacconi [40] reported their surgical findings in merging CTA data with a preoperative MR guidance image for IGNS. From their experience, the use of angiographic data with MR in guidance was key in allowing their surgeons to gain a better understanding of the aneurysm or AVM's position in the patient in the context of other critical anatomical structures in the brain. This improved understanding allowed for reductions in the size of craniotomy and helped avoid surgical issues such as premature AVM bleeding or ischemic complications.

Rohde *et al.* [210] merged CTA images with brain images from other imaging modalities and segmented brain structures for an even more comprehensive data visualization for IGNS. For their cases, they merged anatomical gadolinium-enhanced T1 weighted MR images, diffusion weighted MR images, CTA images, and manually segmented structures of surgical importance, which included blood vessels, nerves, and various forms of brain tumours. Through sixteen patients in which their methods were employed, they found that the methods facilitated the surgical approach in four of the cases and allowed them to devise a tailored approach for patients in two of the cases. The neurosurgeons indicated that the IGNS with vessel visualizations also allowed them to identify crucial but hidden neurovasculature in eleven of the sixteen cases.

Rotational X-ray Angiography

Rotational digital-subtraction X-ray angiography (XA), also known as conventional catheter angiography (CCA), can also be used for IGNS. Modern 3D XA can produce high quality vascular images due to their small isotropic voxel sizes, less than 0.3mm in width. Thin vessels are more easily visualized in XA compared to CTA since the contrast agent is injected directly into the arterial branch of interest instead of intravenously, respectively. The XA imaging modality, therefore allows the fine vascular branching around an aneurysm or AVM to be clearly visualize and evaluated intraoperatively. The highly selective nature of 3D XA also highlights only vessel branches where contrast is injected, thus enabling visualization of an anatomical region of interest without possibly confounding a surgeon with the sheer quantity of information from a complete cerebrovascular network. However, the XA images do not sufficiently visualize other brain structures nor patient skin surface features that are usually used for registration in surgical guidance.

Raabe *et al.* [198] uses a three-point stereotactic head frame to register their acquired 3D XA images to the patient for IGNS in 16 aneurysm cases. They found that although the XA images did not show other vessel branches to allow surgeons to fully orient themselves in relation to the patient, there was generally sufficient correspondence of the vascular structures in the XA image to the patient's vessels. The use of XA was also useful in helping predict the location of the aneurysm during surgery, especially when the aneurysm and the branching vessels were occluded by brain paranchyma or covered by blood clots. This helped minimize the exposure of patient and the additional information improved the quality of aneurysm surgery.

An alternate way of registering XA to the patient using fiducial markers was used by Willems *et al.* [258]. In their work, the authors acquired XA images for IGNS and measured the position of physical registration fiducials on the patient using a tracked pointer. This process registered the XA image to the patient's head for visualization in the view orientation of a surgical microscope. The method was tested on a physical phantom and two clinical cases, which showed that surgical display of XA for IGNS is feasible and helped in the surgeon's understanding of the surgical scene. With further development, 3D XA can be used in IGNS to aid neurosurgeons in their intraoperative spatial understanding of vascular pathologies.

2.1.2 MR Modalities

MR angiography can also be used in IGNS. The methods for its acquisition are much less invasive than conventional catheter contrast imaging. As well, unlike CTA and other X-ray based imaging modalities, MR does not expose a patient to ionizing radiation. This allows more images to be acquired at reasonably frequent intervals for surgical planning and guidance [123]. MRA can also match conventional CTA and XA vessel images in showing the location and flow of vascular lesions. However it has been noted that MRA vessel contrasts are less than XA or CTA and it does not always allow for the same level of time and spatial resolution. This may result in the underestimation of the sizes of vessel pathologies for procedure planning and possibly overlook small early-draining veins or simple arteriovenous shunts [254, 125]. As well, MRA imaging is less selective in vessel contrast enhancement than XA, which may make surgical visualization more challenging to interpret.

Warren *et al.* [254] reported their experience comparing time-of-flight MRA and contrast enhanced MRA with XA for guidance on 40 patients. They reported that MRA provided similar information to XA for AVM surgery in terms of lesion size and blood flow but the size determination for XA was more accurate for larger vessel lesions. MRA also did not detect as many small and slow blood flow vessels compared with XA. However, MRA enabled formatting of different guidance views that were not available with their conventional XA imaging methods. The authors indicated that less-invasive MRA should be more thoroughly investigated for use in surgical planning and IGNS.

Konig *et al.* [125] described their results of using surface rendered 3D time-of-flight MRA images with T1, T2, and diffusion weighted MR images for guidance in aneurysm surgery on four patients. The authors noted that the MRA aneurysm images were of sufficient quality for guidance in three out of the four patients, while the forth did not properly highlight the lesion due to slow blood flow. They also found that the use of MRA images with information from other MR imaging modalities was useful in indicating the size and configuration of aneurysms. However, they also noted that surgical planning using MRA could be significantly improved with better vessel segmentation.

MRA has also been applied for endovascular INGS treatment of aneurysms by Kocer *et al.* [123]. They proposed the real-time merging of 2D fluoroscopic interventional images to preoperative 3D MRA images to gain an understanding of the anatomical relationships of a lesion. They found that using MRA in IGNS helped reduce the patient exposure to ionizing radiation. As well, they found that

the addition of MRA information allowed them to reduce the amount of radiographic contrast agents needed for intraoperative fluoroscopic imaging on patients with renal insufficiency. As well, the merging of the two modalities for guidance helps overcome the lower spatial resolution of MRA.

2.1.3 Ultrasound Modalities

The use of ultrasound Doppler imaging in IGNS allows intraoperative acquisition of vessel data. The benefits of the modality are that it acquires high resolution 3D vessel images with the direction and magnitude of blood flow. The images are acquired after craniotomy using a tracked 2D or 3D ultrasound probe either on the dura, or on the cortical surface of the brain, or in fluid inside a resection cavity. In the case of 2D ultrasound images, each tracked image plane is reformatted into a 3D image slab that can then be used for surgical planning, guidance, or visualization. The ultrasound angiographic data provides the surgeon with additional information during a neurosurgical procedure for localization and helped improve treatment of vessel lesions.[249, 157]

Using information from 3D MRA and Doppler ultrasound angiography, Unsgaard *et al.* [249] evaluated the benefits of combining ultrasound vascular imaging with IGNS for AVM surgery in nine patients. The feeding arteries were visualized using stereoscopic displays which enabled the surgeons to locate and clip most of the vessels early in the procedures. The use of intraoperative ultrasound angiography proved to be highly beneficial in one instance when a residual nidus was identified in the ultrasound image and was able to be removed immediately. They concluded

that using angiographic images in IGNS with stereoscopic displays can help a surgeon quickly and successfully plan, locate, and facilitate the clipping of AVM feeders in the initial phases of surgical intervention.

Mathiesen *et al.* [157] also combined 3D ultrasound angiography in IGNS for the treatment of nine patients with AVMs. The author used stereoscopic displays along with volume rendering to help the surgeons plan their approach and locate the feeding and draining vessels for the AVM nidus. The surgeons believed that the AVM resection was aided by ultrasound; the preoperative MRA provided the configuration and topology of the greater vasculature, while the intraoperative ultrasound angiography helped determine blood flow rates in the vessels. The ultrasound angiographic images not only corresponded to the intraoperative findings by the surgeon but similar to [249] also helped in the identification of a residual nidus, allowing for its immediate removal. The authors concluded that use of the ultrasound angiographic imaging allowed the surgeons to have a better understanding of the form and configuration of AVMs leading to the success of all nine patients undergoing their treatments.

2.1.4 Challenges

The direct use of angiographic images in IGNS can provide benefits to the surgeon in terms of localizing vessel lesions and understanding their topology and spatial relationship with other surrounding vessels and paranchymal tissues. This improved understanding can help reduce the procedure's invasiveness, limit patient exposure to ionizing radiation or contrast agents, and lessen patient complications in neurovascular surgery.

However, the angiographic and anatomical guidance images may not always accurately represent the state of the patient due to errors in navigation tracking and fiducial registration. The preoperatively acquired guidance images may also not accurately represent the actual state and positions of the patients vessels and brain during the procedure due to brain shift and other soft-tissue deformations. Finally, although the angiographic images can effectively show a patient's larger vessel structures, finer vessels with widths less than the voxel size may not be sufficiently well enhanced for use in IGNS.

These challenges necessitate the development of novel algorithms to help enhance smaller or lower contrast vessel structures, and better image registration methods, such that angiographic data can be effectively used in surgical guidance.

2.2 Vessel-based Image Registration

Image registration involves bringing an individual patient or a group's medical image data into the same coordinate frame. The images are properly registered when their corresponding anatomies are spatially aligned. It is through proper registration that medical images can then be used for radiological diagnosis, quantitative disease progression monitoring, post-surgical follow-up, and also surgical planning or guidance for IGNS. Medical image registration, as such, is an important and an active area of research in the field of medical image processing and intervention.

Image registration methods can be roughly classified as belonging to one of three different strategies, namely: feature-based, intensity-based, and hybrid techniques. Feature-based registration methods explicitly extract specific features from a set of

medical images through pattern recognition methods, and then matches these homologous features to recover the geometric transforms that align them. The benefit of feature-based methods is that they separate relevant structures in the image from the background thus reducing the number of local minima and the chances that the registration process would be stuck in one. The identification of key anatomical features, such as tissue folds, vessel bifurcations, or point-like structures, also allows highly specific alignments which improves accuracy. Finally, feature extraction reduces the large amount of information contained in image data to a smaller set of parametrized feature information. This greatly reduces the amount of computation needed for registration and can thus increase the speed at which the method converges to a solution. By deceasing the complexity in the image scene and reducing the possible local minima, feature-based registration methods can be used for intraoperative or realtime registration, where fast and accurate results are essential.

Intensity-based registration methods rely on finding image intensity correspondences that are intrinsically present in image and use similarity measures such as cross-correlation and mutual information to drive registration optimization. Assumptions regarding any features present or encoded in the image's intensities are implicit, with no intensity-based structures explicitly defined and parametrized. For this reason, intensity-based method are robust to feature detection errors and the creation of artifacts that may arise due to feature-based preprocessing. This also allows it use intrinsic image features that otherwise may be removed or "overlooked" by the preprocessing, thus possibly improving registration success.

Hybrid registrations methods combine aspects of both intensity and feature-based registration strategies; anatomical features are extracted to a limited extent on either one or both target and source images. This class of methods seeks to negotiate aspects of both (1) computation speed-ups and (2) feature quality. For example, by performing registration on extracted features the computational load can be greatly reduced. However the process of feature extraction also requires additional computation and this overhead can be high. Sub-optimal feature extraction can introduce artifacts or remove key information that can cause registration to fail. As such, hybrid registration often seeks to complete the necessary feature extraction when results are not urgent (e.g preoperative processing) to reduce computation overhead when registration results are needed promptly. The extent of feature extraction might also be adjusted to balance the robustness of extracted info with the speed of feature extraction.

Vessel-based image registration uses commonly found vascular anatomical features in medical images to spatially align medical images. Vascular structures are good candidates for registration since they are well distributed throughout the human anatomy and easily imagable with imaging devices of various modalities thus ensuring that they will be present in most regions of interest. As well, the branched structures of vascular networks are topologically unique to a subject, which enables less ambiguous image alignments than registration methods reliant on tissue borders or more topologically simple structures.

As with other registration methods, vessel-based registration can be intensity-based, where high contrast angiographic medical images allow vessels to be directly

registered based on their intensity information. More commonly, vessel registration methods are either feature-based or a hybrid, where a vessel lumen is first extracted from the raw image through thresholding or via vessel segmentation, and then modelled as a set of parameters including vessel center-points, diameters, or bifurcation points. In feature-based vessel registration, the corresponding extracted features are matched directly and registered. In hybrid vessel registration methods, the extracted features can be used directly to register with a raw intensity images, or the extracted features can be reconstructed back to an intensity image to register with a raw intensity image. In some cases, a limited amount of vessel feature extraction is applied to both images to produce simplified vessel intensity maps, which are then registered.

2.2.1 Feature-based registration

Alperin *et al.* [6] described one of the first techniques for registration of 2D XA images to 3D MRA images. The angiographic images from the two modalities were registered by choosing which vessel segments to use for registration, finding the vessel centerpoints in the XA, manually identifying MRA vessel points, and then interatively finding the transform that matched the two point sets. The registration results were validated on a physical phantom and on 2 sets of clinical data using image fiducials. They found that sub-millimetre error registration can be attained on the patient data and that the registered and merged images can help a radiologist attain better understanding of patient anatomy.

Liu *et al.* [142] also proposed a 2D XA image to 3D MRA registration method. The algorithm is based on projective invariance, where the projection of 3D tubular

object's skeleton matched to that of the 2D line skeleton. The method first preprocesses the skeletons of both 2D and 3D images then quantifies the 2D projection disparity as a numerical model before optimizing the cost with Newton's method to recover the rigid registration transform. The method achieved submillimetre registration errors with good capture radii and performed better when more vessel segments were available for calculating the transformation. The registration method was found to compare well with images that were manually registered by an expert, in terms of accuracy and time. Bullitt *et al.* [28] performed further clinical tests using the registration method of Liu et al. [142] to compare registration time and quantitative and qualitative registration accuracy in patient cerebral angiographic images. In their tests, they found that there was no statistically significant difference between registration results achieved by experts and those by the method. However the method was shown to be significantly faster than manual registration methods even though the method requires initial manual alignment for images with further initial starting positions.

Nakajima *et al.* [172] describe a method for registration of cortical surface vessel models segmented from preoperative PC MRA images to vessel images taken from video images of the surgical field. The MR images were preprocessed to reduce noise, correct for spatial non-uniformity, the vessel structures were thresholded, filtered for connectivity, and extracted using the marching cubes algorithm. The 3D vessel models were then registered manually to the captured video images. In comparisons of the vessel to vessel registration with skin to skin landmark registration

on seventeen patients and a physical phantom, the authors found that the use of vessels significantly reduced the registration errors measured on artificial landmarks.

Kita *et al.* [122] proposed a real time 2D to 3D vessel registration algorithms based on matching the projected image vessel centerpoints using the iterative closest point method. Both the 2D and 3D images are surface modelled and skeletonized for centerpoints. The local region of each point on the 2D image was then searched to find their corresponding point on the 3D image, and the rigid transform was than calculated. The method was tested using nine cerebral 2D XA images on two 3D MRA surface models and found to successfully align the images except in the cases where the initial centerpoints extracted by skeletonization was poor. The method was able to correctly compute the rigid transforms in under 6 seconds.

Slomka *et al.* [228] described their rigid registration algorithm to align 3D B-mode and power Doppler ultrasound images to 3D MRA images of the carotid bifurcation of six patients. The images were first thresholded to eliminate non-vascular background and noise and then rigidly registered using the simplex algorithm with mutual information. The method was tested on data from 5 patients and was able to register their images with millimetre translation errors and rotational errors of around 2 degrees from initial errors up to 10 mm and 40 degrees, respectively. The author found that the method was also robust to errors when vessel segments more than 8 mm long were available for registration. However, the method was also reliant on the aortic bifurcation for registration success.

Porter *et al.* [193] also described an algorithm that rigidly registered reconstructed 3D colour Doppler ultrasound vessels images with 3D MRI vasculature.

The vessel volumes were first segmented by thresholding the image using the mean of the local intensity and then applying morphological operations to clean the image of isolated non-vessel voxels. The voxels from the processed MR and US images were then converted to point clouds and used for registration. Optimization was done by iteratively translating or rotating the point sets against one another, choosing the transformation that gives the highest correlation between the points of the two images and repeating the iteration. The algorithm was tested on segmented forearm vasculature, liver vasculature, and on a prostate phantom and errors were found to be 4–8mm, 2–4mm and 2mm, respectively.

Aylward *et al.* [13] have proposed a CT-to-CT rigid body registration algorithm that uses the vessel model generated by the vessel enhancement algorithm of Aylward and Bullitt [14]. The authors first created an accurate tubular vessel model from a source image applying their segmentation algorithm, and then registered this model directly with the target images acquired from the same patient. The method was tested on CT images of the liver and on pre and post-operative brain MRA images, and was capable of registering the vessel images with sub-voxel consistency, converging in approximately six seconds. Through their validation they found that their method was robust to ambiguous and poorly corresponding vessel segments and also to non-rigid deformations in the vessels themselves. This method was further applied by the authors [15] for registration of CT vessel images with intra-operative B-mode Doppler images acquired for guidance in liver tumour ablation. The center-points of the CT vessels, extracted through pre-operative processing, were registered to the bright vessel structures in the ultrasound image. The mean error for their

CT to ultrasound registration was 2.3 mm with a maximum of 2.8mm. The authors indicated that there errors were well within their margin of accuracy.

Jomier and Aylward [114] extended the rigid registration method of Aylward *et al.* [13] to correct for non-linear tissue deformations. The method first completes a round of rigid registration to place the vessels in their relative positions, then each branch in the vessel tree was rigidly registered in a piece-wise manner according to the extracted morphological information of the vessel tree. Finally all points along the vessel branches were non-linearly registered to each other, constrained by user selected elasticity and rigidity parameters. The authors tested their method on a vessel phantom and on pre and post-operative cerebral MRA images and found that it is highly robust to image noise and that 87% of vessel centerline points in their source vessel model were within two voxels of target image centerlines.

Lange *et al.* [131] described a method for registration of vasculature from CT or MR image to power Doppler ultrasound images. The method first segmented the vessels from pre-operative CT or MR images through region growing with manual processing and then skeletonized them to get a set of vessel centerlines. The 2D ultrasound images were reconstructed into 3D volumes and the vessels were processed in a similar fashion to the pre-operative images. The vessel centerlines were then aligned using the iterative closest point (ICP) algorithm and the match point pairs were used to compute the non-linear transform using multilevel B-splines. The authors validated their registration method on images from 3 patients put in 50 different starting positions and found that the resulting registration errors were almost always under one millimetre with only 4% failure in all the trials.

Turgeon *et al.* [248] presented a fully automatic technique to rigidly register a preoperatively generated 3D coronary artery vessel model with images that can be intraoperatively acquired using 2D fluoroscopic angiograms. Vessels from the 2D and 3D images are enhanced using the algorithms of [124] and [216], then thresholded and filtered for connectedness. Registration is performed with the downhill simplex optimization method using single entropy correlation coefficient as the similarity measure. The method can use either one or dual-plane image 2D angiograms for registration and takes into account mismatches in cardiac phase. The authors validate their algorithm using semi-synthetic 2D and 3D datasets that were created from 4D clinical images. They found that the background, timing offset, and typical errors in the vascular tree reconstruction of the dual-plane version of the method had a success rate of 94% with an average accuracy of 2.19 mm.

Tashiro *et al.* [243] proposed a 3D registration method for tracking the movement of lung anatomy in a sequence of 3D CT images by matching stable vessel topological features such as junctions and bifurcations. Lung CT vasculature was extracted by thresholding and skeletonized to provide the vessel center voxels. Bifurcations at a vessel center voxel were detected if it also had 3 vessel center voxels as neighbours in its local 26-neighbourhood. These voxels were then converted to points in 3D space, matched using a probabilistic relaxation method, and tracked across successive 3D CT images. By examining the displacement vectors of the point pairs lung displacement measures can be obtained. The authors tested this technique using a clinical CT image that had been artificially deformed and also on a displaced

rigid bifurcation phantom. From their tests, they estimated that displacement error is within 1 voxel, which realistically quantify 3D organ motion and made the technique suitable for application in radiation therapy.

Reinertsen *et al.* [200, 202] also proposed a non-linear registration algorithm for correction of registration of MR and Doppler ultrasound brain vascular images. The method extracted the vessel structures from preoperative Gadolinium enhanced MR angiographic images and the intraoperatively reconstructed Doppler ultrasound vessel images and skeletonized them to recover their respective vessel centerpoints. The two sets of centerpoints were then linearly registered using ICP modified with a least trimmed squared robust estimator to reduce the possibility of incorrect point pairings. When the linear registration has converged, matching vessel point pairs were used to drive a thin-plate spline transform to compute the non-linear transformation between the images. The method was then validated by using digitally simulated and physical brain phantom images [199]. The author also validated the technique on clinical datasets in [202, 201]. In their test, they found their registration method was able to accurately and robustly correct non-linear deformation between MR and ultrasound images with a high degree of accuracy.

Groher *et al.* [91] introduced a graph-based algorithm for rigidly registering abdominal 3D CT angiographic (CTA) to 2D digital subtraction angiographic (DSA) images. The method first preprocessed the 3D CT vessel features by first regularizing the intensities and 2D images by vesselness enhancement using [81]. Both 2D and 3D were extracted by region growing from a user selected seed point. The extracted features were then skeletonized and the resulting centerpoints organized into graph

structures by representing the detected bifurcations as nodes and their joining centerpoints as graph edges. Registration is done using the downhill simplex algorithm matching the graph generated from the DSA to the 2D projection of the graph generated from the 3D CT vessel image. The method was tested on a digital simulation, a physical head phantom, and the abdominal images of 4 patients. It successfully registered images in under 2 seconds. In over 200 simulated displacements, they showed that it robustly reduced registration errors.

Zikic *et al.* [272] introduced a graph-based registration method using *a priori* knowledge for realistic non-linear alignment of 3D CTA or MRA images to singular 2D DSA images. The method extracts vessel centerpoints and converts the vessel paths into graph models. The models are then rigidly registered to initially identify the corresponding points between the two graphs. The 3D graph is deformed to match its 2D projection to the graph of the 2D DSA, all the while with length preservation and smoothness constraints. The *a priori* knowledge from the constraints provided meaningful non-linear 3D deformations of 2D projections. Without the additional constraint, bending a 3D vessel and projecting the profile to a 2D image may result in an incorrect interpretation that the 3D vessel had been compressed and shortened. The method was tested on synthetic models and 2 liver angiographic images and showed improvements in position and shape error after registration. The method was further extended in Groher *et al.* [92] such that initially unknown point correspondence can be resolved while the registration undergoes optimization. Validation of the extended algorithm showed that it was able to converge to the right

solution from initial displacements up to 3.8cm. The registration also had submillimetre in-plane accuracy, though the accuracy was less in cases where the 3D vessel displacement was in the projection direction.

Ding *et al.* [65] proposed to track vessel features in microscope video images that were recording during tumour resection surgery. Starting and ending points of vessel segments in the images were first chosen and extracted using a minimum cost path algorithm. Points on the path were automatically chosen and the pixel intensities and other vessel features located perpendicular to the path at the points were recorded. These feature points were then matched to points in the following image frame by searching in the perpendicular direction to the curve. The matched point sets from the two image frames were then used to computed a thin-plate spline transform for image alignment. Validation was performed on 14 image sequences with only two failures. Processing of each image frame takes approximately one second. The method only requires manual input on the first frame, and is able to robustly track images even when the paths are obscured in certain image frames.

A 4D graph-based registration method was presented by Zhang *et al.* [271] for coronary artery motion tracking using CT angiograms. The authors' approach consists of first extracting vessel centerlines of the heart at end-diastole, extracting the start and end of the vessel and using a B-spline to model the vessel. The B-spline model was successively and non-rigidly registered to each cardiac image frame throughout the cardiac cycle using a free-form B-spline transformation model with normalized mutual information. Tracking of the vessels in all other phases of the cardiac cycle was done by using the motion fields acquired in the previous frame's

registration step and refining the accuracy of tracking using vessel templates. The authors then validated the method on eight cardiac CTA sequences. The test results showed that the proposed method was more robust than other non-rigid registration methods and that the models built from the registration tracking information were comparable to semi-manually created models.

A graph-based vessel registration method was also developed by Deng *et al.* [61], but in this case for the registration of retinal fundus images. The method operates by extracting vessel centerlines, detecting the bifurcation features, and forming a graph from the bifurcations by centerline connectedness. Graph matching was first performed to find general global correspondences between each image's bifurcation features. Incorrect matches were eliminated using a structure-based sample consensus method based on the RANSAC algorithm [78]. Finally the bifurcations were aligned using the previously found correspondences, ICP was used to finely register the images' vessel centerlines, and the registration transformation was computed. Tests on forty-eight clinical retinal image pairs demonstrated that optimum registration can be achieved using their method. The tests also showed that the method was invariant to linear images transformations and rapidly converged using only simple distance measures without additional feature descriptors.

Chen *et al.* [37] presented a retinal image registration method that detected and matched robust bifurcation features. Vessel centerpoints were extracted by ridge-based vessel extraction and their bifurcations were detected by filtering for vessel center pixels with three vessel center neighbours. Each robust bifurcation feature consists of the lengths of the 3 vessel segments that make up a bifurcation as well

as the angles of each of the vessel segments at the bifurcations and its adjoined neighbouring bifurcations. These extended features were robust to translation, rotation, scaling, and modest distortion. In their tests, the registration method was able to match corresponding vessel centerpoints with only a few isolated one-pixel registration offsets.

Huang *et al.* [105] described a technique to non-linearly register MR liver images deformed through different patient positions or respiratory phases. The method employed elastic solid mechanics to recover large motion deformations for soft tissues in high intensity focused ultrasound (HIFU) treatment. Liver tissue was segmented and vessel centerlines were extracted from MR images through skeletonization. The reference and target centerlines were used as matching features with a numerical liver organ mechanical model used to constrain the magnitude of deformation. When validated on clinical MR liver images, the vessel centerlines were well fitted with target registration errors below 2.3mm, with registration converging quickly and robustly. The authors noted that constraining tissue strain mechanics prevented the optimization from being trapped in a local minima, prevented over-fitting, and provided physically realistic non-linear registration results.

2.2.2 Intensity-based

Imamura *et al.* [106] proposed an image intensity-based intraoperative 2D fluoroscopic to 3D CT angiography registration method for assisting aortic stent grafting. The registration method generated 2D digitally reconstructed radiographs (DRR) by projecting 3D CTA to a 2D plane at multiple orientations and angulations, and found the one that most closely matched the fluoroscopic image to use its transform as for

registration between the two images. The authors' method extended upon the work of Penney *et al.*[182], to further allow for registration of images acquired both with and without contrast agents. This was done by detecting for contrast enhancement in the fluoroscopic images using vessel segmentation and then adding or subtracting the segmented vessel's intensity from the image to generate the appropriate DRR for image registration. The authors tested the method on 12 fluoroscopic images and found that cross-correlation worked well on low resolution data while M-estimator worked well on higher resolution data.

Hipwell *et al.* [99] adapted the the DRR method for registration of 3D PC-MRA images to 2D XA images. The author explored several strategies for producing a DRR from the MRA data with several similarity measures to match the produced MR-based DRR with the XA image. The search strategy for finding the rigid-body registration transform was done using gradient descent, adjusting the parameters for the DRR projection until a maximal value was found. The method required user input to specify a spherical volume of interest in the MRA data which was then mapped to a region of interest in the XA image. The method was tested on a physical phantom and on clinical images from three patients. The authors' results showed that using both vessel probability maps and explicitly segmented MRA images produced good DRR projections, and that using either gradient measures or pattern intensity measures produced good registration results.

2.2.3 Hybrid Registration

Penney *et al.* [181] proposed a technique to rigidly register liver MR with B-mode ultrasound images using vessel probability maps calculated from the images.

This method allowed preoperative MR images to be registered to intra-operative free-hand 3D ultrasound images to update changes in liver anatomy. The vessel probability maps for MR were generated by using a lookup-table. Each ultrasound probability map was created by examining the intensity of the 2D ultrasound image voxels and the magnitude of intensity dips along the ultrasound beam direction. Registration optimization was accomplished by iteratively changing all the rigid body transform parameters and selecting those that improve the similarity measure between the two modalities' probability maps. The authors tested their method on five subjects against "bronze standard" ground-truths created by manually point picking, and found that it was accurate to within 2.3 and 5.5mm which is sufficient for most liver procedures.

Chanwimalung *et al.*[35] proposed a method that registered overlapping small field 2D retinal angiographic images from the same patient by combining intensity registration and feature registration strategies. The method first extracted the retinal vessel tree to produce a binary image of the vessel. The image was then skeletonized to produce a set of vessel centerlines that could be further analyzed to detect vessel bifurcations. The binary images were then roughly registered using mutual information and translated for initial alignment. Corresponding bifurcation features and sampled vessel points were then found using the iterative closest point algorithm to produce a final registration by image translation. Affine linear transformation can be optionally estimated to determine it is necessary for image alignment, since the low image deformation in the small field images were usually not significant enough to require it. The method was tested on 504 pairs of retinal images and showed high

registration success, with 95% of the image pair registrations validated manually as being acceptable. The method was also robust to poor image quality and small image overlaps.

Barber *et al.* [16] proposed a vessel registration algorithm that effectively matched a reference vessel mesh model to the vessel structure in the angiographic image of a patient. This registration provided patient specific vessel lumen meshes for the computation of blood fluid dynamics and vessel shape in different cardiac phases. A binary vessel volume image was first generated from the reference mesh model and the patient's vessel image registered to it by optical flow. The inverse of the mapping generated through registration was then applied to the reference mesh model to produce the patient specific mesh model. The method was validated using the laser surface profiles of physical aorta and carotid phantoms as well as on clinical aortic images. The accuracy of their method was submillimetre with accuracies 2–3 times better than that of compared standard methods. The method is also 18 times faster compared to standard methods.

Mollus *et al.* [170] proposed a method to rigidly register liver 3D rotational XA data to a 2D DSA image. The 3D XA vessel features were first extracted and skeletonized to build a centerline model of the vessel tree, while the 2D image was left unprocessed. The 3D centerpoints were matched to vessel candidates in the 2D image by their in-plane orientations and then expected intensity profiles for typical liver vessel radii were used to locate a set of matching target points. The registration optimization between the projected 3D centerpoints and their 2D target points were done through the Levenberg-Marquardt least squares fitting algorithm

[139]. Experiments were performed on synthetic angiograms and 2 clinical data sets, which showed that the proposed approach was accurate, robust to preprocessing error, and has a large capture range.

Maeda *et al.* [149] proposed a 3D non-linear vessel registration method for aligning intrapatient thoracic CT images for temporal subtraction diagnostic procedures. The method registers vessel structures using a cost function that measures the registration overlap, using normalized cross correlation of image intensities and a vessel likelihood function that uses the structure's orientations and the eigenvalue vesselness measure of [140]. A smoothness measure assures that the author's multiscan free-form deformation was well behaved. Optimization was done using a Quasi-Newton method at multiple resolutions to enhance efficiency and robustness. The authors applied their method on 13 sets of thoracic CT images, evaluating the cross-correlation of the registered image, and found that their method improved registration accuracy by 8% compared to a non-vessel based conventional non-rigid method [214]. Using the vessel registration method also produced less registration caused subtraction artifacts at vessel structures.

Mitrovic *et al.* [169] introduced a robust 3D-2D rigid registration method for use in merging of intraoperatively acquired 2D cerebral C-arm image to 3D preoperative angiographic images for endovascular image-guided interventions. The method precomputes the 3D vascular model which consists of its detected centerline, local orientation, and radii, and matches them to the intensity and gradient orientations of the 2D image. The authors validated their method on ten clinical image sets and determined their registration accuracy by measuring the alignment error of fiducial

markers with their centroid coinciding with the centroid of the cerebral vessel tree. They determined that the method had a mean registration errors below 0.65mm with execution times below one second. The method also has the highest rate of success and largest capture range when compare with state-of-the-art methods.

2.2.4 Challenges

Vessel images and their vascular structures can be used for aligning medical images through image registration by vessel features, intensities, or by hybrid techniques.

Vessel registration methods can operate using explicitly extracted vessel features from the image. Vessel feature registration can be fast, robust to local minima, and highly accurate. However, the effectiveness of these registration methods can be heavily dependent on the quality of the extracted data. Feature extraction methods that miss too many vessel features or contribute too many artifacts and non vessel features, dramatically reduce the effectiveness of vessel feature registration. As well, depending on the vessel feature extraction method used, the total processing time needed to complete both feature extraction and feature registration may be quite high. Improvements can be made in feature-based vessel registration by improving vessel extraction, improving homologous feature matching, and reducing ambiguity of features by including more vessel parameters.

Vessel image intensities can also be quite effectively used for image registration. Such methods using vessel intensities have the benefit of not requiring feature extraction, which contributes overall processing time savings especially when the extraction method is computationally expensive. The fact that intensity based registration does

not involve feature extraction, also eliminates any of the extraction based issues of feature based registration. However, using image intensity for registration can be slow due to the amount of information that needs to be processed for image alignment. As well, the presence of other image structures can create local minima in the registration parameter space that causes a vessel-based intensity registration method to not properly converge to the expected solution. Improvements can be made to vessel intensity-based registration through the acquisition of better quality vessel images, through the tuning of imaging parameters, or improving of registration image similarity measures.

Hybrid vessel registration seeks to balance the benefits and reduce the shortcomings of feature and intensity based vessel registration. For instance in IGNS, the computationally intense phase of high quality feature extraction is often allocated to the preoperative stage. Doing this allows intraoperative registration involving intensity to feature alignment to be more efficiently completed and more robustly completed. As well, the extent of intra-operative feature extraction can also be controlled, such that the extraction process does not completely remove all image intensity information. This strategy can reduce computation time and the possibility that the extraction method removed too much vessel information or misidentified vascular features. Such balancing and reallocation of aspects of improved feature and intensity based vessel registration method can be used to create novel and improved hybrid registration methods.

2.3 Cerebral and Vascular Imaging Phantoms

The accuracy and measurement reliability of medical imaging devices and the results produced from image processing are highly important if diagnostic decisions and surgical guidance are to be based on the data. To assure these criterion are met and also to understand the specific characteristics and limitations of an imaging device that acquired them, medical images need to be compared against objects of known dimensions with defined and reproducible imaging parameters. These objects are known as medical imaging phantoms.

Medical imaging phantoms are used in situations where verification of an imaging device or an image processing algorithm is required. Such verification is required if image data are acquired or processed using novel techniques, and particularly so if the different modality images are to be compared and their information merged for further processing. The creation of anthropomorphic cerebral phantoms can help in such verification, especially if they contain anatomical structures that are important for validating specific imaging modalities or image processing techniques. Developing anthropomorphic phantoms can thus enable more control and confidence in the reliability of one's imaging work-flow results.

The focus of creating more anthropomorphic cerebral phantoms for validation for image processing and medical imaging is a relatively recent trend in the development of medical imaging phantoms. While there was early development of phantoms and phantom tissue mimicking materials for characterization of brain imaging modalities, [212, 102, 148, 215, 147, 154, 19, 89], the constructed head and brain phantoms were typically non-anthropomorphic until the late 1990's.

One of the first truly anthropomorphic cerebral phantoms was created by McCullough [159]. The author developed the head phantom for CT geometry validation that simulated the bone and soft tissue, with different imaging validation inserts that can be placed into the brain space. A custom cast version of a commercial skull model was cut open and modified with an acrylic plate to be able to hold water, as the soft-tissue mimicking material, along with geometric size, high imaging contrast, and low imaging contrast inserts. The phantom was used to evaluate reconstruction software for the EMI CT scanners at normal and lower radiation dose imaging, and demonstrated that such phantoms can be useful for evaluation of CT scanner performance and to enable effective quality control procedures.

To validate positron emission tomography (PET) imaging accuracy, Hoffman *et al.* [101] created a realistic brain phantom that simulated emission activity distributions found in the human brain in cerebral blood flow and metabolism studies. The phantom was fabricated from thin acrylic sheets with sections cut out to represent and allow differentiation of cerebral spinal fluid, grey matter, and white matter in the final PET images. Multiple sheets of acrylic were cut, each representing the tissues that would be visible in a certain axial slice. All the sheets were then aligned, stacked, placed in a container with radioactive tracers and imaged. The result from the phantom showed sufficient brain anatomy to be able to estimate the limits of accuracy of PET brain imaging.

Rice *et al.* [205] created an anthropomorphic multi-tissue MR head phantom to test MR structure localization and for spectral analysis of the MR signal. The phantom consisted a subcutaneous fat layer simulated using safflower oil which surrounded

a cylinder of brain tissue mimicking material made of gelatin and agar containing brain metabolites. Cavities for the nasal sinus and the ventricles were also created, with the latter holding a simulated cerebrospinal fluid made of water and copper chloride solution. The T1 and T2 magnetic relaxation times of the phantom tissue were very close to that of *in vivo* brain tissues and the different levels of metabolites are detectable via MR spectroscopic analysis. The author believed that the well-characterized tissue mimicking properties of the phantom made it useful and a clinical reference and in testing MR spectroscopic methods.

Fahrig *et al.* [75] was the first to create a full polyester cerebrovascular arterial flow phantom for use in XA, MRA, and CTA, extending the casting methods of [229] using low-melting temperature alloys. The cerebral arteries were cast as four large vessel core components consisting of the circle of Willis arteries, the internal carotid arteries and the basillar artery using the aforementioned alloy. Each component was then bent to the required 3D shape and connected together using small wooden plugs that can be removed after casting. An aneurysm made of the same alloy were glued to the vessels. The entire vessel core setup is placed in polyethylene housing and a polyester resin is poured around the alloy components to cure. After curing, the phantom was placed in a hot water bath to melt out the metal alloy. Any residual metal was removed using a dilute nitric acid solution. The phantom was then connected to a computer controlled pump for testing using iodinated contrast agents for the x-ray imaging modalities and water for MR imaging. The phantom was found to be geometrically accurate, and its flow dynamics mimicked that seen in vivo. The authors stated that images of the phantom in XA, CTA, and MRA

were consistent with those image using the same modalities under real physiological conditions.

The development of poly-vinyl alcohol cryogel (PVAc) material was an important step in producing ultrasound imagable multimodal brain phantoms. The material was first described by Peppas [183] and used first used for developing MR phantoms by Mano *et al.* [154] who recognized its long-term stability, mechanical resistance to rupture, and similarity to human tissue in both texture, water content, and relaxometry times. Due to its elasticity and toughness Chu and Rutt [41] recommended its use in validating MRA measurements under pulsatile flow. Comeau *et al.* [48] used PVAc to create a semi-realistic brain phantom that can be imaged in MR and ultrasound modalities. The phantom consisted of a cast flat disk of PVAc embedded with a ridged brain-hemisphere simulation made of different concentrations of PVAc that contained fluid filled spaces to simulate vessels and ventricles. The phantom could be precisely deformed and the tissue movements tracked with ultrasound and MR images using the phantom's vessels and ventricle features. The tracked features allow the deformations to be subsequently corrected through image processing and validated using the known phantom geometries and applied deformation parameters. The tests with the phantom showed that good ultrasound and MR imaging can be performed and that it can be used for validation of non-linear registration algorithm for image processing. The phantom was used by Gobbi and Peters [88] to demonstrate and validate their multimodal registration methods and the general nonlinear software package they also created.

Surry *et al.*[240] further characterized the ultrasound, MR, and physical properties of PVAc and exploring its application to phantom fabrication. The authors built a dual hemisphere anthropomorphic brain phantom using stereolithography to create the mold to cast the PVAc. The digital model of the phantom was based on [103] and was edited to remove all tissues below the canthomeatal plane to also reduce the brain's sulcal depth to enable effective casting and phantom removal. The authors also built a PVAc blood vessel phantom containing two branched vessels. The brain phantom can be easily imaged in ultrasound and in MR, showing the central sulcus and the shallow sulci in both imaging modalities. The authors demonstrated that PVAc can be used in multimodal imaging, for tissue biopsy accuracy studies, and provided guidelines on how to best handle and use PVAc for phantom construction.

Reinertsen *et al.* [199] extended the work of Comeau *et al.* [48] and created a realistic ultrasound and MR imageable brain phantom. The brain component of the phantom was constructed by filling a commercially available brain mold with PVA solution and inserting two loops of plastic tubing to act as brain vasculature. The brain component was then cured and placed with a circular disk of PVAc into a cylindrical container with an inflatable catheter. The catheter allowed the finished phantom to be precisely deformed by inflating it with precise quantities of fluid. All the contents in the cylindrical container were then immersed in PVA solution which was then cured to create the final phantom. The phantom's deformations were found to be reproducible with millimetre accuracy and imaged well under MR as well as b-mode and Doppler ultrasound imaging modalities. The phantom was later used

by the authors to validate the vessel-based registration method that they developed [202, 201].

A large amount of development for anthropomorphic phantoms and innovation on multimodal tissue mimicking materials have occurred through the design of vascular flow phantoms. With the development of flow imaging in MR, CT, and ultrasound modalities, the measurements and unique artifacts from these modalities had to be characterized. This necessitated the creation of vessel structures in these phantoms that realistically simulated the more complex anatomical form of blood vessels, as well as the creation and inclusion of vascular pathologies and lesions. Multimodal tissue mimicking materials that closely match the biological imaging characteristics of *in vivo* tissues in MR, CT, ultrasound, and optical modalities had also been developed for vascular phantom due to the need for inter-modal flow rate validation. As well, the necessity of good image alignment between multimodal images of the phantom for comparison has also spurred the exploration of multimodal imagable fiducials in vascular phantom.

Due to the accuracy needed to manufacture them and their complex structures, designers of vessel phantoms were also early adopters of computer aided manufacturing and other rapid prototyping technologies in mold production. They have also introduced more sophisticated casting techniques for phantom fabrication including lost material and multi-layered casting methods.

Based on this research and development, vessel flow phantoms with complex structures, containing multiple pathologies, built from multimodality tissue mimicking materials can be constructed. Many of the sophisticated production methods

and advanced materials developed from vascular imaging phantoms can be applied to improve anthropomorphic cerebral phantoms.

It should be noted that many earlier imaging phantoms, including vessel phantoms, are now available from commercial vendors. However, the aim of this section is not to exhaustively summarize all present vascular phantoms. Rather, we seek to provide a brief overview of the serial development of vascular imaging phantoms fabrication methodology over the last three decades.

Vascular imaging phantoms are indispensable for evaluating and characterizing angiographic imaging devices and vessel image processing algorithms. Accordingly, these vascular phantom have evolved in conjunction with the testing needs of developed imaging devices and processing methods. Some of the earliest vessel phantoms were primarily static and used for the imaging sharpness and geometric verification of x-ray angiographic imaging modalities [212, 102, 215]. However with the advent of vascular imaging centred on blood flow, more sophisticated phantom were built to allow quantification of flow velocities and observe potential flow imaging artifacts. Multimodal vascular phantoms were eventually developed due to the need of cross-modality imaging verification and to test multimodal image processing methods.

Vascular phantoms vary in structural complexity and anthropomorphic similarity. In the simplest cases, a vascular imaging phantom may just consist of a set of tubes and catheters to act as the vessel mimicking material. They may or may not circulate a blood mimicking fluid to simulate either steady or pulsatile blood flow. The tissue mimicking materials used may be simply solid plastic or plain water to more advanced mixtures or layered emulsions. These simple phantoms fulfil

the most basic imaging requirement of a specific modality and due to their ease of fabrication are still commonly used for verification. However, more sophisticated vascular phantoms have been developed to and constructed to evaluate more specific characteristics of different imaging modalities and as such will in addition contain bifurcations [82, 229], different vessel tortuosities [75, 5], varying degrees of stenosis [262, 31, 231], and may have multiple layers of vessel mimicking tissue to simulate different vascular tissues (i.e. the intima, media, and adventitia) [60, 22, 24] and pathologies (e.g. sclerotic plaques, calcifications) [57, 56, 24]. Fiducial markers are also commonly embedded in the phantom to assure proper image alignment over multiple images and various imaging modalities [82, 118, 45]. For more realistic phantoms with greater similarity to biological tissues, *ex vivo* vessels and organs are sometimes used to produce vascular phantoms [57, 118].

In the rest of the section, we provide a brief overview of vascular phantoms that have been developed over the last few decades for validation and verification of various medical imaging modalities. We organize the review of vascular phantoms according to their imaging modality; for x-ray, MR, ultrasound, and optical imaging, with an emphasis on the development anthropomorphic multimodality vascular phantoms.

2.3.1 X-ray and CT Imaging

X-ray modality vessel phantoms were first developed for measuring the size of vessel pathologies in contrast-enhanced x-ray imaging. Wise et al. [262] created a carotid aorta phantom specially designed to study the scanning parameters for CTA imaging on conventional versus spiral CT imaging devices. The phantom was

constructed of a solid polymer cylinder that had the density of soft tissue. Holes with different percentages of stenosis, stenosis length, and angles of stenosis relative to the CT scanning axis were drilled into the cylinder to form vessel lumens. The drilled holes were plugged and filled with a non-ionic contrast solution that has a CT density of 240 Hounsfield units. By scanning this phantom and analyzing the image with its known physical measurements, the authors noted that while there is little difference between conventional and spiral CT imagers, a thinner and longer stenosis was imaged with higher accuracy in CTA imaging. Vessel angles also caused degradation in image quality with increased halo and edge artifacts.

Later x-ray modality vascular phantoms were improved in anatomical realism to enable actual implantation of stents and used for the *in vitro* visualization of these implants. For instance, Winder *et al.* [260] built an aortic phantom containing a stent graft for testing CTA scanning and visualization of the scanned data. CT data from a patient was manually segmented and thresholded and a mesh model was built using the marching cubes algorithm. The mesh model was then physically constructed using stereo lithography in two parts which allow a commercial aortic stent graft to be seated or removed. The vessel phantom was filled with a contrast solution and scanned at various slice thicknesses, pitches and reconstruction intervals. The phantom image was visualized using virtual intravascular endoscopy (VIE) to validate stent placement. The phantom can be used to find optimum scanning parameters for aortic stents and also allowed the authors to notice potential pitfalls of virtual endoscopic visualization in overestimating stent wire diameter and vessel wall indentation caused by the stent's wires. This work was later extended by Sun

and Ferris [239] to study the effects of CT collimation and found that higher section thickness can distort aortic vessel ostiums in VIE. The authors noted that acquiring CT scans of optimal section thickness for proper visualization must be balanced with the patient's radiation exposure.

More recently, Thakur *et al.* [245] designed and constructed a multipath acrylic phantom for the training of neurovascular catheter insertion and manipulation guided by 2D fluoroscopy. The phantom contains vessels of different diameters, angulations, and changes in diameter transitions. To create the phantom, two acrylic sheets were milled in mirror image using a numerically controlled machine with a hemispheric bit to ensure cylindrical vessels when the two sheets are aligned and fastened. Fluid connectors were attached to the inlets and outlets of the phantom to allow a pump to be connect to fluid circulation. A connector is attach to the inlet to the phantom to allow the catheter to be introduced to the phantom. The phantom imaged with good contrast in 2D fluoroscopy and radiographs, and functions well with inserted catheters. The authors believe that it can be used for training safe catheter handling and for the assessment of new catheter guidance techniques. As well, the materials of the phantom are stable to temperature other environmental factors thus giving a long usage lifetime.

2.3.2 MR Imaging

Vascular flow phantoms for MR imaging have been developed for determining the accuracy of the flow rates and characterization of artefacts arising from the imaging modality. Meier et al. [162] introduced a vessel phantom for their tests to quantitatively determine blood flow rates in MR in real-time over an entire heartbeat

interval. The phantom was constructed from a round, water-filled cylinder embedded with 4 interconnected acrylic tubes of two different internal/lumen diameters. The blood mimicking fluid was a solution of water and $CuSO_4$ which was fed through the phantom's acrylic tubes by either pulsatile or continuous flow. The phantom accurately determined the flow rates, which matches that of *in vivo* MR and ultrasound measurements done on the abdominal aortas of healthy human subjects.

To verify the accuracy and quality of novel MRA techniques, in 1999, Smith *et al.* [231] developed an anthropomorphic carotid bifurcation phantom with vessel stenosis. Different MRA imaging modalities were tested and their geometric accuracy and imaging appearances were characterized. This work extended upon the technique for producing multimodal phantom in [229]. An aluminium mold was precision milled using computer assisted manufacturing (CAM) to first cast the lumen of the vessel phantom. The casting material used is a low temperature melting metal alloy. This metal cast was then itself encased in a polymer resin. By heating the polymer encased cast, the low-melting point alloy cast is removed, leaving an accurate hollow polymer vascular phantom. A blood mimicking fluid of water and glycerol was pumped through the phantoms and imaged using 3D TOF, 2D TOF, and 3D PC MRA. Using of the phantom allowed the authors to identify imaging artifact in each MRA technique and shows its usefulness for the assessment and characterization of newly developed MRA techniques.

To produce an MR compatible phantom that behaves like biological tissues when heated using high intensity focused ultrasound (HIFU), Payne *et al.* [180] created a *ex vivo* kidney vessel phantom for MRA to identify significant blood vessels in planning

HIFU treatments. A specially prepared alcohol fixed canine kidney was cannulated at the artery, vein and ureter and then suspended in an alginate filled plastic holder inside a large vat of water. A focused ultrasound heating element was place in the vat of water and the phantom was sonicated near the kidney vessel as required. The kidney phantom was perfused at different flow rates with distilled water while being imaged using 3D TOF MRA. The authors indicated that the kidney vessel phantom can used to evaluate, test, and plan MR guided HIFU therapy. Using the phantom, MR protocols and be tested and tuned to improve organ tissue or vessel imaging. The heating and cooling effects of HIFU and the flow rates of close-by vessels can also be quantified. However, perfusion rates must be controlled to prevent damage to the vessel in the phantom, which can result in poor imaging.

2.3.3 Ultrasound Imaging

The used of phantoms for validating Doppler ultrasound is an important and ongoing research topic that extended from early research in medical ultrasonograhy. Law *et al.* [133] discussed the important aspects of designing ultrasound compatible flow phantoms. Their review delved into the phantoms from preexisting literature going back to the 1970s regarding the types of blood mimicking fluid, tubing used for the vessels, the types of pump used for circulation and the specific use of the phantom. The authors proposed their own phantom for validating Doppler ultrasound under steady blood flow using a vessel phantom built from thin-walled polyethylene tubes connected to peristaltic pumps under gravity feed that circulate a fluid suspension of chemically-fixed red blood cells. The authors indicated that the phantom setup appears to be useful for Doppler ultrasound studies in pulsed and continuous blood

flow, for use in stenosed vessel phantoms to aid in diagnostic quantification, and to study the scatter of ultrasound by red blood cells.

To overcome the limitations of vessel mimicking materials in vascular phantoms produced, Rickey *et al.* [206] introduced a wall-less vessel phantom consisting of only tissue mimicking material for studying Doppler ultrasound flow. While rubber tubing can be used to mimic blood vessels, the material has high ultrasound attenuation, which may introduce measurement errors and artifacts. By removing the tubing and using the paranchymal tissue mimic directly as the vessel, the acoustic impedance between the vessel and the lumen can be reduced. The phantom was constructed by pouring their formulated dissolved tissue mimic, consisting of agar, cellulose particles, and glycerol into a prepared container with a cylindrical aluminium bar. The vessel was formed when the agar was set and the mandrel was removed. The blood mimicking fluid was a mixture of metal machining fluid, water, and nylon particles for ultrasound scattering. The proposed vessel phantom did not cause shadowing and also does not distort the ultrasound's beam power spectra. Due to this, the phantom can be used to precisely measure Doppler signal sensitively and validate flow rates in small and thin vessels. The work also showed the importance of choosing low attenuating materials for use as vessel mimic. The tissue mimicking materials and methods for producing this phantom was eventually widely adapted and used as a basis for the development of many modern vascular phantoms.

De Korte *et al.* [60] improved upon the the wall-less phantom by introducing a technique to produce multiple vessel tissue layers using different tissue mimicking materials. The phantom was created for the purposed of validating elasticity

measurements in intravascular ultrasound (IVUS). Vessel tissue mimics of different densities were formulated using different quantities of agar in a gelatine solution, with silicon carbide powder added for scattering. The phantom was constructed by pouring the vessel mimic into a syringe and agitating it until the fluid has almost set. A "lumen tube" is then inserted down the centre of the syringe, the tissue was allowed to set completely, and the tube was finally removed to create a vessel lumen. Layered vessels with lesions of different echogenicity and hardness were created through the same technique by repeated casting of the lesion material before introducing the lumen tube. To measure the vessel elasticity and hardness, the IVUS probe was inserted into the phantom which was pressurized with fluid from the other end of the phantom. Compression was applied to the phantom and scans were made to produce the strain image of the vessel phantom. The strain images were able to map the hard and soft legion tissue mimics despite the same being not always visible in the echogram images.

Brunette *et al.* [22] developed a three-layer vascular phantom with different vessel tissues and wall thicknesses for use in IVUS. An aluminium mold was machined with two female components and a male vessel lumen component. The mould was designed to have four different vessel lumen diameters and a slight offset on the mandrel to allow for different vessel wall thickness. The outside and innermost layer of the vessel mimicking material used is an agar gel solution with cellulose particles while the middle echolucent materials lacked the cellulose but contained glycerol. The layers were applied by dipping the mandrel in layers of the different agar solutions once each layer have sufficiently cooled. When imaged using IVUS,

the phantom was able to robustly reproduced the characteristic different layers of the large arteries and is more realistic in geometry and ultrasonic properties than phantom made from different materials and can be used to validate automatic segmentation or tissue characterization methods. Potter *et al.* [194] used this method to construct a similar single material agar artery phantom in order to quantify how adjustments to ultrasound parameters and probe distances changes vessel lumen and wall thickness. The lumen diameter appears to significantly reduce with increases in gain and probe distance while vessel wall thickness increased with gain and varied inconsistently with probe distance. The study showed how reported clinical measurements using ultrasound needs to specify or document the dynamic range and probe distance for their studies.

Landry and Fenster [129] introduced a wall-less agar phantom embedded with different carotid plaque lesion bodies to determine the accuracy of reconstructed 3D B-mode ultrasound images in measuring plaque volume. A tissue mimicking material consisting of agar solution, glycerol, and cellulose powder was cast in a container around an acrylic mandrel and cooled to create the vessel lumen and surrounding tissues. Plaques were created from the same tissue mimic but with only one sixth of the cellulose and measured to determine its weight, which relates to its volume by the material's density. Twelve plaques of different heights and lengths were created, and then glued inside each phantom's vessel lumen. The phantom were then filled with a glycerol solution, plugged, and placed in water for storage. When imaged, the authors found that the phantom produced ultrasound volume measurements that were within 3.1% of the actual volume.

To create more wear resistant vascular phantoms using newly available ultrasound compatible materials, Poepping *et al.* [191] fabricated a thin-walled silicone rubber vessel flow phantom for Doppler-flow studies based on anatomically accurate digital geometric models derived from the work of [230]. Although wall-less phantoms have less mismatch problem to the tissue mimicking material they are vulnerable to damage from usage, environmental changes, and have incompatibility to certain blood mimicking fluids. The authors constructed the vessel mimicking material using a two-part cured silicone rubber with varying concentrations of cellulose powder to allow for enough ultrasound scattering without increasing the attenuation of the vessel. The methods for casting the vessel is similar to [229] in which a low-melting-point alloy vessel core is cast. However for this phantom, a additional mold is used to cast the vessel mimic around the lumen core before being placed into the tissue mimic before the core is melted out. The authors found that the vessel phantom is stable over time, environment and usage stresses. The elastic modulus of the vessel wall also mimicked that of human arteries.

To enable study of ultrasound guided HIFU, Greaky et al. [90] designed a pulsatile flow phantom made of a real carotid artery for HIFU transcutaneous hemostasis of injured blood vessels. The vessel flow phantom is similar to [56] was built from an *ex vivo* porcine carotid artery that was imbedded in agarose gel to stabilize it and the setup was connected to a pulsatile pump system. Heparinized blood was circulated in the phantom and needle was used to puncture the artery. The ultrasound imaging probe and HIFU transducer were then used to guide the focus of the transducer and the seal the arterial puncture, respectively. The entire process of pulsatile flow,

arterial puncture, and puncture sealing can be visually confirm as well as through Doppler ultrasound imaging from the ultrasound probe. The authors believe that the designed phantom can provide a controlled and repeatable setup for studying the application of HIFU for hemostasis in a variety of vessel injuries.

Less anatomically accurate ultrasound vascular phantoms were also built to charaterize newer imaging modalities and to study effect of imaging parameters on ultrasound measurement accuracy. Hammer *et al.* [95] developed arterial wall motion phantom to validate software that measure such motion using tissue Doppler ultrasound image (TDI). The phantom consists of a two slabs of agar tissue mimicking material, with one attached to a static ultrasound probe and another on a mechanically controlled moving paddle. The setup simulates ultrasound imaging done in the lateral cross-section parallel to the arterial vessel axis. By adjusting the paddle's motion different wall displacement, velocities, and accelerations can be simulated. In experiments, the paddle's motion is controlled using a stepper motor controller which when validated with a laser, yielded a positional accuracy of around 36 micrometers. Testing the software with, the phantom the authors found that TDI methods of resolving displacement was highly accurate. However, the software became less accurate with decreased wall displacement and increased wall movement velocity.

As well, Schulten-Wijman *et al.* [218] developed a phantom made of polyurethane tubing to determine the influence of ultrasound settings on Power Doppler ultrasound measurements. Plastic tubing was immersed in a mixture of water and ultrasound coupling gel. The tubing was set at an angle of 45 degree to the liquid surface and

a commercial blood mimicking fluid was circulated through the phantom. Using the phantom the author found that power Doppler can significantly overestimate vascularization index within a region of interest depending on vessel size, and that clinical interpretation of the index should take this fact into account.

2.3.4 Optical Imaging

Optical imaging modalities can be used to accurately determine the blood flow rate and characterize the turbulant flow dynamics inside stenosed arteries. Vascular phantoms built for optical modalities need to be transparent to visible light in order allow the proper acquisition of camera footage for tracking the flow dynamics of particles in stenosed vessels.

Cao and Rittgers [31] created a optically transparent silicone rubber stenosed phantom to study platelet adhesion in vessel pathology. The vessel was cast by creating a vessel lumen core out of wax, carving the wax to produce the "negative" of a stenosis plaque, and then coating sufficient silicone polymer on the carved wax core to fill the plaque negative and coated it with approximately 2mm of the material. The silicone was than cured and the wax is melted out to form the phantom. The phantom was then embedded in a viewing box with heavy mineral oil to reduce optical refraction. The blood mimicking substance used was a solution of distilled water and dextran circulated by a pulsatile pump to simulate cardiac cycles. Resin particle approximately the size of platelets were injected into the phantom slightly upstream of the stenosis and the flow of the particles are recorded using a video camera for analysis. Through their experiments, the found that with that 75% and

95% stenosis created enough particle resting time downstream from the stenosis that may be enough to initiate blood clot formation under physiological resting conditions.

Improving on the realism of the previous phantom, Brunette et al. [24] described a multi-layer silicone rubber coronary artery phantom for particle image velocimetry (PIV) to experimentally observe flow over atherosclerotic formation. The phantom extended upon the multilayered ultrasound vascular phantom of [22], substituting the tissue speed-of-sound matched agar mixture for optically transparent silicone rubber. The vessel phantom was made by injection casting silicone polymer into precision machined aluminium molds. Five two-pieced female mold components were created to mold the sclerotic occlusion for the stenosis and layers of arterial tissue around a male mold component representing the vessel lumen. The finished vessel phantom was embedded in a transparent polycarbonate container filled with a similar refractive indexed water and glycerol solution. The blood mimic is the same water and glycerol mixture with titanium dioxide powder included for laser tracking. The multilayer phantom was tested in a PIV flow analysis system and was able to supply usable experimental data. The authors believe that this data can be used to validate computational fluid dynamics algorithms and hypotheses. This phantom was later adapted for used by Brunette *et al.* [23] to study 3D blood flow characteristics by scaling the phantom up by 6.35 times while keeping the blood mimic, circulation setup, and data acquisition the same as in the previous experiments. Particle velocity was calculated and used to derived vessel shear stress distribution and secondary flows with the flow volume. Results from their experiments showed that abnormal

shear stresses are initiated even at early stages of sclerotic formation are important contributors of disease progression and also plaque rupture.

Cimalla *et al.* [44] proposed a method for determining blood flow velocity using intraoperatively injected fluorescence dyes for neurosurgery. The vessel phantom consisted of silicone tubes circulated with water a the blood mimic, the fluorescence dye bolus is injected as a suspension of water, whey protein, and dye compound. The bolus injection is recorded as a digital IR fluorescence video and the data is analyzed. From their experiments, the author found that the fluorescence can be used to determine the accuracy of flow velocity by $\pm 20\%$ which is comparable to clinical Doppler ultrasound measurements.

2.3.5 Multimodal Imaging

Balancing the desired material properties for multimodal imaging is important such that a phantom constructed with these material can be effectively used in its prescribed imaging modalities. Frayne *et al.* [82] constructed one of the first multimodal anatomically realistic carotid artery vessel phantoms. A digital model averaged from multiple human carotid bifurcations was numerically machined onto acrylic slabs to create a two halves of the artery phantom. Water soluble wax was cast in the mold, allowed to solidify, removed, and then thinly coated with a polyester resin. By dissolving the wax in water a thin polyester plastic phantom is left. This plastic component was then mounted into a plastic housing and embedded in a tissue mimicking material consisting of agar, propanol and cellulose powder. A blood-mimicking fluid made of cellulose powder, machine cutting fluid, and water can be circulated through the phantom. The phantom was surround by lead wire as

a fiducial material which can be used for multimodal image alignment. Both the blood and tissue mimicking materials can be successfully images in x-ray, ultrasound and MR modalities, with the latter seeing dark wires in contrast with the tissue mimicking material. The physical phantom was geometrically accurate, with flow images and flow measures acquired on the phantom with Doppler ultrasound and phase contrast MRA agree with previously published data.

Renaudin *et al.* [204] designed a hard plastic 3D anthropomorphic coronary artery phantom capable of being imaged using contrast enhanced 3D MR and CT. Computer modelled coronary arteries were extracted and a digital model with empty vessel models were printed using stereolithographic methods to create the physical phantom. The empty vessel lumen of the rigid printed plastic phantom can be filled with gadolinium or iodine based contrast agents for 3D T1 gradient echo MR or 2D and 3D XA imaging. By using computer aided design, a physical phantom of highly accurate and realistic branching vessels can be consistently fabricated. The authors, indicated that the phantom's accuracy and ease of production allows it to be widely used for radiological validation, imaging quality control, and used in clinical field for training in angiographic interventions.

A highly influential set of methods for the creation of wall-less anthropomorphic triple multimodality vascular phantoms 3D and 2D XA, 3D MR, and 2D Doppler ultrasound was described by Smith *et al.*, 1994 [229]. The author's vascular flow phantoms can be built to emulated healthy carotid vessels or stenosed vessels. The phantom was fabricated by casting formaldehyde agar gel around a vessel core for

lost material casting. The core was in turn constructed using a low melting temperature alloy (Cerrolow 117) that was cast in a numerically machined aluminium mold. Melting away the alloy vessel core after the agar mixture had set leaves an agar gel with an evacuated lumen that can be fitted with tubing for used as the multimodal vascular phantom. Three carotid bifurcation phantoms were created with different anatomies; a normal, a 70% concentric stenosis, and a 70% eccentric stenosis in the internal carotid artery. The phantom were tested on x-ray based systems for DSA and CTA, magnetic resonance scanners for MRA and ultrasound imaging devices for Doppler angiography and showed promising similarities to images acquired from real tissue.

In order to create a highly realistic flow capable vascular phantom compatible with x-ray and ultrasound imaging, Dabrowski *et al.* [57] used a real human abdominal aorta. An abdominal aortic artery was harvested through autopsy, cleaned, and preserved in a low formaldehyde solution. The prepared artery was then mounted into a box, cannulated to acrylic tubes, tested for leaks, and box was filled with the tissue mimicking mixture specified by [206]. Stainless steel balls were embedded into the agar to act as registration fiducials. The lumen of the vessel was not perfused, but rather, filled with a water and glycerol solution, chosen for its low refraction index. The phantom was then evaluated using 2D XA, 3D CT, and 3D B-mode ultrasound imaging, which showed good overall correlation between the imaged lumen shape, plaques, and calcification features within the phantom. The anatomically realistic imaging properties of the phantom makes it attractive for evaluating imaging techniques in x-ray and ultrasound modalities. As a follow up to this work,

Dabrowski et. al [56] extended the testing of this real aorta phantom for use in flow imaging in 3D power and 3D colour Doppler ultrasound. The authors found that the phantom can be imaged well under Doppler ultrasound imaging modalities and generated more realistic flow patterns than purely artificial test phantoms. By using real human vessels with atherosclerotic plaques, the blood flow around these lesions can be better studied and characterized.

Using novel materials, Cloutier *et al.* [45] created a thin-walled multimodal vessel phantom with a longer shelf-life than wall-less phantom that contained imagable fiducial markers capable of being clearly imaged in XA, CTA, MRA and ultrasound angiography. The phantom was constructed using a agar and oil emulsion as the tissue mimicking material that was embedded with small glass sphere fiducials. The spheres were places in precisely known locations in the phantom to aid in viewing and in inter-modality registration. The phantom contained a thin latex walled vessel cast from a vessel core made from a low-melting point alloy using methods similar to [229]. In verification tests, the fiducials were highly visible and did not produce artifacts or distortion in all imaging modalities. The use of a thin walled vessel isolated the tissue mimic and prevented from desiccation while preventing gadolinium MR contrast-agents from leaking into it. The authors verified that the manufacturing process did not alter the phantom's precise geometry. For this reason, it can be used for imaging calibration, multimodal image registration validation, and other intra and intermodality comparative studies of medical imaging systems. Using this phantom, Boussion *et al.* [21] published a study that determine the accuracy of CTA,

MRA, b-mode ultrasound angiography, and IVUS in estimating of the phantoms vessel size and for cross-modality vessel registration. Using the phantom's images their compiled results indicated that CTA and IVUS were better for geometric accuracy, while CTA to MRA-based image alignments had the best accuracy and robustness for multimodal lumen border registration.

Sulaiman *et al.* [238] developed an x-ray and MR compatible non-rigid aortic arch aneurysm phantom for *in vitro* evaluation of new stent designs. The vessel phantom's mold was made by first producing a digital model of a patient's aortic arch, and then using it to create molds through stereolithography for the vessel phantom's lumen and for the vessel's outer wall. A wax lumen core was cast from the lumen mold and then used with the mold from the other wall to cast the vessel phantom using silicone rubber. Melting away the wax core produces the final silicone phantom. The completed silicone aortic arch phantom was attached to a pump that circulated a blood mimic consisting of water and a red-coloured radio-opaque dye. Stents were deployed at the phantoms aneurysm and found to attach snugly without perceivable leakage. The authors believe that such phantoms can be used for training stent placement and can help in presurgical patient-specific stent selection. They also found that the presence of a physical phantom helped the surgeon and radiologist become more familiar with the vessel and its pathology to optimize treatment approach and anticipate problems.

Allard *et al.* [5] proposed a new casting material for use in producing multimodal vascular flow phantoms that can be used in x-ray, MR, and ultrasound modalities.

The authors extend upon the work of [45] and introduced the used of isomalt, a commercially available sugar alcohol, for replacing a low-melting-point metal alloy for lost-material casting processes. Liquid isomalt was cast in a silicone mold fabricated using stereolithographic methods and the resulting cast was coated in a polyurethane membrane to create a thin wall to isolate the blood mimic from the tissue mimic in the completed phantom. The coated cast was then encased in an agar and oil tissue mimicking material and the isomalt was dissolve in water. The authors compared vessel phantoms built using isomalt to that built with previous method using low-melting-point alloys and found that isomalt did not leave residuals that caused imaging artifacts in MR and x-ray modality imaging methods. The geometric accuracy of phantom made using isomalt was comparable to that manufactured with the alloy. The authors indicate that using isomalt allows complex vessels with multiple stenoses and other lumen irregularities to be easily manufactured with leaving residuals.

Jiang [112] created a bifurcated vessel phantom to that can be used to investigate heating and thermodosage of vessel tissue in HIFU treatment. The vessel mimicking material used is a silicone polymer mixed with a thermosensitive powders that changes colour when heated. The vessel phantom was itself manufactured through lost-wax casting of a digitally modelled vessel lumen core. The authors tested the phantom with perfused with water under HIFU sonification and found that the physical properties of the phantom agree well with those of human tissue, and can be used to display thermal dosage profile for HIFU experiments.

King *et al.* [118] constructed a set multimodal renal artery phantoms using the fiducials and low-melting-point alloys casting methods described by [45] and the tissue mimicking materials proposed by [244]. Renal artery vessel phantoms with stenosis of 0% to 85% were created and imaged with ultrasound, MR, CT, and XA. The phantom was imaged in water for ultrasound and in air for all other modalities. The authors reported that the images acquired from the phantom in all modalities were distortion free and with good contrast between the background tissue, fiducials, and vessel lumen. Discrepancies in the estimation of stenosis in the higher-stenosed phantoms between the imaging modalities were evident. From their tests, the authors believe that their artery phantoms can be useful in evaluating current and emerging imaging technologies.

Allard *et al.* [4] created a multimodal aortic aneurysm vessel phantom with an visible thrombus to be used in x-ray, MR, and ultrasound imaging modalities. To create this phantom, molds was fabricated for the vessel lumen as well as the thrombus using method similar to that described by [5]. A novel formula for abdominal tissue mimicking materials was developed consisting of agar, glucosamine, oil, sodium azide and water. The tissue mimicking material used for the thrombus consisted of agar, glycerol, cellulose powder, sodium azide, and water. The thrombus material was clearly visible in MR and CT imaging modalities as a hypointense feature, while being hyperintense when imaged using ultrasound. The tissue mimicking materials developed in the phantom matched the *in vivo* CNR and SNR values of T1 and T2 MR sequences. As well, the materials' x-ray absorption and ultrasound propagation speeds matched that of *ex vivo* biological tissue. The phantom is not only useful for

validating imaging methods and processing techniques, it can also be used to train for planning and training fluoroscopic-guided stent graft deployment.

2.3.6 Challenges

Imaging phantoms of each modality have their own unique constraints and complexity since the materials used for their construction should act in a similar manner to real tissue in a specific imaging modality. For phantoms in x-ray based modalities such as CTA and XA, x-ray absorption and transmission properties must be matched, just as in optical imaging modalities the tissue mimicking material must allow for sufficient light transmission. In MR modalities, the magnetic relaxation times of the vessel and tissues should be similar. And for ultrasound imaging modalities, the material must have similar speed of sound, ultrasound scattering qualities, and ideally similar rheological properties to biological tissues. Furthermore, any fiducial markers in a phantom should show up with high contrast in respect to the rest of the phantom tissue and their location should be able to be unambiguously identified.

Multimodality anthropomorphic imaging phantoms are challenging to build. The tissue mimicking materials that are compatible in one imaging modality may not be optimal for another. This is also challenging for multimodal fiducials, since it must be able to be imaged in each imaging modality without causing significant image distortion or artifacts and still be unambiguous in each modality. As well, the complex anatomical forms in a real biological tissue are often difficult to properly fabricate in anthropomorphic phantoms.

We believe that the methods developed in multimodal anthropomorphic vessel phantoms can be used to improve cerebral imaging phantoms. This includes applying the developed multimodal materials and also extending the techniques used to fabricate anthropomorphic vessel phantoms. Through this, more sophisticated cerebral anatomical phantoms with multiple tissue and anthropomorphic structures may be constructed.

2.4 Vessel Enhancement

The enhancement or segmentation of vascular structures is particularly important for medical diagnosis, surgery planning, and surgical guidance. In fact, vessel segmentation is usually a prerequisite step for the accurate visualization of vascular features from complex vessel containing medical images.

Although automatic vessel segmentation methods are more widely used, manual vessel segmentation is still routine in many clinical settings despite being time-consuming, subjective and error-prone. With the amount of medical image data now being acquired and more commonly used in IGNS, the corresponding amount of processing and labour needed for manual segmentation can quickly add up in time and cost. On top of this, the use of manual segmentation can also inject interrater variability into the segmentation results. As such, *automated* vessel enhancement and segmentation tools are important not only because they improve operator efficiency for preparing vessel data, but they produce vessel segmentation results that are more consistent. This allows angiographic data to applied more routinely in surgical guidance and visualization, thus improving a surgeon's understanding of the

configuration of vessels around a lesion. In this manner, improved vessel enhancement and extraction can help improve surgical results, which altogether translates to better patient outcomes.

Vessel enhancement and segmentation is a challenging problem due to both the anatomy of the vessels and the characteristics of their acquisition modality. Healthy blood vessels vary greatly in their anatomical characteristics such as their cross-sectional size, length, curvature, and branching. The vessels themselves may be embedded in organs or different tissues that may also change their appearance when imaged. Furthermore, the dense vessel networks found in different organs can also differ greatly in their form and topology. These variations in forms are greatly increased should we consider vessels pathologies such as stenoses and aneurysms, or medical implants such as stents or embolizations. The type of imaging modality for blood vessels also contributes additional complexities to the creation of automated vessel enhancement and segmentation methods. Each medical imaging modality produces data of different effective resolutions and contrasts. They also contribute their own types of noise and unique imaging artifacts. These challenges have resulted in the development of a wide variety of vessel enhancement and segmentation image processing techniques for different and often dedicated applications.

A vessel segmentation algorithm may be be developed to process images of a target organ (e.g. liver, lung, brain) often in combination with a specific medical imaging modality (e.g. CTA, MRA, ultrasound). Vessel segmentation can in general be divided into three specific processing stages:

- **Preprocessing**: Processing the raw medical image data to enhance image structures, improve the image's quality, or reduce the effects of noise and image artefacts. Effective vascular image preprocessing can thus potentially improve the quality of any subsequently performed vessel structure extraction and postprocessing. Vessel enhancement methods belong in this category.
- **Extraction**: The optimization process in which the boundaries or the path of vessel structures in the raw or preprocessed image are explicitly located and delineated. This gives a defined boundary in image space between what are vessels and what are background parenchymal tissue. Commonly used extraction methods include voxel region growing [156, 20, 164], wave propagation [197, 119, 120], level-set front propagation [1, 220, 151], the popular active contours methods such as parametric snakes [160, 246, 267, 167] or curve evolution [144, 251, 63, 209, 265, 104], and centerline extraction methods [14, 62, 261].
- **Postprocessing**: The processing of extracted vessel structure information to refine and correct their results. Example of this are the vessel reconnection, hole-filling, or topology correcting methods. Alternatively, post-processing can also be use to further extract vessel structures to derive additional structural or morphological information on the vessel network. This includes extracting centerlines from extracted contours [177, 196, 227], detecting vessel boundaries and bifurcations from extracted centerlines [175, 80, 267, 167], detecting branch or vessel tree hierarchy [128], and reconnection disconnected vessel segments [268, 134].

A review of the entire field of vessel segmentation for preprocessing, extraction, and post processing is out of the the scope of this thesis. For further details on vessel extraction and postprocessing vessel segmentation algorithms, we direct the reader to the vessel extraction and segmentation review papers of Kirbas and Quek [121] and Lesage *et al.* [136]. In this section, we will provide a review of the work in the literature concerning solely the preprocessing algorithms used for vessel structure enhancement. They include methods based on first and second-order image derivatives, image intensity statistics, anisotropic diffusion, prior-knowledge image registration, and other detection models such as mathematical morphology and multidimensional filtering.

2.4.1 First Derivative Methods

Some of the first vessel feature filters were based on image first-derivatives. Koller *et al.* [124] proposed a general multiscale filter through the non-linear combination of first derivative Gaussian edge detectors to produce a feature detector that was insensitive to edges but sensitive to line image structures. Their feature detector was steerable and scalable over an image and could thus determine local image orientations and detect line features of different scales. By combining the maximum filter responses of the feature detectors over a set of orientation and varying the detector scales in that orientation, a line-structure enhanced image was produced. The author successfully applied the method on 2D natural images and extended it for use in 3D volumetric MRA images by incorporating vessel orientation information found by obtaining the principle vectors of the image Hessian.

Poli and Valli [192] proposed a real-time vessel enhancement method that used a set of line filters sensitive to different line orientations and thicknesses. The sets of filters were made by linearly combining spatially shifted Gaussian first-derivatives kernels of different widths that were then stretched "longitudinally" to be more directionally selective. These filters were note by the authors to be similar to the receptive fields of cells in the visual cortex and also filters designed by Zucker [273] for texture tangent field estimation. Outputs of each filter direction were then integrated together by finding their maximum intensity at each pixel to produce the resulting enhanced vessel image. The authors tested their methods and found that it could process images at a rate of 13 per second on a 300 MHz computer. As well, the enhanced images processed from real 2D coronary angiograms and synthetic phantom images that showed promising results.

2.4.2 Second Derivative Methods

A popular class of vessel feature filters are the Hessian-based filters. While some methods used solely the second derivative information for enhancement, others used it in combination with first derivative information for improved vessel enhancement at vessel lumen boundaries.

Although early vessel enhancement methods used the image Hessian to find the local principle orientation in the image [124], Aylward *et al.* [12] was the first to analyze the image Hessian to enhance the image intensity ridge for vessel segmentation at user specified scales. The ridges were found by comparison of the Hessian eigenvalues. A ridge exists at a 3D voxel with eigenvalues λ_i such that $\lambda_1 < \lambda_2 < 0 < \lambda_3$.

The diameter of the vessels at the detected image ridge could be found by convolution of the image with a Laplacian of Gaussian at a user estimated scale for a ridge point. By traversal along an image ridge from a user selected initial point, a vessel structure centered at the image ridge can be extracted. The authors tested the method on 3D MRA and CT bone data and found that it allowed vessels and bone structures to be quickly and successfully segmented by the user.

One of the first to describe a multiscale vessel feature filter that used second derivative Hessian eigenvalues extensively for vessel enhancement was Lorenz *et al.* [143]. In their filter, the image Hessian was decomposed to find the eigenvectors and eigenvalues at multiple filter scales optimized for vessel enhancement. The eigenvalues at the each scale were then analyzed by finding their ratios and combing them with the local image gradients to enhance vessel-like structures. They also showed that using the orientation information from the principle Hessian eigenvector, along with their detected vessel-like structures can be used to improve vessel skeletonization and surface meshing. The method enhanced the vessel lumen strongly on both 2D digital subtraction angiographic (DSA) images and 3D MRA images.

Frangi *et al.* [81] proposed a multiscale filter based solely on Hessian eigenvalue analysis greatly extending the eigenvalue ratio analysis of [143]. The analysis consists of 3 eigenvalue ratio terms repeated at each filter scale and then integrated to create the final filter vessel map. The method analyzes the eigenvalues at multiple scales

(s) through 3D vesselness filtering defined for dark-field images as:

$$V(s) = \begin{cases} 0 & \text{if } \lambda_2 > 0 \text{ or } \lambda_3 > 0 \\ (1 - \exp\big(-\frac{R_A^2}{2\alpha^2}\big)) \exp\big(-\frac{R_B^2}{2\beta^2}\big) (1 - \exp\big(-\frac{S^2}{2c^2}\big)) & \text{otherwise} \end{cases} \tag{2.1}$$

where $R_A = |\lambda_2|/|\lambda_3|$ in the first term assures that that the vessel cross-section is relatively circular and $R_B = |\lambda_1|/\sqrt{|\lambda_2\lambda_3|}$ in the second term assures that vessel is more elongated in one axis. These two first terms describe the geometry of a vessel segment. The last term with $S = \sqrt{\lambda_1^2 + \lambda_2^2 + \lambda_3^2}$ weighs the intensity of all the eigenvalues, making sure that only pixels with higher eigenvalues are enhanced ("structureness"). The method was tested on 2D DSA and 3D MRA images and showed the effective enhancement of different sized vessel structures. Sato *et al.* [216] developed another filter using different terms for Hessian eigenvalue analysis to enhance vessel-like structures. The formulation of the terms also suppresses non-vessel image features while being relatively robust to changes in vessel intensity. To do this, the authors made a thorough study of the effects of intensity and morphological changes along a vessel segment on the derived Hessian eigenvalues. The method also introduced a technique to combine filter outputs of each scale, by equalizing the results of each scale to the background noise, thus balancing noise suppression with vessel enhancement intensity.

Shikata *et al.* [225] used Hessian eigenvalues to first enhance the tubular vessel structures and then estimate the vessel centre as an initial step for processing. Their method then grew paths from seeds along the vessel centres using the eigenvalue corresponding to the principle vessel orientation eigenvector at each location as the

termination criterion. Spheres with sizes estimated from the image's gradient are then drawn onto the grown path to extract the vessel structure. The algorithm was applied to clinical CTA scans of five healthy human subjects and validated on manually identified vessel centerpoints. The results obtained were visually promising and were able to correctly label on average 98% of the manually identified vessel centerpoints.

Vessel enhancement methods can also be used to suppress or remove vessel structures from an image. Li *et al.* [140] described a vessel enhancement method to remove CT liver vasculature in order to enable improved identification and detection of liver nodules. The filters used for enhancement were tunable to selectively suppress tissue feature types according to their size and shape. Terms were developed using Hessian eigenvalues ratios for the sole enhancement of dot, line, and plane-like objects. The filters were tested on synthetic images and clinical 2D and 3D CT images and showed qualitative effectiveness in selectively enhancing specific shaped objects. The authors indicated that this may be useful in computer assisted diagnosis of tumours and other pathologies.

As with the work of Aylward *et al.* [12], certain methods used the second-derivative information to specifically enhance image ridges and vessel centerlines that can be used to further enhance vessel structures. Krissian *et al.* [127] proposed a multiscale filter using Hessian eigenvalues to enhance vessel center-ridges for use as initial vessel centerpoints in vessel extraction. The authors quantified the effects of filter scale and vessel sizes on filter responses and used them to create their cylindrical vessel detection model. Like [12], the authors used the information of the initial

vessel center-ridges and their principle direction. However they used the multiscale eigenvalues for vessel size detection, the image first-order derivatives to refine vessel boundaries and centers detection, and combined them together to develop an improved model for vessel enhancement. The technique was tested on 3D synthetic images, physical phantom images and clinical images, showing that the method was able to properly enhance closely space or highly curved vessels, vessel bifurcations, and low intensity vessels.

Staal *et al.* [235] presented a method for enhancing retinal angiographic images by using information from second order derivatives to enhance vessel image ridges for use as approximate vessel centerlines. The ridge points are grouped into convex sets according to the orientations of the image intensity ridge. Once grouped, the convex sets were then used to partition the image into convex regions, with the pixels closest in Euclidean distance to a convex set belonging to that set's region. Feature vectors are computed for each pixel in each convex region, which are then used to classify pixels as vessels or background features using a trained kNN-classifier. The method was tested on 40 manually labelled retinal angiographic images and was able to enhance the vessels with accuracy bordering that of a human observer.

2.4.3 Anisotropic Diffusion Methods

The challenge of extracting thin and lower contrast vessel structures while suppressing noise has been tackled by a different class of methods using anisotropic diffusion. Stemming from the diffusion scheme of Perona and Malik [186] and its reformulations [33, 7], the technique diffuses, or spreads the values of an image taking into consideration the boundaries of local image features. Through this process,

image noise can be average out while the contrast of image features or oriented structures could be preserved and enhanced. This led to the development of anisotropic diffusion methods specifically for regularization of medical images [86], with numerous subsequent applications to angiographic images for enhancement of vascular features [176, 163].

Meijering *et al.* [163] proposed an edge enhancing diffusion technique for the specific purpose of vascular feature enhancement, using the Perona and Malik diffusion scheme regularized by the method of Catte *et al.* [33]. Although the original method produces overall smoothing that appeared anisotropic, the core of the diffusion method was actually isotropic and dependant on the image intensity gradient to scale local diffusion [33]. To create their anisotropic diffusion method, they used the diffusion tensors of [255] and created a method that not only smooths in regions with low gradients, but also gives preference to smoothing along edges instead of over them. The method was tested on digital simulations and on physical phantoms and showed improved smoothing results over the previous methods while maintaining oriented structures.

Instead of using matrix-based diffusion, information from intensity gradient flux can also be analyzed and used for anisotropic diffusion vessel enhancement. Krissian [126] proposed a enhancement method based on decomposing the image gradient flux locally in an orthogonal basis, which allows image voxels with higher local intensity curvatures at specific orientation to be enhanced. Orientations with the smallest

image intensity curvatures undergo anisotropic diffusion to regularize vessel structures. The method was demonstrated on a liver CTA and shown to be successful at preserving thin, low-contrast and stenotic vessels.

Tankyevych *et al.* [242] proposed a different diffusion scheme relying on anisotropic mathematical morphological operators. They used the image Hessian eigenvalues to initially isolate linear vessel segments and then applied opening morphological operators with orientation variable structuring elements. These filters were guided by the orientation information derived from the Hessian eigenvectors, which allowed them to track, extend, and connect linear vessel segments. The method was tested on 2D neurite images and shown to connect and homogenize linear vessel segments.

Although not technically an anisotropic diffusion method, Orkisz *et al.* [176] described a conceptually similar anisotropic smoothing scheme. This method was based on detection of regional orientation using a discrete directional kernel similar to anisotropic Laplacian kernels. The direction filter with the highest response and homogeneity is chosen and the median value of the pixels under the kernel is used as the intensity. They tested their method on lower limb as well as abdominal artery MRA images and found that their anisotropic filtering method not only resulted in lower image noise, it also enhanced of vascular structures in the processed images.

Several anisotropic diffusion vessel enhancement methods were based on modifying Frangi's [81] multiscale vesselness measure to provide smoothing to the original method's geometrically based structure enhancement. Canero and Redeva [34] proposed the construction of diffusion tensors based on the crease enhancement diffusion method of Solé *et al.* [234] but reformulated it for Frangi's [81] multiscale Hessian

based vesselness measure. A pixel's participation in image vascular structures was determined via the thresholding, and its value was then smoothed based on a diffusion tensor constructed from the Hessian eigenvectors, eigenvalues and the scale of the convolution. The method was tested on 2D synthetic digital images with different noise levels or structure types, and on 2D X-ray angiographic images. The authors found that the diffusion scheme suppressed the image background while improving the image's vessel structure coherence.

Manniesing *et al.* [152] also proposed a multiscale diffusion-based vessel enhancement method that modifies Frangi's [81] vesselness measure by affixing a smoothing term to Frangi's vesselness measure. The method undergoes iterated rounds of diffusion that computes the images' vesselness while smoothing the result using tensors constructed from the Hessian eigenvectors and eigenvalues. The tensors are constructed such that they isotropically smooth non-vessel background structures while anisotropically smoothing vessel structures along their principle orientations. Vessel segments at bifurcations are smoothed into one another according to their respective diffusion tensions, resulting in no disjunctions. Their method was applied to low-dose 3D CTA and shown to preserve thin vessels and maintain the diameters of vessel structures of all scales.

More recently, Yuan et. al [269] proposed the use of local line integrals to average values along the principal axis of a vessel segment to provide smoothness to the measured vesselness map. An orientated line at a certain pixel which gives highest local orientation similarity with respect to curvature is used to integrate and average the Hessian eigenvalues of pixel along that line. Frangi's [81] vesselness measure was

then applied onto the average values to find the local vesselness. In addition, the authors evolved a curve to track the vessel segment's centre, which improve the line integration, resulting in improved smoothing. Vessel segments at bifurcations were treated as special cases which were detected and the Hessian integration line length was adjusted to reduce the intensity suppression at these junctions. When tested on 2D angiographic image databases and on 2D synthetic images, this curve directed smoothing reduces noise and preserves thin vessel structures.

2.4.4 Statistical Methods

Several groups have used image intensity statistics in order to highlight vessel regions and enhance vessel structures. Wilson and Noble [259] were one of the first to propose a statistical method for the probabilistic classification and hierarchical enhancement of vessels in angiographic images. The authors modelled the intensity distribution of each image tissue type using a Gaussian mixture model, and found the parameters for the model through expectation maximization (EM). By fitting the model to an image's intensity, each voxel can be statistically labelled as a vessel or a background class. The statistical labelling is then performed recursively on smaller sub-regions in the image to improve the model fitting process. The method was tested on 3D time-of-flight (TOF) MRA and was found to correctly classify vessels and estimate their sizes well enough for the needs of surgical intervention.

Hassouna *et al.* [96] described another statistical vessel enhancement method by modelling MRA vessel lumen intensities and background tissues using mixture models of Rayleigh and Gaussian distributions and then estimating the parameters

using EM. They showed that their proposed mixture model can represent the intensity distributions of vessel in the clinical images better than methods using purely Gaussian mixtures, and that it helped in vessel enhancement. As well, their proposed model initialization parameter estimation, based on histogram analysis, helped prevent parameter initialization dependent EM techniques from converging to any local maxima. The authors tested their algorithm on twenty 3D TOF MRA data sets and a geometric phantom and showed that it can accurately enhanced surgically and radiologically relevant vasculature in these images.

Gan *et al.* [85] proposed a 3D vessel enhancement algorithm based on 2D maximum intensity projections (MIP) of the original 3D image. The method uses a maximum *a priori* estimator on a mixed Gaussian models to identify voxels above certain intensity thresholds as vessel voxels and remove them from the processed image. This estimation process was repeated until the model showed that all vessel voxels have been identified. The MIP processing was repeated once for each axis and the combined information allows isolated misclassified voxels to be iteratively removed. The method was able to enhance major vascular structures in 3D rotational angiography and produced less false positives than maximum *a posteriori* based statistical methods.

Instead of only using statistical image intensity modelling for vessel enhancement, additional information can also be incorporated into for improved enhancement results. For instance, Chung *et al.* [42] combined statistical modelling with image coherence measurements to enhance vessels in phase-contrast MRA. The authors proposed a method to automatically select between different image-fitted mixture

models and found the optimal values to threshold foreground structures. A coherence map was then generated using local phase coherence and combined with the intensity mixture models to create a probabilistic framework for separating vessel structures, paranchymal tissues, and the background. The authors applied their technique on synthetic, phantom, and clinical images and found that it segments vessels of relatively low intensities and high SNR values with higher accuracy than statistical modelling methods without coherence information.

A different approach combined statistical vessel enhancement with anisotropic smoothing was described by Yang *et al.* [266]. This is done by first roughly clustering the image intensities into different tissue classes using k-nearest neighbour and then modelling the intensity of each cluster with a Gaussian distribution for use as probabilistic *a priori* knowledge. This information is introduction into Bayes' rule, which can then be use for maximum *a posteriori* estimation. The probabilistic maps from the estimation were then anisotropically smoothed in the direction of the inward normal vector of the local image maximum intensity curvature to produce a set of regularized tissue posterior probability maps. These smoothed maps can then be used for vessel extraction. The algorithm was tested on a 3D contrast-enhanced CT cardiac image and was found to successfully segment blood and the lumen of coronary arteries to help achieve more accurate clinical diagnoses.

Instead of creating statistical models based on global voxel intensity, Agam and Wu [3] and Agam *et al.* [2] instead created probabilistic shape models for detecting vessel features. Agam and Wu [3] proposed a probabilistic vessel enhancement filter based on analysis of structure tensor eigenvalues using a probabilistic model

that accounted for vessel bifurcations. Since the method was based on structure tensors constructed from image first-derivatives, the method was more robust to noise than second-derivatives based methods. Their probabilistic model had also higher degrees of freedom which allowed it to distinguish between non-vessel nodule structures ash vessel bifurcations. Similarly, Agam *et al.* [2] introduced a vessel tree enhancement and nodule detector using correlation-based enhancement filters and fuzzy shape representation. The correlation-based enhancement filters operate on first-order derivatives and the fuzzy shape representation was based on regulated morphological operations. Together, this made the method less sensitive to noise compared to Hessian based second-derivative methods and standard morphological operators, respectively. The probabilistic methods of both Agam and Wu [3] and Agam et al. [2] were tested on thoracic CT scans and found to properly distinguish between lung nodules and vessel bifurcations, thus allowing the selective enhancing or suppressing each type of structure as required.

2.4.5 Registration-based Methods

Vessels can also be segmented by registering a vessel image with another image that has been pre-labeled or associated with prior knowledge models. Passat *et al.* [179] proposed a registration-based probabilistic vessel enhancement method based on *a priori* knowledge of neurovascular anatomy. A cerebral vascular atlas was first created by extracting the vessel size information, non-linearly registering them to a reference image, and calculating a probability map of possible vessels at a location by the average of registered vessel images. Segmentation is performed by registering the reference image to a vessel image, eliminating the locations where vessels are

not likely found, and adding likely vessel points using the author's "hit-or-miss" morphological structuring element. The enhancement method performed well on enhancing vessel voxels in phase contrast MRA data and was shown to be robust to high-intensity imaging artifacts.

Isgum et. al [108] described an atlas-based heart and aorta vessel segmentation method that operated through registration of multiple manual atlases. The target image undergoing segmentation was registered to multiple atlases and their labels were propagated based to the target image based on their absolute intensity differences of the registered images. The labels were fused in a manner similar to label-fusion techniques, by weighting the pixel intensity differences between the target and atlas image. The authors also introduced an atlas selection method based on pattern recognition to speed up the segmentation process. The method was compared against single and average-shape atlas-based segmentation method and validated using heart and aortic images from thoracic CT scans. Results show that the method was more accurate than other atlas-based methods based on a single atlas, an average-shape atlas, or multi-atlas method with fusion by total average. The author noted that the results produced were very similar to those of an independent human observer.

Another registration-based vessel enhancement method involving alignment of prior knowledge models with the subject image was introduced by Biesdorf *et al.* [18]. This method provided patient specific aortic arch segmentation through non-rigid registration of an aorta parametric intensity model. A 3D parametric cylindrical aortic model was Gaussian blurred to match the intensity profile of aorta image features and then rigidly registered to a 3D CTA aorta image. The model was then

deformed through elastic non-rigid registration to improve fit of the model's intensities to that of the image and thus improving the segmentation result. This method combines the benefits of robust model-based segmentation with the accurate delineation of elastic registration, and can cope with different healthy and pathological vessel shapes. The method was validated on synthetic images, phantom data, and five clinical CTA images and found that the computation speed and segmentation accuracy of the approach is superior to pure model-based approaches that do not incorporate non-rigid registration refinement.

2.4.6 Other Methods

On top of vessel filters based on derivatives, vessel probability, diffusion, and prior-knowledge registration, techniques have also been developed, taking advantage of other detection models. Wilkinson and Westenberg [257] described a method using mathematical morphology filters with top-hat transforms to suppress noise and non-vessel features in CT angiographic images. They proposed two filters which either performed size distribution morphological openings of a "filamentous" vessel feature at different scales or applied scale independent shape criteria filters at different image intensity thresholds. Zana and Klein [270] also proposed the use of mathematical morphological operators supplemented with the analysis of image curvature to remove non-vessel features from angiographic images. The authors used linear opening operators to detect vessel segments, and used structure connectivity with image curvature analysis to improve image contrast to finally highlight vessel structures. The method was tested on 2D retinal angiographic data sets and found to enhance the vessel structures without suppressing vessels at junctions and bifurcations.

A multidimensional approach for vessel filtering in the Fourier domain was proposed by Westin *et al.* [256] as a feasible approach to reduce a angiographic image noise while improving vessel enhancement. The direction of local image features was first estimated using quadrature filters. With the direction information, the method performed locally adaptive highpass or lowpass filtering to eliminate high frequency noise while preserving thin vessel-like structures. The implemented Fourier domain filters greatly simplified filter rescaling, which were linearly combined to extract different image features. The method was validated on synthetic images and clinical 3D phase-contrast MRA cerebral data and 2D TOF renal MRA data, which showed that the method was effective at suppressing noise while preserving and enhancing thin vessels.

Local image thresholding can also be used to enhance vessel structures from the background. Jiang and Mojon [113] proposed a multiple adaptive local image thresholding method for retinal angiography vessel enhancement. The method performed adaptive local thresholding to a test image and then accepted or rejected the thresholds through an automatic verification procedure. A raw vessel image is thresholded at various intensities and the pixels in each binary threshold image were verified to be part of a curvilinear structure using a contrast and vessel thinness criteria. Pixels filtered at each threshold were recombined to produce an enhanced vessel map. The authors validated their method on 20 retinal angiographic images and reported that their method had high specificity and was significantly better than global thresholding methods. The method is also shown to be general enough to be useful for a wide range of other image feature enhancement applications.

Law and Chung [132] introduced a vessel filter based on image gradient flux on a vessel segment. The flux entering a local sphere was determined and the orientation with the minimal flux was computed, producing a set of eigenvectors and eigenvalues. The eigenvalues were then analyzed to produce a measure for vessel-like elongated structures. The method analyzed only the local flux on a local sphere surface and thus the results were less sensitive to corruption by the presence of adjacent vessel structures. The method was validated on closely spaced synthetic vessel images and on phase-contrast MRA images, which demonstrated that it was robust to image noise, extracted vessels of lower intensity, and could enhance closely located vessel structures without degradation of enhancement compared to Hessian-based methods.

Truc et. al [247] proposed the use of directional filter banks to enhance 2D vessel structures. Filters of different orientations were applied to the raw image, then each filter output was then corrected for non-uniformity in image intensity. The intensity corrected images then undergo multiscale Hessian eigenvalue analysis to enhance vessel like structures. The enhanced directional images are then recombined by summing to obtain the final filtered vessel map. The authors tested the method on synthetic images and clinical 2D retinal and cardiac angiographic data, which showed that the directional image filters avoids suppression of vessels bifurcations and thin vessel structures which allow for the enhancement of more complete vessel trees. The methods is also quantitatively less sensitive to image noise when compared to Hessian-based approaches.

2.4.7 Challenges

Most vessel enhancement and segmentation algorithms are adept at isolating higher contrast vessel structures. However, the primary challenge of vessel segmentation still lies with the proper enhancement of thinner or lower contrast vessel structures in moderately noisy images.

Image first derivatives method are able to accurately detect and enhance large vessel structures with fewer model shape constraints and less noise sensitivity than second derivative methods. However, they are sensitive to intensity edges, and some methods require filter steering or special model constraints to effectively segment thinner vessels. Second derivative vessel enhancement methods are popular and have been effectively used for multiscale vessel enhancement but are more sensitive to noise. As well, due to their filter models, many of them suppress vessel bifurcations unless this is compensated by information from other methods. Statistical vessel enhancement methods can help effectively highlight regions where vessels exist for further segmentation processing, but they may not be as effective for enhancing long segments of thin vessels. This is similar for prior-knowledge registration-based enhancement methods, which can be applied to robustly enhance large spatially stable vessel structure but are less effective at enhancing smaller vessels at variable locations. Finally, the use of anisotropic diffusion methods can greatly reduce noise and help regularize vascular structures for enhancement. But balancing diffusion image smoothing with proper retention of details, such as tortuosity in smaller vessels, is not trivial.

Vessel enhancement can be improved by being able to better determine whether a pixel or voxel has local features that correspond to vessel structures. However, not all vessel structures can be effectively detected by using only local features, such as low contrast-to-noise or thin vessels. By taking into account information from a larger image region surrounding a point, beyond that of its local support, a developed method can better determine if the point is indeed part of a greater vessel structure.

2.5 Conclusion of Review

The use of angiographic data in IGNS can be greatly enhanced through improved vessel-based image registration and vessel image enhancement to help visualize blood vessel structures. As well, imaging phantoms should be used to validate such segmentation and registration methods.

In the following chapters, we explore methods for vessel-based registration, construction of physical phantoms, and vessel enhancement. We saw the need for a effective intraoperative vessel registration method and recognized the benefits of hybrid vessel image based enhancement. As such we extended the feature-based vessel registration methods of Reinertsen *et al.* [202, 201] by reducing the extent of feature extraction to retain more image intensity information, thus preventing the removal of image information needed for registration and improving the rate of registration success. To improve our image registration validation, and more generally, medical image processing validation, we extended the phantom development work of Surry *et al.* [240] and Reinertsen *et al.*[199] to develop an anthropomorphic multimodal PVAc based brain phantom that contains multiple anatomical features as well as inflatable

catheters and fiducials to allow precise control of non-linear deformations and validation of distortion correction. As well, we found during our registration work that there needs to be an improved vessel enhancement method. As such, we developed a vessel enhancement method that improves upon Frangi's second derivative-based vessel enhancement filter [81] by incorporating local eigenvalue analysis with regional structure information through non-local means weightmaps analysis as proposed by Buades *et al.* [26].

CHAPTER 3
Multimodal Volumetric Vessel-based Registration

Forward

In this chapter we present a novel non-linear hybrid vessel registration technique that combines aspects of both feature-based and intensity-based vessel registration methods for aligning magnetic resonance (MR) angiographic images to intraoperative Doppler ultrasound (US) angiographic images. As mentioned in Chapter 2, the correct merging of medical images used for neurosurgical guidance is of great importance for precise surgical targeting in IGNS. To allow for greater accuracy and robustness in registration, our hybrid technique retains as much of the original vessel intensity information as possible, with limited filtering to remove non-vessel background paranchyma. This non-linear registration technique is practical for intraoperative image alignment, using US images directly acquired on the patient's dura in the surgical region of interest. Our registration technique corrects for skin-surface registration inaccuracies and for brain-shift which occurs after craniotomy.

This chapter has been published in the *International Journal of Computer Assisted Radiology and Surgery* as [39]:

- S.J-S. Chen, I. Reinertsen, P.Coupé, C. Yan, L. Mercier, D. Del Maestro, and D. L. Collins. Validation of a hybrid Doppler ultrasound vessel-based registration algorithm for neurosurgery. *International Journal of Computer Assisted Radiology and Surgery*, 7(5):667–685, 2012.

Manuscript: Validation of a Hybrid Doppler Ultrasound Vessel-based Registration Algorithm for Neurosurgery

Sean Jy-Shyang Chen [1], Ingerid Reinertsen [2], Pierrick Coupé [3], Charles X. B. Yan [1], Laurence Mercier [1], D. Rolando Del Maestro [4], D. Louis Collins [1]

[1] McConnell Brain Imaging Centre, Montreal Neurological Institute, McGill University, Montreal, Canada
[2] SINTEF Health Research and National Centre for 3D Ultrasound in Surgery, St. Olav University Hospital, Trondheim, Norway
[3] CNRS, UMR 5800, Université Bordeaux, 33405 Talence Cedex, France
[4] Department of Neurology & Neurosurgery, Montreal Neurological Institute, McGill University, Montreal, Canada

Abstract

We describe and validate a novel hybrid non-linear vessel registration algorithm for intraoperative updating of preoperative magnetic resonance (MR) images using Doppler ultrasound (US) images acquired on the dura for the correction of brain-shift and registration inaccuracies. We also introduce an US vessel appearance simulator that generates vessel images similar in appearance to that acquired with US from MR angiography data.

Our registration uses the minimum amount of preprocessing to extract vessels from the raw volumetric images. This prevents the removal of important registration information and minimizes the introduction of artifacts that may affect robustness, while reducing the amount of extraneous information in the image to be processed, thus improving the convergence speed of the algorithm. We then completed 3 rounds of validation for our vessel registration method for robustness and accuracy using (i)a large number of synthetic trials generated with our US vessel simulator, (ii)US images

acquired from a real physical phantom made from polyvinyl alcohol cryogel (PVAc), and (iii)real clinical data gathered intraoperatively from 3 patients.

Resulting target registration errors (TRE) of less than 2.5mm are achieved in more than 90% of the synthetic trials when the initial TREs are less than 20mm. TREs of less than 2mm were achieved when the technique was applied to the physical phantom, and TREs of less than 3mm were achieved on clinical data. These test trials show that the proposed algorithm is not only accurate but also highly robust to noise and missing vessel segments when working with US images acquired in real-world conditions.

3.1 Introduction

Modern neurosurgery relies heavily on computer assistance and image guidance to provide topological and locational information to surgeons, enabling them to accurately navigate within the patient's brain. Known as image guided neurosurgery (IGNS), these techniques typically use the preoperative image of the patient's head acquired through magnetic resonance imaging (MRI) for surgical planning and navigation. Significant errors may be introduced into surgical navigation from image misregistration or through intraoperative deformation of brain tissues in neurosurgery, also known as brain-shift. Displacements from brain-shift can vary greatly between 5–50mm on the cortical surface [27, 66, 98, 116, 158, 166, 171, 203, 202, 207]. However, even prior to dural opening, displacements caused by brain-shift can nevertheless be quite significant. Hill *et al.* (1998) [98] have shown that even with the dura intact, the magnitude of brain-shifts observed was as large as 3.4 mm pushing outwards and 8.1 mm collapsing inwards.

These tissue displacements, both *before* and after dural opening, are quite significant and enough to render guidance using the preoperative magnetic resonance (MR) image useless for surgical use, even after accurate initial patient to image registration. In order to compensate for such displacements in the soft tissue, the preoperative MR image can be corrected by registering it to an intraoperative image, which could be acquired using either intraoperative computed tomography (CT) [94], intraoperative MR [97, 174, 208], or intraoperative ultrasound (US) imaging [130, 202].

US is a good candidate for intraoperative imaging. However, images acquired using US may be difficult to interpret by untrained users. This is due in part to its relatively small imaging field-of-view, its non-standard anatomical views, speckling in its acquired images, and the need for a craniotomy in order to do intraoperative brain imaging. Nevertheless, US imaging has many advantages that overcome these shortcomings. For instance, US imagers have the benefit of being significantly less expensive, capable of real-time imaging, and more portable than either MR and CT imaging devices. As well, US imaging gives good resolution and contrast in soft tissues without the need to compromise surgical ergonomics or exposing the patient to ionizing radiation when compared to intraoperative MR and CT, respectively. Intraoperative US images can be used effectively to correct and update the preoperative MR images to the intraoperative state of the imaged tissues.

The challenge of registering images between US and MR modalities is that they have different image contrasts, noise patterns, and artifacts. This is due to the fact that the two imaging modalities are acquired using very different physical principles, with MR images depending on proton spin interaction and US images depending on

the material's acoustic properties. Two types of strategies are used in the literature to overcome the challenge of registering the images:

1. **Feature-based:** Salient anatomical features that can be imaged on both MR and US such as sulci [51], tumour outlines [138], or blood vessels [114, 130, 172, 181, 201] are used as alignment cues. These anatomical features are extracted and parameterized prior to their use in registration.
2. **Intensity-based:** This strategy typically employs image processing methods to relate the intensities of MR to US. For instance, gradient information in the MR image [208] may be used directly for registration, or the preoperative MR image may be segmented and processed to generate a set of "pseudo-ultrasound" images, which allows for better image correspondence and registration [8]. Mutual information could also be used to relate the intensities found in MR and US [110].

Blood vessels are important and useful features for the registration of deforming soft tissues due to several of their properties. First, vessels are easily identifiable and also usually well distributed in most surgical regions-of-interest (ROI). Second, many image processing methods exist to extract vessels from the acquired images. For instance, the moving blood in a blood vessel is easily imaged using Doppler US and can be implicitly segmented from the image background based on colour saturation alone. As well, vasculature from different types of MR angiography can be extracted preoperatively using segmentation algorithms such as that of Descoteaux et al. [64] and Frangi [81]. Finally, the vessel's unique branching and stable relative paths and positions to surrounding tissues allow for high specificity in registration. Therefore

as vessels move and change shape with deforming tissues undergoing brain-shift, the correction of these vessel movements enable the detection and correction of the corresponding tissue deformations.

To date, blood vessels have been successfully used for linear and non-linear registration of deforming soft tissues such as the cerebral cortex [172, 201] and the liver [130]. From previous work in our lab, brain shift compensation using vascular images from Doppler US and MR was characterized and shown to be highly accurate [201].

Purely feature-based registration algorithms are fast and accurate techniques that typically rely on image preprocessing to parameterize and reduce the complexity in the raw data. For vessel registration, this preprocessing is typically done through skeletonization, which reduces and parameterizes the vessel image into a set of vessel centerpoints. This process dramatically reduces computation time for registration since the amount of data that needs to be processed is often greatly reduced.

However, such methods can remove important information for registration, such as vessel lumen diameter or voxel intensity differences in the vessels images themselves. As well, thin, low contrast vessels and important vascular features such as branching and continuity can be eliminated altogether. Removal of this information introduces ambiguities that allows skeletonized branches of thick vessels to be incorrectly matched with thin vessels. Likewise, centerpoint fragments from different vessels can be incorrectly matched to a single vessel. As well, the extracted centerpoints of densely situated vessels can be reduced to featureless point clouds, making purely iterative closest point (ICP) algorithms [17] fail and rendering the registration

process impossible. For these reasons, purely feature-based registration can produce poor results on clinical data.

Indeed our previous experience using ICP-based techniques yielded good results using vessel traces that were relatively sparse [202], with distances between the vascular branches being greater than the magnitude of misregistration. However our recent experience with more complex anatomies containing many more blood vessels resulted in failed registrations.

Intensity-based registration methods are very accurate and quite robust to noise due to the amount of information available for use in alignment. As such, they are widely used for atlas, inter-subject, and various inter-modality registration tasks. Although more sophisticated intensity-based methods may be developed to improve processing time, intensity-based registration methods capable of correcting free-formed non-linear deformations required to properly register cerebral vasculature are quite computationally intensive and can take several minutes for images of modest size. For this reason, their use is limited to offline registration tasks since they are not suitable for intraoperative registration, which should ideally complete in at most 2-3 minutes during the time needed to prepare for tissue dissection.

These issues inherent to feature or intensity-based registration methods, necessitate the investigation and creation of a robust vessel registration method capable of overcoming the reliance on extensive preprocessing to allow for the registration of MR and US vessels with a high degree of accuracy in clinically acceptable time.

3.1.1 Motivation for Hybrid Registration

In this paper, we describe an algorithm for a hybrid feature and intensity-based non-linear registration of MR to US images through cerebral blood vessels using ANIMAL [47]. Previous non-linear feature-based vessel registration algorithms by Reinertsen *et al.* [201] and Lange *et al.* [130] preprocess their acquired images by segmenting the vessels and skeletonizing them to a set of discrete vessel centerpoints for registration. In contrast, our registration method attempts to eliminate the background by extracting only the vessel information while at the same time minimizing other forms of preprocessing to retain as much of the original vessel information as possible. To this extent, we use the whole volumetric vessels from the angiographic intensity images instead of relying on discrete points or lines produced through skeletonization of vessel data. In the following sections, we present our hybrid non-linear volumetric registration technique developed for the registration of US vessels acquired on the dura with MR vessels. Our goal for hybrid registration was to be able to automatically and robustly correct tissue displacements up to 20mm; a threshold that is more than twice the maximum recorded brain-shift tissue displacement of 8.1mm prior to dura opening[98].

3.1.2 Validation data types

Our registration method was then validated using three types of data with increasing realism:

Synthetic data generated from a digital phantom: Multiple synthetic US data sets were generated numerically from a clinical MR image. This enables us to evaluate the behaviour under controlled conditions where the ground truth is

known. However, the simulated data are not completely realistic and do not account for all possible imaging situations.

Real data acquired from a physical phantom: Real MRI and US data were acquired from a PVA phantom. This set of experiments permits evaluation of the algorithm with an object having a known gold standard, which produces images that are more realistic. However, the spatial distribution of the image signal is quite simplistic and does not accurately replicate data gathered in clinical scenarios.

Real clinical data acquired from 3 patients: Real preoperative MRI and intraoperative US data were acquired from 3 patients. This is the most realistic set of data and represents real surgery and clinical imaging. However the image registration results are difficult to evaluate since the ground truth is not known exactly.

3.1.3 Overview

We will describe in detail our hybrid registration algorithm in Section 3.2. We will then describe the tool we created and images we acquired to validate the robustness and accuracy of our registration algorithm, including the digital phantom (Section 3.3.1), the physical PVA-based phantom (Section 3.3.2), and clinical data from 3 patients (Section 3.3.3). The methodology for validating our registration algorithm is detailed in Section 3.3.5 followed by the result of the validation in Section 3.4. We then conclude with a discussion of our test results and future work in Section 3.5.

3.2 Hybrid Registration

Our hybrid registration method takes the raw MR and US clinical images and preprocesses them to extract vascular features while retaining the intensities of the vessels in volumetric form. This combination of intensity and feature-based cues are used for hybrid registration. The source image for registration consists of a 3D contrast enhanced MR vascular imaging processed with Frangi's vesselness filtering[81], while the target image consists of an intraoperatively acquired and reconstructed 3D Doppler US volume with the volumetric vessels extracted from the background tissues by using a colour saturation threshold. Detailed descriptions of the preprocessing done to the target and source images can be found in Sections 3.2.1.

Using the minimally processed vessel data, registration proceeds in two phases, with multiscale linear registration prior to non-linear registration. We noticed that although a large amount of registration error can be corrected with rigid-body transformations, the 6 degrees of freedom of the transform do not allow for an adequate correction of all the non-rigid displacements observed between the preoperative and intraoperative images. It is for this reason that we register the images using full affine transformations after an initial round of rigid- body registration for a first alignment, and then subsequently using non-linear transformations to correct the remaining brain-shift not captured by the affine linear transformation.

3.2.1 Preprocessing

The first step in our registration method is to preprocess our source and target images to extract their vasculature. Our source images were T1 weighted Gadolinium MR images that were processed using Frangi's vesselness method [81], which

effectively enhances tube and vessel-like structures in the image. The parameters used for the filtering are α, β and γ at 0.5, 0.5, and $0.5 \times max(HessianNorm)$ and five filter scales with values 0.4, 0.74, 1.1, 1.64, and 2.5mm.

Our target images were 2D power Doppler US images, which were fused with the raw B-mode US images. The latter were filtered by removing all pixels under a colour saturation threshold. The filtered 2D images were then reconstructed in a 3D volume using the tracking information contained in each image. This was done by nearest-neighbour regridding of each pixel in the ultrasound image slices to a 3D volume with the same resolution as the MR image in a similar fashion as that of [224]. Although other interpolation methods could have been used rather than the basic nearest-neighbour regridding method, we found that the other methods increased the 3D reconstruction time and did not perceptibly improve registration accuracy. A thorough review of 2D ultrasound image reconstruction techniques and their considerations can be found in [233].

3.2.2 Linear Registration Phase

The linear registration algorithm takes as input the aforementioned source and target intensity volumes which have been preprocessed for vessel features, then blurs them with a Gaussian kernel prior to each round of linear registration, using a smaller kernel for each subsequent round. We used the reconstructed US vessel volume as the registration target image and the MR vessel volume as the source image.

The starting estimates for registration depend on the method used for data acquisition. For our clinical cases (Section 3.3.3), the starting estimates are based on the transforms acquired from the facial skin landmark registration performed by a

surgeon. In the case of the physical phantom data (Section 3.3.2), the initial registration is done by point-based registration on the container of the physical phantom. In any case, the transforms puts the acquired US images into the same coordinate system as the MR image and provides the initial position for registration.

Table 3–1: Parameters used in multiscale linear registration (Top) and multiscale non-linear registration with ANIMAL (Bottom)

Round	Blur FWHM	Sampling grid	Crop margin	Transform
1st	3.3mm	2.5mm	50mm	Rigid-body
2nd	2.2mm	1.8mm	16mm	Affine w/ Isotropic Shear
3rd	1.5mm	1mm	10mm	Affine w/ Anisotropic Shear

Round	Lattice Diameter	Sampling grid	Rigidity
1st	15mm	5mm	0.9
2nd	10mm	2.5mm	0.8

Our linear registration is optimized using a downhill simplex algorithm [173] with cross-correlation as the objective function. We found that it performed effectively and quickly for registering our images of similar image contrast: both processed MR and US images have bright vessels on dark backgrounds. Although other objective functions such as mutual information may be used, we found in our preliminary tests that these methods were significantly slower and did not perform better than cross-correlation on our pre-processed vessel images. In fact, observations from our preliminary test are in line with that of [190], who suggested that registration with mutual information does not perform well in images with (1) thin structures such as the vessels in retinal images or (2) for cross-modality registration of MR to US images.

We performed a total of three rounds of optimization with sequentially smaller blurring kernels and sampling grids with successively refined linear transforms. Due

to the size difference between the US target and the MR source volume, cropping was automatically performed on the MR volume around the location of the US target to improve and speed up the calculation of registration transforms. Cropping for the first round of registration is set to 50mm, since this is the largest value of brain shift recorded in the literature. Parameters defining the full-width-half-max (FWHM) of the blur (where the FWHM relates to standard deviation by $\sigma = \frac{FWHM}{2\sqrt{2\ln 2}}$)[135], the sampling grid used, the crop margin, and the type of linear transform used in each round are described in more detail in Table 3–1.

3.2.3 Non-Linear Registration Phase

Following the linear registration, which provides a robust global alignment, we used the ANIMAL registration algorithm [47] to compute a set of non-linear transformations that corrects for any local vessel deformations that cannot be accounted for by the linear transformations. ANIMAL hierarchically estimates 3D vector field at different scales, mapping deformations progressively from larger to smaller scales and produces a globally non-linear deformation field with point-to-point correspondence between the two volumes.

The affine linear registration transforms recovered from the previous linear registration phase are applied to the preprocessed volumetric intensity source image, which is then used as the source image for this non-linear registration phase of our hybrid registration method. We performed two rounds non-linear registration, once at lower resolution, and once at higher resolution using ANIMAL with cross-correlation objective function, and relatively high stiffness to maintain smoothness in the deformation (See Table 3–1). The resulting transformation is applied in each

round of non-linear registration only if the final value of the objective function is reduced from the starting value.

Through the iterations of non-linear registration, we are able to attain correspondence between the US and the MR vessel images based on their grey scale voxel values. Even though the vessels are not sparse, there exists a significant amount of tissue in between each vessel where the ANIMAL algorithm must interpolate or extrapolate the deformations. This is due to the fact that the algorithm performs registration and regularizes using only the non-zero vessel voxels of the images, and ignores the zero-valued voxels where the non-vascular tissues have been removed. To address the limits of the local elastic regularization used in ANIMAL and to ensure a continuous smooth deformation throughout the tissue, we apply the thin-plate spline (TPS) transform [68] on points extracted from the aligned US and MR vessels to regularize the transformation over the entire image.

One thousand points are randomly sampled from overlaps of the vessels from the two non-linearly registered volumes and inversely transformed using the deformations recovered by ANIMAL. This produces 1000 pairs of homologous points, which are then used as the control points to define the displacements on an interpolating TPS.

3.3 Validation Methods

3.3.1 Digital Phantom

As part of the work to validate our hybrid registration algorithm, we developed a non physics-based digital phantom to synthesize images that simulate the appearance of Doppler US vessel images acquired from a brain distorted by brain shift. Qualitative visual observations were made between the vessels acquired using power

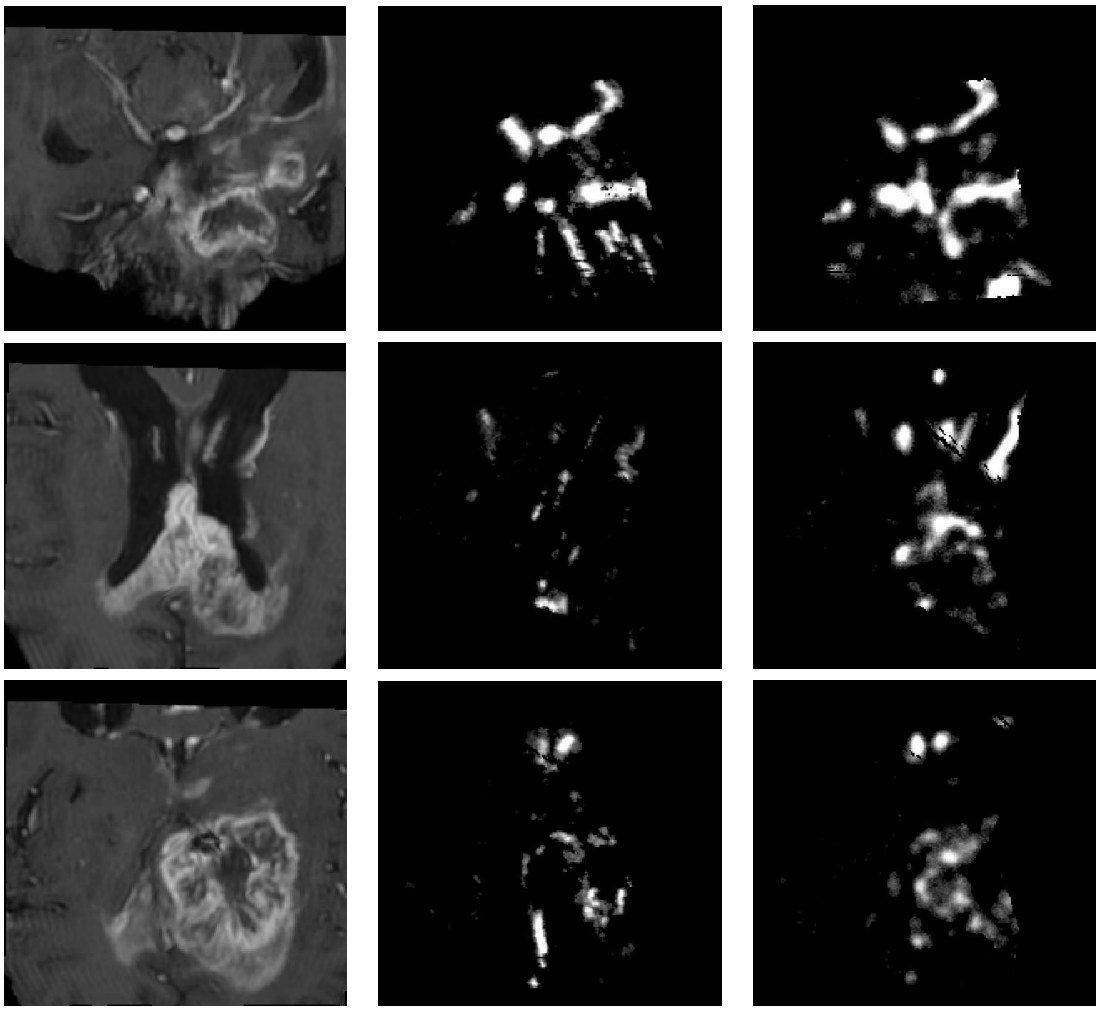

Figure 3–1: Three different cross-section views of the actual T1 Gado-enhanced MR image (MR image), the actual ultrasound volume (Actual US), and the simulated ultrasound volume (Simulated US) imaged in the same brain region.

Doppler US and MR imaging to enable and successfully imitate real power Doppler US images from MR vessel data. We found that the US vessels in comparison to MR vessels tend to be:

1. **Thick:** This is likely due to the fact that the US operator increases signal gain when acquiring the Doppler US image. This is done to allow smaller and more distant vessels to be captured in the image.
2. **Uneven:** The surfaces of the acquired US vessels are uneven due, in part, to speckling in US images and artifacts arising from flash artifacts caused by sudden probe movements.
3. **Noisy and containing artifacts:** Both noise and US image artifacts can be due to the random scattering and reflection of US pulses in the different tissue being imaged, as well as the noise introduced by the electronics of the US imaging equipment.
4. **Presence:** Some vessels are dimmer or entirely not present in volumes of one modality versus the other (See Fig. 3–1). This could be due to imaging artifacts such as occlusion, shadowing, and the angle of the US probe in respect to the imaged blood flow.

Our digital phantom simulates the appearance of a Doppler US vessel image by taking an MR vessel image as input. The workflow of the digital phantom is shown in Figure 3–2. The first step to producing the synthetic US vessel involves extracting and processing an MR angiographic image to act as the ground truth image. The second step is to generate a set of random linear and non-linear transforms to act as the registration ground truth and then applying the transform to an MR vessel

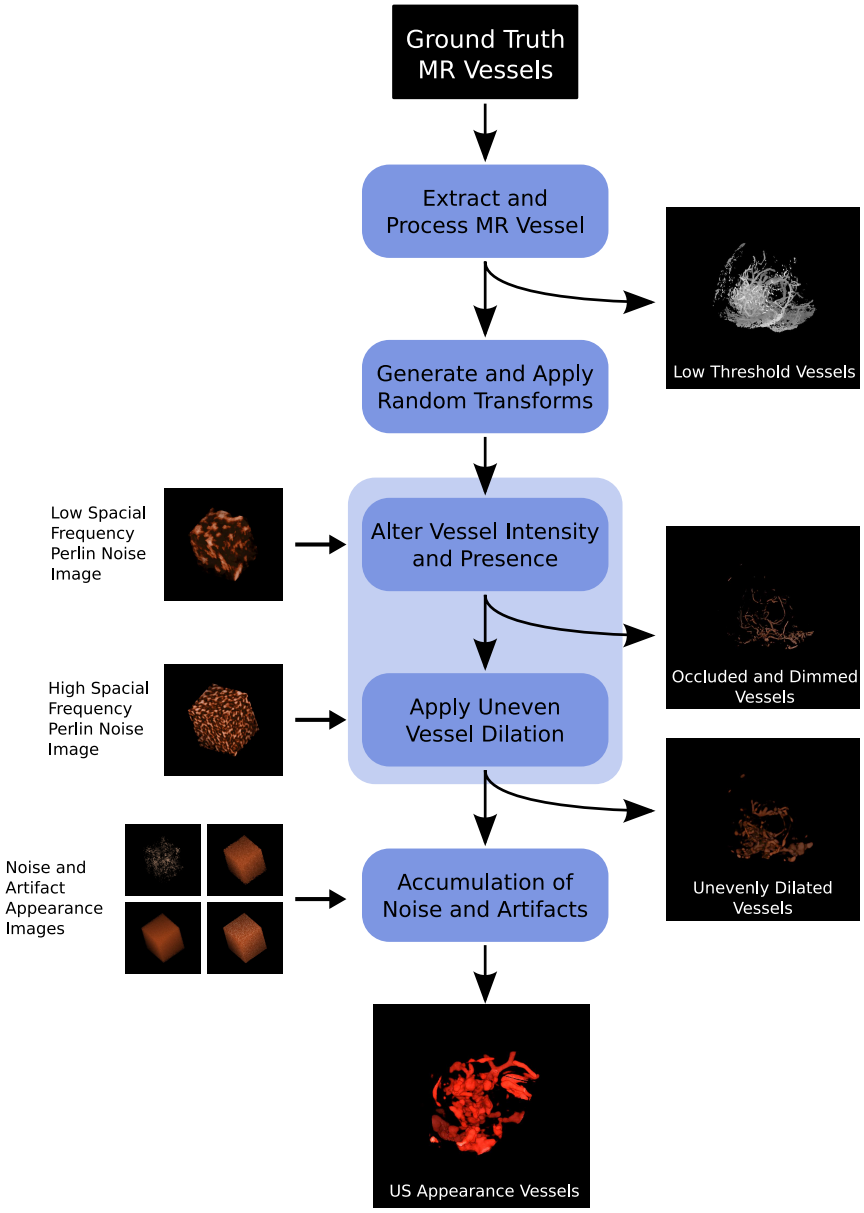

Figure 3–2: Workflow of the Digital Phantom showing each step of the Doppler US appearance simulation process. Images used and outputted in each processing step are also shown.

image. The third step involves altering the transformed MR vessel image to exhibit the observed characteristic appearance of the US vessels listed above. Finally, noise and speckling is added, and the simulated US volume is masked into the shape of an US sweep. These steps are explained in detail below.

To show that the simulated US vessel volume behaves similarly to a real US vessel volume in MR vessel registration, we also compared the similarity of the cross-correlation objective function curves to each other.

The first step in creating the simulated US vessels involves extracting the vessel from a T1 weighted Gadolinium MR image in the manner described in Section 3.2.1. The extracted MR vessel image is then thresholded at a low intensity to capture anything that may be a vessel and then cropped down to a ROI.

Random Transformations

Parameters for the linear transforms are chosen randomly within translations from -30 to 30mm, rotations from -5 to 5 degrees, scalings from 0.9 to 1.1, and shears from 0.9 to 1.1, with the fixed transformation point located in the center of the ROI bounding box. The non-linear transforms are generated using a TPS since this method produces realistic deformations that are smooth and regularized. Nine pairs of control points are used to define the TPS transform, with the two points of each pair randomly located in relation to each other at distances between 0–5mm. The first 8 point pairs are located on the corners of the bounding box around the ROI that has been scaled down by 50% to be inside the ROI. The last point pair is positioned in the center of the ROI bounding box (See Fig. 3–3). The rationale for this placement scheme is to localize the control points of the thin-plate spline in the center of the

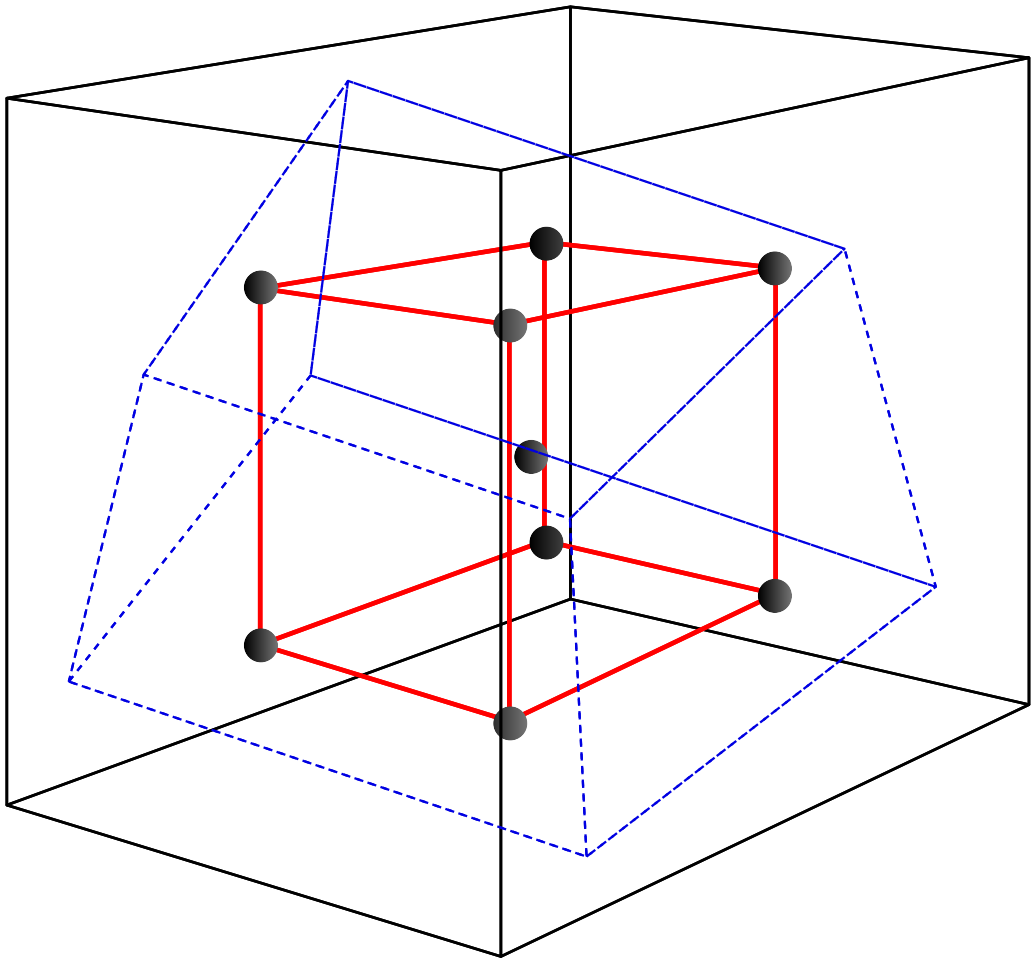

Figure 3–3: The placement of TPS control point pairs in relation to a region-of-interest (blue dashed box) for the creation of non-linear distortion. Eight control point pairs (gray) are located at the corners of the 50% scaled (red box) version of the bounding box (black box) surrounding the region of interest. The ninth point pair (gray) is positioned in the center of the bounding box.

ROI where the anatomical structures are located, thereby increasing the local non-linear deformations there. These sets of linear and non-linear transformations were used as the gold-standards for validating our registration method, and also applied to the processed MR vessel image to simulate tissue displacement from brain shift.

Simulation of Characteristics

Once the MR vessels have been deformed using the set of random transforms, they are used to simulate the appearance of Doppler images. The simulation occurs in two steps. First, the thick uneven surface and variable presence of the US vessels are simulated through the extensive use of Perlin noise [185]. Afterwards noise and speckle are added onto the simulated vessels.

Perlin noise is a procedural texturing method commonly used in computer graphics to generate many types of continuously varying pseudo-random textures with specific spatial frequencies. Random gradients are first defined at regularly spaced intervals in a 3D lattice. These gradients are used to determine the intensity of the field between the nodes of lattice through linear or cubic interpolation. This simple technique allows us to generate random appearing textures of different scales and spatial frequencies that can easily be used as parameters for varying the appearance of generated US vessels. A more detailed explanation of Perlin noise and the technique for generating it can be obtained in [185].

We used the intensity values of a Perlin noise texture with low spatial frequency as the parameter for determining whether the vessel is present in the image (vessel presence) by varying the contrast of a vessel to the background. The noise texture has a value between 0 and 1, which makes the vessel completely invisible and fully

visible, respectively. This roughly simulates artifacts from shadowing or from angle dependant modulation of the US signal. Although power Doppler US (signal power) is not as sensitive to probe angle as colour Doppler US (blood flow rate) the probe angle to a vessel may nevertheless alter the intensity of the power signal.

Perlin noise of high spatial frequency is used to determine the radius of a particular voxel's dilation on a visible vessel. The dilation is performed using a 3D isotropic Gaussian point spread function with a FWHM of between 3–5mm. This higher spatial frequency Perlin noise, which has a value between 0 and 1, is used to determine extent of the vessel dilation. The value of 0 indicates that the voxel will be dilated to 3mm and 1 indicates that the voxel will be dilated to 5mm. The combined uneven dilation of the original vessels produced a set of resulting vessels that are thick and bumpy. When the resulting dilated vessel volume is thresholded and windowed for intensity, a set of disjoint vessels with uneven surfaces are created, which simulates appearance-wise the increased gain of the power Doppler US imaged vessels and any amplified noise.

Accumulating Noise and Speckling

Various types of artifacts and noise commonly seen in US images and volumes are applied to the generated vessel volume as the final step to simulate the US vessel volume. Speckle artifacts generated via the methods of Pizurica *et al.* [189] and grainy Perlin noise are multiplied to the expanded vessels. Gaussian noise and high intensity voxels from Perlin noise of high frequency are added to the vessel volume. The volume is then masked with a mask generated from the coordinates and orientation of a real US sweep to produce a wedge shape volume similar to a

reconstructed US vessel volume. The resulting simulated US vessels qualitatively resemble the real US vessels in their thickness, uneven surfaces, noise, artifacts, and their variable presence (see Fig. 3–1).

Behavior of Simulated Vessels in Registration

To ensure that the simulated US vessels from our digital phantom performed similarly to real Doppler US reconstructed vessels in registration, we measured their cross-correlation values through translations, rotations, and scaling. The simulated US vessels and their corresponding real US vessels, were all registered and aligned to the MR angiography data. The gold-standard transform for aligning the real US image to the MR image was found by first calculating the affine linear transform between manually picked homologous anatomical landmarks between the US and MR image in the manner described in Section 3.3.3.

All the data sets were blurred with Gaussian kernels of 5 voxel FWHM and the two sets of US vessels were translated, rotated and scaled around their registered position on the MR vessel image. From the test results in Figure 3–4, we see similar profiles for the cross-correlation objective function for both sets of US data. The correlation of the objective function curves was greater than 0.9 for translation and more than 0.8 for rotation and scaling.

This indicates that there is high similarity between the registration performance of our simulated US vessels compared to that of the real US vessels. As well, the generated transforms and distortions from our digital phantom also vary smoothly and are of similar magnitude as that found in clinical cases in the literature. From this,

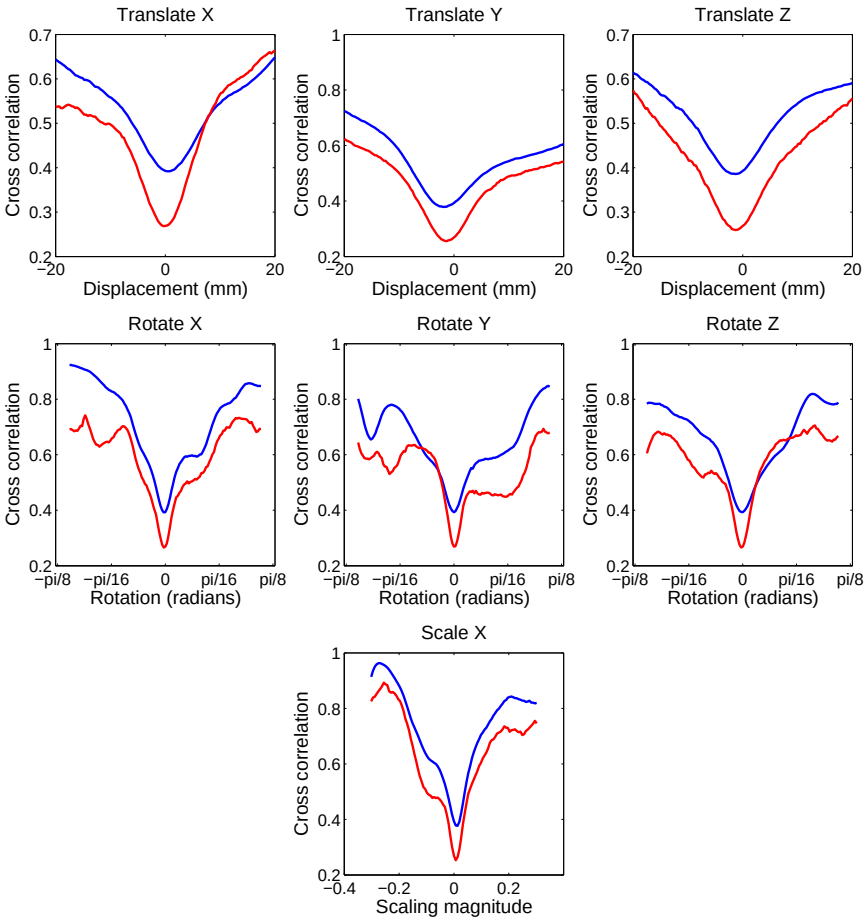

Figure 3–4: Graphed curves of showing correlation values of the simulated US (red) versus that of the real US (blue) when the vessels are translated (top row), rotated (middle row), or scaled (bottom row). The horizontal axes of the translation graphs, rotational graphs and the scaling graph are labelled in millimetres of translational displacement, radians of rotation, and magnitude of scaling about the center of gravity of the US vessel volume, respectively. All vertical axes of the graphs are show $1 - CrossCorrelation$. Cross-correlation between the translation curves in the x, y, and z directions are 0.91, 0.98, and 0.99, respectively. Cross-correlation between the rotation curves in the x, y, and z directions are 0.95, 0.82, and 0.88, respectively. Cross-correlation between the scale curves is 0.86. The offset of the two graphs show that the simulated US vessels has a slightly higher resemblance to the MR vessels since the former is simulated from the latter.

we can conclude that simulated US vessel volumes model the appearance of clinical US vessel images sufficiently well for testing our MR to US registration algorithm.

3.3.2 PVAc Physical Phantom

MRI and Doppler US vessel data of a polyvinyl alcohol cryogel (PVAc) physical brain phantom described and acquired by Reinertsen et al. [202] were used to validate our algorithm. The phantom is made of 3 types of PVAc of different hardnesses, containing 3 coils of plastic tubing with inner lumens of 1.57, 2.36, and 3.18mm, capable of circulating fluids for simulating blood vessels. The phantom also has an inflatable catheter located near its bottom center to simulate brain deformation [199]. The T1 MRI data set from this phantom consists of two image volumes for each catheter inflation of 0, 5, and 10ml of water, giving a total of 6 volumes (See Fig. 3–5) for improved validation. Three sets of 2 Doppler US images for phantom inflations of 0, 5, and 10ml were also acquired.

The MR images were acquired with a Siemens SonataVision 3T using T1 weighted MR imaging at a voxel resolution of 1mm x 1mm x 1mm. The tubes in the phantom were manually segmented from the MR images.

The phantom US images are acquired with an ATL HDI 5000CV US imager using a ATL P7-4 phased-array probe on power Doppler mode. A passive target with marker spheres was attached to the US probe and optically tracked by a Polaris tracker (Northern Digital Incorporated, Waterloo, Ontario, Canada). The ultrasound probe was calibrated with a z-fiducial phantom described in [87]. The US probe is swept smoothly and steadily by hand over the water-immersed phantom to minimize gaps in the reconstructed volume. The 2D Doppler images are filtered

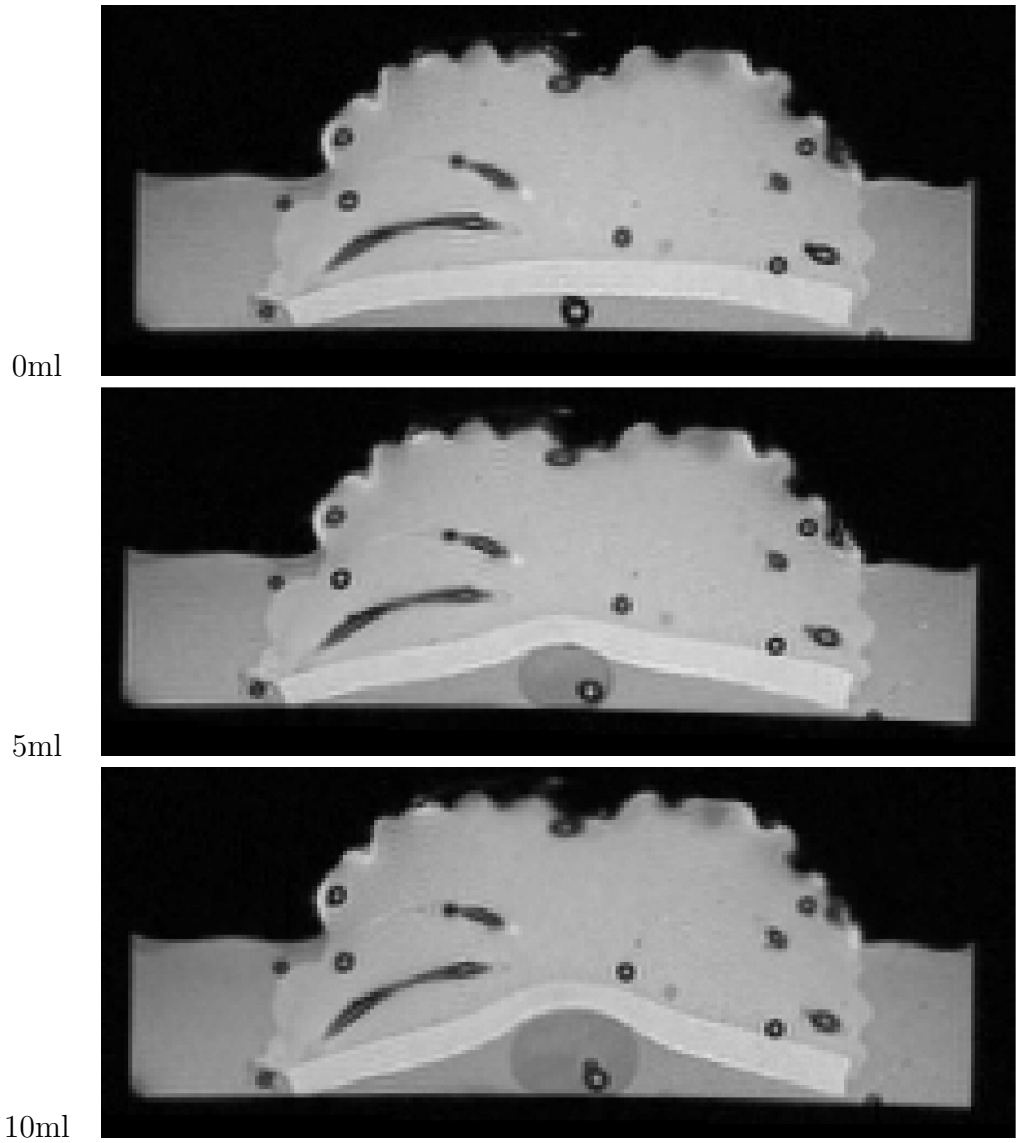

Figure 3–5: T1 MR images of the PVAc Phantom inflated with 0, 5, and 10ml of water in the implanted catheter, which can be seen at the bottom center of each image.

using a colour saturation threshold and reconstructed using the same methods as described in Section 3.2.1.

Manually labelled homologous landmark points, consisting of 21 fluid filled bubbles, located and distributed evenly throughout the phantom tissue material, were found in each of the 6 physical phantom MR volumes. These landmarks were used to validate the transformation of our algorithm. In 2 separate point picking trials to determine intra-rater variability, the mean difference between the points around each landmark was approximately 0.7mm with a maximum distance of 1.1mm.

3.3.3 Clinical Data Acquisition and Vessel Extraction

Vessel structures in preoperative MR and intraoperative US images must be properly acquired and extracted prior to registration. To acquire the preoperative image, the patient can be scanned using MR angiographic techniques, such as time-of-flight, T1-weighted MPR [237], or contrast enhanced MR angiography.

In our institute, open cranial surgery involving such procedures as tumour resection almost always involve Gadolinium (Gd) contrast enhanced MR imaging for enhancement of the pathology, usually within a week prior to their procedure. This also provides us with a contrast enhanced MR vascular image for use in computer assisted neurosurgical guidance. The images were acquired using a GE Signa Excite 1.5T with double-dose Gd enhanced T1 weighted MR imaging at an in-plane resolution of 0.5 x 0.5mm and a slice thickness of 1mm. The MR vessels are extracted by filtering the angiographic MR images using Frangi's vesselness method with the same parameters as those described in Section 3.2.1.

We note that although MR angiographic or contrast enhanced MR imaging may not be routinely performed in all institutes for tumour surgery, we nevertheless believe that the development of improved image processing methods may allow blood vessels to be extracted from standard T1-weighted images thus allowing for the use of a technique such as ours.

During the stabilization of the patient's head for operation, the pre-operative MR image was rigidly registered to the patient's head by the surgeon through manually picking nine facial landmark point pairs. These point pairs were chosen between the skin surfaces of the actual patient and the segmented patient MR image identified using optically tracked pointer and a mouse pointer, respectively. The point pairs consist of the patient's lateral and medial canthus on the left and right eye, the tragus and tragus valley on the left and right ear, as well and the most posterior part of the nasal bridge.

The clinical intraoperative US images and their tracking data were acquired and processed in the same manner as the physical phantom data to build the US volume from 2-dimensional slices and extract its vessels (see Section 3.2.1). The probe was swept in a free-handed manner over the dura of the patient after the craniotomy in a smooth and steady manner to minimize gaps in the reconstructed volume.

Table 3–2: Patient information and US scanning parameters for our 4 sets of clinical data

US Scan			**Patient**			
#	*Hz*	*Focus*	*Age*	*Sex*	*Pathology*	*Location*
1	4	8cm	70	Male	Glioblastoma	Left Frontal
2	4	8cm	40	Female	Glioblastoma	Right Parietal
3	4	8cm				
4	6	8cm	49	Male	Oligodendrocytoma	Left Frontal

Manually labelled landmarks for anatomical features found between the MR volume and the US volume were used as a silver-standard to evaluate registration success. These landmarks consist of blood vessel bifurcations, conjunctions of sulci, and unambiguous distal portions of ventricles located throughout the volume from 4 sets of real clinical data acquired from 3 patients (See Table 3–2). Depending on the size of the volumes and the availability of landmarks, between 7 and 18 unambiguous points were labelled by an expert. Four separate point picking trials were done to determine intra-rater variability. The mean difference between the points at each landmark was 1.3mm with the maximum distance of 2.1mm.

Given the clinical nature of these images and their acquisition conditions, it was difficult and took significant amounts of time to accurately identify unambiguous landmark points in both the US and MRI images. This process involves cross-checking between the preoperative and intraoperative images, re-verifying the landmarks, and correcting any inaccuracies, which can take around 15–30 minutes per case or around 2–4 minutes per landmark point. This was especially true for US acquisition 3, where the sweep amounted to a thin slab less than 2 cm in width and only 7 unambiguous landmark points could be identified.

3.3.4 TRE Calculations

We use the target registration errors (TRE) as a quantitative measure to test and validate our registration methods on our digital phantom trials, physical phantom trials and also our clinical trials.

Digital phantom trials: The TRE were calculated using an initial set of points, which were evenly sampled from throughout the ROI delimited sweep cone of

the US images. The initial points were then transformed using both the gold-standard transformations and the recovered transformations from our technique. The root mean square (RMS) errors between the latter two sets of points were then calculated to give us our TRE.

Physical phantom: The TRE were calculated using the labelled homologous fluid filled bubbles in the physical phantom images of each catheter inflation. The transformations recovered through registration of the source MR vessel image to the target US vessel image of a different inflation was applied onto the points picked from the source MR image. The RMS errors between transformed source points and the set of points picked from the target inflation image was then calculated, giving us our TRE.

Clinical trials: The TRE were calculated through a set of silver-standard point pairs, which were manually picked from homologous intra-cranial anatomical landmarks in the source MR image and the target US image. The transformations recovered using our registration technique were applied onto the source points and compared with the locations of the target points through computation of the RMS error as TRE.

3.3.5 Registration Validation

The hybrid registration algorithm was evaluated with the digital phantom (Section 3.3.1), the PVAc Phantom (Section 3.3.2), and 4 sets of real clinical data (Section 3.3.3). Although it is common in the literature to report translation and angular errors, we elected to use TRE for validation of our registration method since it can effectively encompass the displacements incurred from the full affine transformation

(12 degrees-of-freedom) used in our linear registration phase. This includes scaling and shear transformation on top of the translational and rotational transforms used in rigid-body registrations.

The TRE measure is also useful since it allows us effectively compare the quantities of error corrected between our linear and non-linear registration phases. Validation of the registration were done in the following manner for the digital phantom, the physical phantom, and the clinical trials datasets:

Digital phantom: Using the digital phantom, we created 2100 registration trials, each with a randomly generated vessel instantiation, transform, and deformations which were used as the gold standard. TREs greater than 2.5mm are considered as failed registration attempts.

Physical phantom: Validation using the physical phantom was performed by registering each of the 6 MR volumes with each of the 3 US volumes to estimate the non-linear transforms. This was done to account for deformations generated from inflating with 0, 5, or 10ml of water.

Clinical trials: Registration validation of the clinical trial was accomplished using manually defined landmark points used as the silver-standards that were chosen from homologous intra-cranial anatomical landmarks in the source MR image and the target US image.

3.4 Results

3.4.1 Digital Phantom

We found that our registration method was quite robust and accurate in correcting the simulated brain-shift of our digital phantom, with a high success rate given

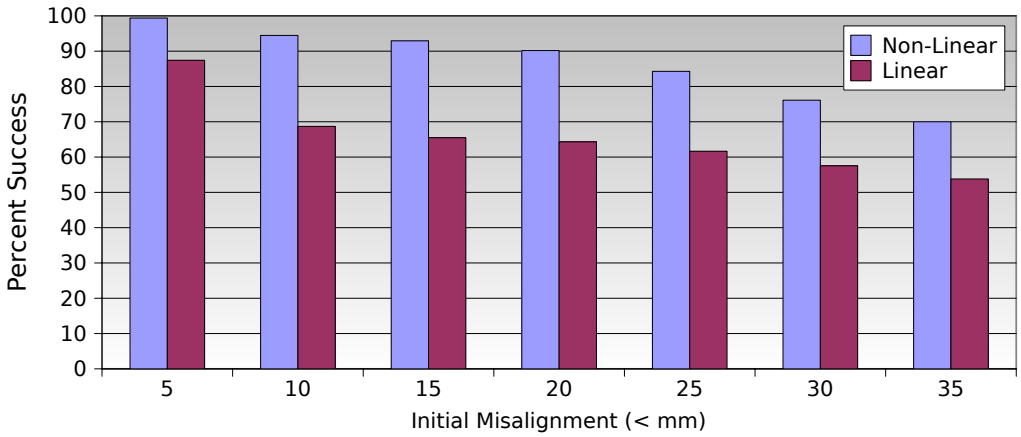

Figure 3–6: Digital phantom registration percent success on test cases of different initial misalignment RMS errors using the linear and non-linear phases of our registration algorithm. Registration trials with RMS errors of less than 2.5mm are defined as successful.

the 2.5mm threshold criteria. In applying our full registration method (linear and non-linear phases) to the digital phantom we found that our method was successful for 99%, 94%, 92%, and 90% of the digital phantom trials at 5, 10, 15 and 20mm initial misregistration, respectively (see Fig. 3–6, Non-Linear).

It is interesting to note that the linear step completed in the first phase of registration can significantly reduce the initial TRE. In the same trials as above, when initial misalignment RMS error is less than 5mm, 10mm, 15mm, and 20mm, the linear registration results in TREs less than 2.5mm for 87%, 68%, 65%, and 64% of the trials, respectively (see Fig. 3–6, Linear). These lower values are expected since linear transforms cannot completely correct for the local non-linear deformations we generated for our digital phantom. Furthermore, if the linear registration completed with a TRE of less than 6mm in these trials, the non-linear registration was successful more than 96% of the time, correcting the TRE to below 2.5mm.

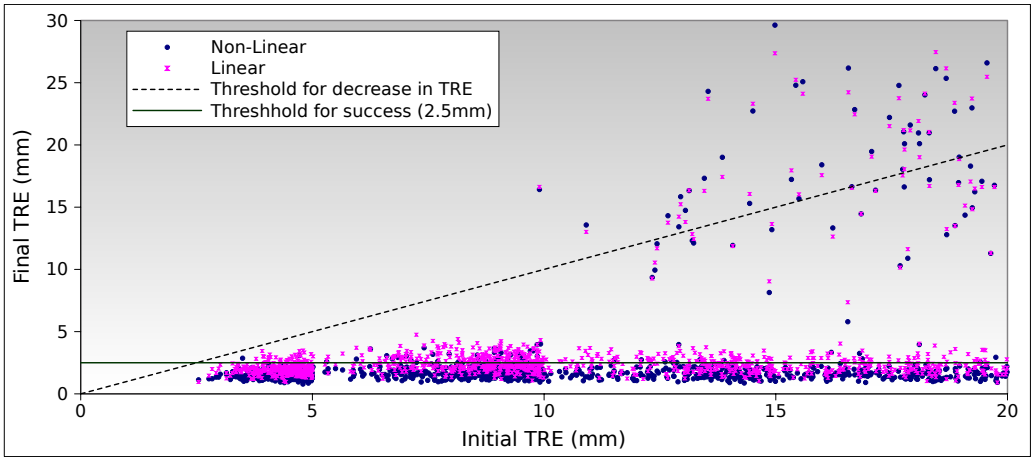

Figure 3–7: Digital phantom registration results showing the TRE for all the trials after the non-linear phase of the registration process. The horizontal axis indicates the initial TRE prior to correction while the vertical axis indicates the final TRE after non-linear registration. The blue circles are the results after non-linear registration and the pink X's are the results after linear registration. The black diagonal line shows where a registration trial resulted in the reduction in TRE (point is below the line) or whether it increased the TRE (point is above the line). The green horizontal line shows our cutoff for success (2.5mm). The mean reduction of 0.62mm TRE from linear to non-linear phases of registration is highly significant, with $p < 2 \times 10^{-64}$ in a two-tailed t-test.

Given the initial design criteria of 20mm maximum displacement on the dura, only 10% of the trials failed with TREs greater than 2.5mm. We found that only 3% of the registration trials attained a greater TRE than the initial alignment (see Fig. 3–7). The mean reduction in TRE through non-linear registration from the linear registration results is 0.62mm and quite significant, with $p = 1.73 \times 10^{-64}$ in a two-tailed t-test. This significant reduction in TRE can also be seen in that the mean TRE after linear registration was 2.29 ± 0.62mm with the first and third quartile being 1.84mm and 2.66mm, respectively, which reduced after non-linear registration to 1.64 ± 0.47mm with the first and third quartile being 1.32mm and 1.82mm, respectively. In general, we found that the regions of the US volume with the least blood vessels had the highest TREs while regions surrounded by vascular structures had consistently low TREs.

We also tried to examine the behaviour of the vessel registration algorithm when we push it beyond the 20mm operating range. We see that in this case the success in the non-linear registration was only 84%, 76%, and 70% for 25mm, 30mm, and 35mm initial misregistration.

3.4.2 PVAc Phantom

In our tests with the physical PVAc phantom, our non-linear registration algorithm was able to correct the deformations in all our trials to TREs 2mm or under (See Table 3–3). This correction corresponds to a reduction of 8% to 45% in TRE remaining from the linear registration step after non-linear registration, with the TREs decreasing in all cases in these tests on the physical phantom. This demonstrates that the algorithm is likely converging towards the correct solution.

Table 3–3: TREs resulting from applying the non-linear registration algorithm on 6 linearly registered physical phantom MR images (Fin) and the initial TREs (Init). The MR images were acquired by inflating the physical phantoms twice (*1*, *2*) with 3 different volumes of water (0, 5, 10ml). The transforms are computed by registering each physical phantom MR source image with the remaining phantom US target images of dissimilar inflation volumes. Source images are listed as rows while target images are listed as columns in the table.

		0ml				**5ml**				**10ml**			
		1		*2*		*1*		*2*		*1*		*2*	
Volume	**#**	**Init**	**Fin**	**Init**	**Fin**	**Init**	**Fin**	**Init**	**Fin**	**Init**	**Fin**	**Init**	**Fin**
0ml	*1*	×	×	×	×	1.8 → 1.1		2.6 → 1.9		1.7 → 1.1		2.7 → 2.0	
	2	×	×	×	×	1.8 → 1.6		1.4 → 1.3		1.7 → 1.4		1.9 → 1.7	
5ml	*1*	2.6 → 2.0		1.4 → 1.3		×	×	×	×	1.4 → 1.2		2.6 → 2.0	
	2	1.7 → 1.5		1.4 → 1.1		×	×	×	×	1.6 → 1.3		1.8 → 1.6	
10ml	*1*	2.7 → 1.8		1.8 → 1.1		1.6 → 1.1		2.6 → 1.8		×	×	×	×
	2	1.9 → 1.0		2.6 → 1.9		1.8 → 1.0		2.6 → 2.0		×	×	×	×

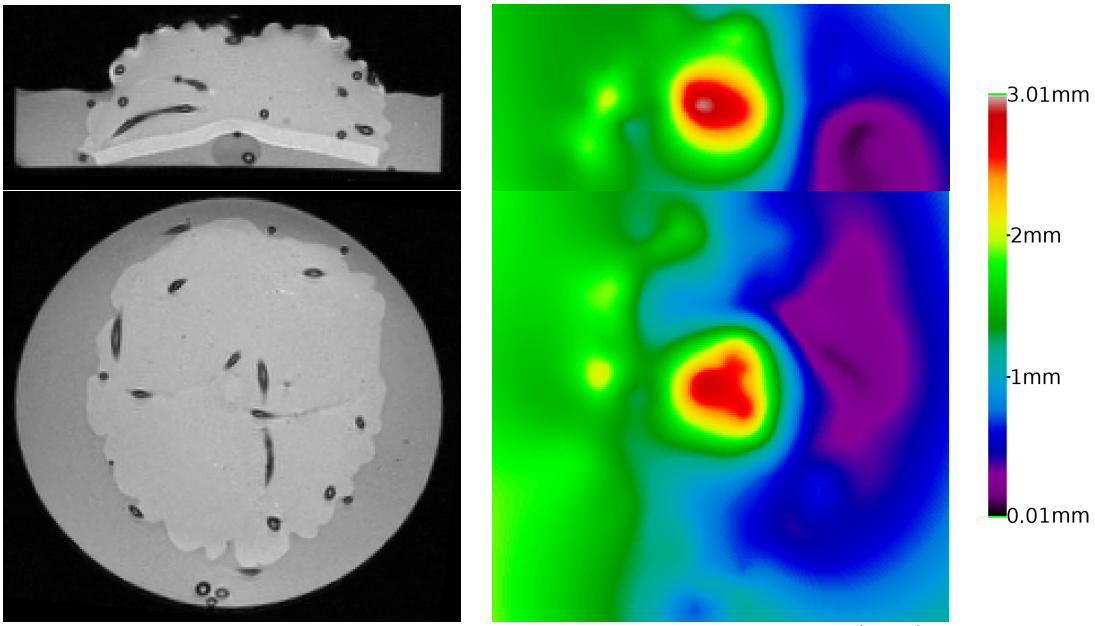

5ml MR Image Deformation Magnitude (mm)

Figure 3–8: PVAc Phantom with 5ml inflation (Left) and its corresponding magnitude of deformation when non-linearly registered to the 0ml inflation phantom (Right). The magnitude of non-linear deformation is highest around the center of the phantom where the inflation catheter resides with the maximum recovered deformation of 3.01mm and the minimum of 0.008mm.

It should be noted that since the chosen landmarks on the PVAc phantom are spread out evenly over the entire volume of the phantom, the actual amount of non-linear displacement an their corresponding correction through registration has been diluted in calculation of the TRE. To illustrate this, we used the results of the 0ml to 5ml registration trial and calculated the TRE from 5 landmark points located in a region of the phantom closer to the catheter balloon. From this, we noted a reduction of TRE from 2.4mm to 1.3mm, which equals to a 46% reduction in the TRE of this region from our non-linear registration alone. The differences in the magnitude of non-linear deformations throughout the image can be seen in Figure 3–8. The degree of non-linear deformation was as high as 3.01 mm, in the region close to the center of the imaged volume where the deformation inducing catheter resides.

Images showing a 5ml inflated phantom corrected with the recovered transformations from registration with a 0ml inflated phantom can be seen in Figure 3–9. Note that there is almost a complete overlap of the vascularized cerebral region of the phantom images, including the more highly deformed parts of the phantom near the catheter.

3.4.3 Clinical Data

The initial registration of the MR to the patient's head attained from the facial landmarks for the clinical data was achieved with the standard homologous landmark point-pair method described in Section 3.3.3. Only one starting point was evaluated for each clinical case, since experiments using the synthetic phantom data have indicated the algorithm's robustness to the starting location. These initial mean TREs from facial registration using the manually identified silver standard landmarks on

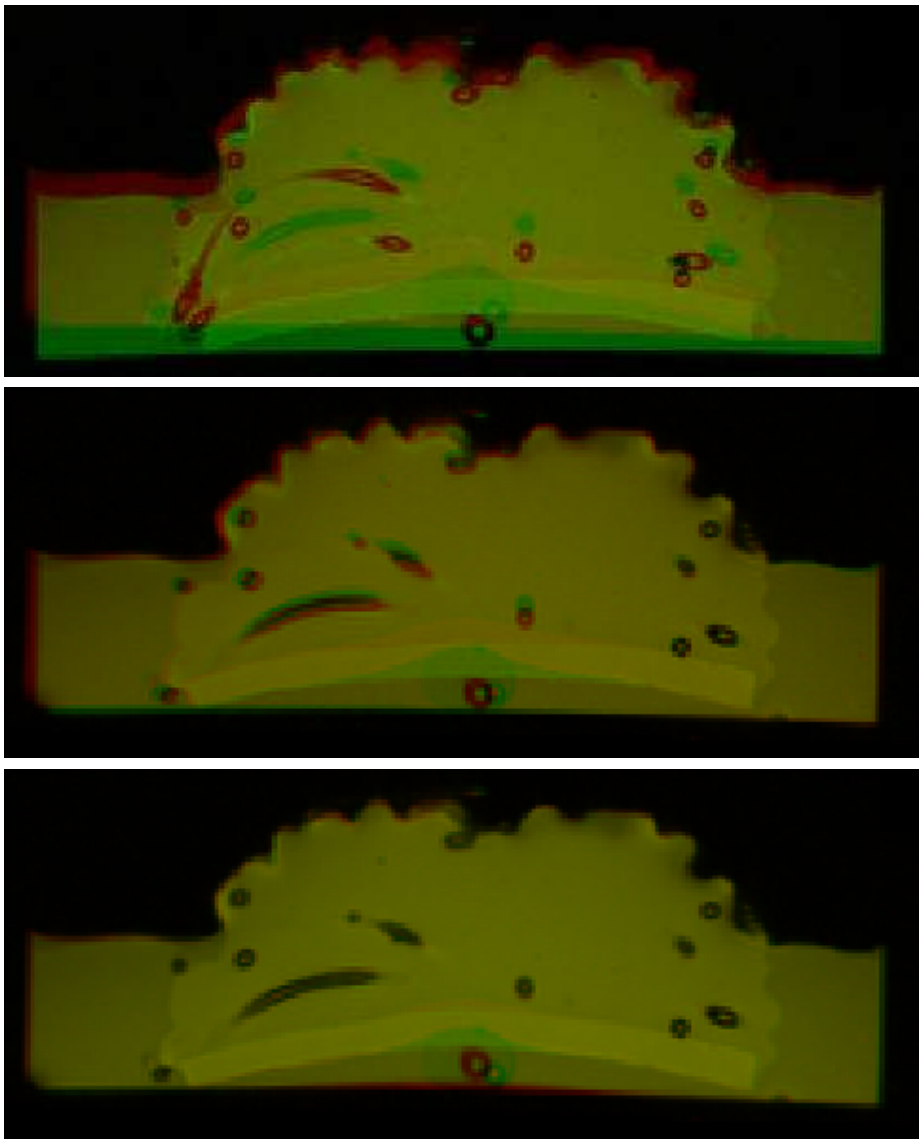

Figure 3–9: PVAc Phantom with 5ml inflation image (red) being registered to its 0ml inflation image (green). The image initial alignments shows considerable misalignment. After linear registration, alignment is greatly improved but a large amount of misregistration can be seen in the left side of the image and close to the inflatable catheter. Following non-linear registration, most of the phantom is well aligned.

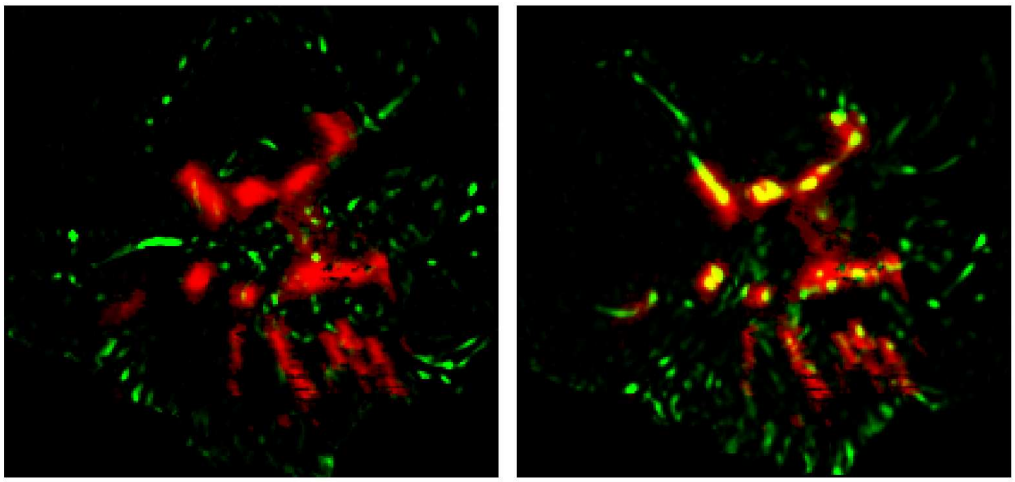

Figure 3–10: Registration results showing improved alignment of the preoperative MR vessels (Green) with the intraoperative US vessels (Red). The images show a transverse slice plane of the US volume and the same slice plane through the misaligned MR volume before (Left) and after (Right) applying the transformations recovered using our hybrid registration method. Notice that the MR vessels previously misaligned and out of plane to the US vessels are now well registered. The images are from Patient 1 in Table 3–4.

Table 3–4: Full registration TREs for our 4 sets of clinical data. The first row shows the TRE from intra-operative patient facial registration, the second row shows the results of our method after the linear registration phase, the third row shows the final results of our method after the linear and non-linear registration phases, the forth and fifth rows show the percent reduction of TRE from the facial registration to the linear and both linear and non-linear registration phases, respectively. The sixth row shows the additional percentage of TRE reduction following the non-linear registration after linear registration. The last row indicate the number of landmarks used to determine TRE on each patient dataset.

Data sets #	**1**	**2**	**3**	**4**
Facial Registration TRE	7.25mm	3.51mm	4.61mm	3.74mm
Linear Registration TRE	3.48mm	1.32mm	3.50mm	2.12mm
Non-linear Registration TRE	2.38mm	1.23mm	3.38mm	1.70mm
Linear % Reduction	52.0%	62.3%	24.2%	43.3%
Non-linear % Reduction	67.2%	64.9%	26.7%	54.5%
% Difference	15.2%	2.6%	2.5%	11.2%
# of Target Landmarks	18	7	15	8

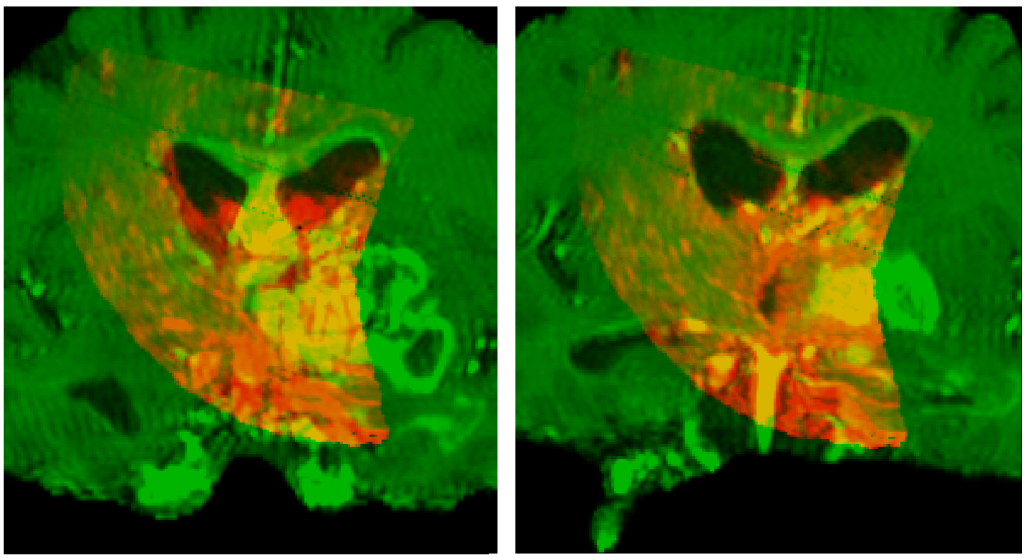

Figure 3–11: Registration results using clinical data, with overlays of the dual-mode US (Red) on the Gadolinium-enhanced T1 MR images (Green). The images show a coronal slice plane of the US volume and the same slice plane through the misaligned MR volume prior to (Left) and after registration (Right). The TREs for this subject (Patient 1 in Table 3–4) before registration is 7.46mm and 2.88mm afterwards. Note the improved alignment of the sulci and ventricle borders.

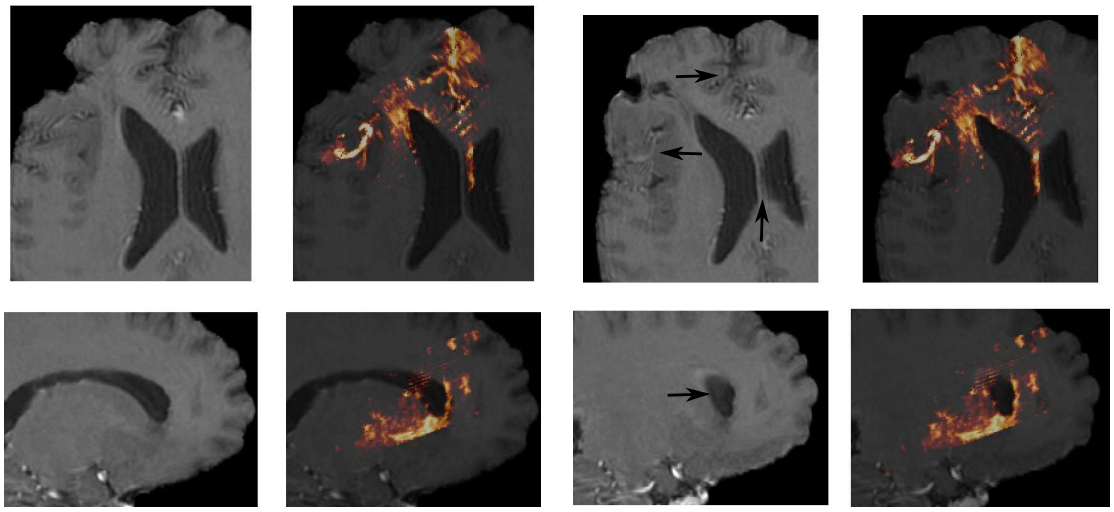

Prior Registration After Registration

Figure 3–12: Registration results using clinical data from Patient 4 (see Table 3–4), with the non-overlayed Gadolinium-enhanced T1 MR images (Left) and overlays of the hot-metal toned dual-mode US on the MR images (Right) in both coronal (Top) and sagittal planes (Bottom) prior to and after registration. The TRE before registration is 3.75mm and 1.7mm afterwards. The arrows on the non-overlayed registered MR image indicate areas of improved alignment at the vessels, sulci, and ventricular borders through the use of our registration method.

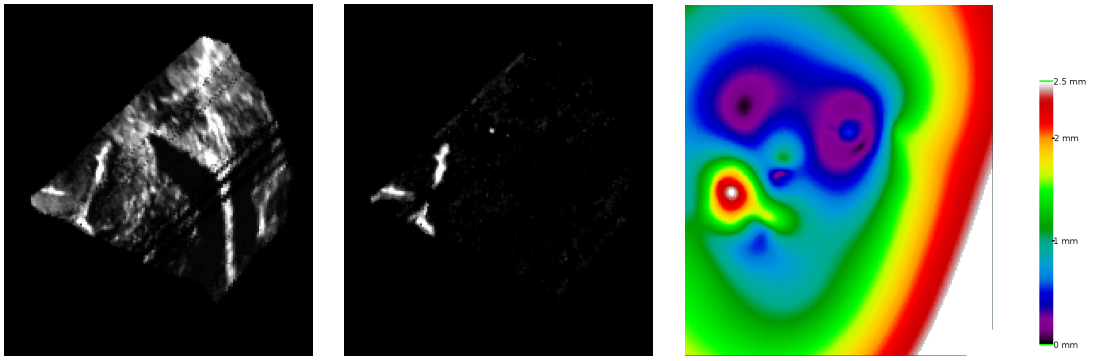

B-mode Image Doppler Image Deformation Magnitude (mm)

Figure 3–13: Images from Patient 4 (see Table 3–4) showing a coronal slice from the reconstructed US image (Left), the Doppler US vessel image (Middle), and the magnitude of non-linear deformation recovered after the linear registration phase (Right). This reveals that significant non-linear deformation occurs even prior to dural opening. The magnitude of non-linear deformation recovered from MR to US registration was very high close to the Doppler vessels with the maximum recovered deformation of 2.5mm and the minimum of 0.006mm. Note that the deformation field can be high in the borders of the image where there are no vessels to "lock-down" the amount of deformation in these regions.

the four datasets were 7.25mm, 3.51mm, 4.61mm, 3.742mm. It is important to note that although our surgeons sought to keep the root mean square errors of their facial landmark fiducial registration errors (FRE) lower than 1.5mm, the resulting TREs from the initial skin-based registration are nevertheless quite large. The magnitude of the TREs is likely due to the configuration of skin landmarks in relation to the surgical target. If the geometric center of gravity of the fiducials is not close to the surgical target, the landmark configuration may lead to a lever effect, accentuating the TRE. Such a decorrelation between the measured FRE from the measured TRE has been noted in the past [59, 221, 222].

After the US to MR registration process consisting of the linear and nonlinear registration steps, the TREs were reduced to 2.38mm, 1.23mm, 3.38mm, and 1.70mm on these clinical datasets with improvements of TRE by 67.2%, 64.9%, 26.7%, and 54.5%, respectively. Resulting images from registration of Patient 1 (See Table 3–2) can be seen in Fig. 3–10 and 3–11, which are respectively the registered vessel images and the T1 MR image corrected with the recovered transformation. Resulting registered images for Patient 4 in Fig. 3–12 show the T1 MR image corrected with the recovered transformation. It can be seen that the amount of non-linear deformations from datasets 1 and 4 are not negligible, with 15.2% and 11.2% of the TRE uncorrected by affine-linear registration (See Table 3–4). The magnitude of non-linear deformations in Patient 4 was as high as 2.5 mm in some local regions of the brain, and can be seen in Fig. 3–13. Note that this deformation was recovered from our vessel based registration after completion of our linear registration phase, from images acquired prior to dural opening. This indicates that full affine-linear

registration alone is insufficient to capture and recover all the brain-shift induced deformations even prior to dural opening.

The average execution time for vessel registration is roughly 6–8 minutes on a 2.4 GHz Intel Q6600 processor. In this time span, the multiscale linear registration takes approximately 3-4 minutes and non-linear registration takes approximately 3-5 minutes, with the rest of the time taken up by US preprocessing and volume reconstruction, which takes less than a minute.

3.5 Discussion

The validation results indicate that the hybrid registration algorithm outlined in this paper can be applied to correct for registration errors due to inaccurate fiducial registration and to update preoperative images to account for brain shift.

3.5.1 Validation

Our method can successfully correct for brain shifts with displacements as large as 20mm in more than 90% of the cases (See Fig. 3–6 and 3–7) in our digital simulations. As well, we have found in our clinical cases that we can significantly reduce the registration TRE with either only linear registration or both linear and non-linear registration (See Table 3–4). However, we note that these results need to be interpreted with care given that our digital simulation is not entirely physically realistic and that we have evaluated the technique only on 3 patients in our clinical trials. We plan to apply the method to a larger cohort of patient data in the future to further validate and determine the generalisability of the results. We also intend to improve our methods for simulation of US blood vessels to make them more physically realistic. We also note that while our clinical cases used specified facial

landmarks for initial registration, it is also possible to use a random iterative closest point method such as that of [76] for initial rigid body registration, before applying our hybrid method for non-linear soft tissue registration.

Our digital phantom occasionally removes large regions of vessel segments in its random vessel presence simulation. On some of these simulated US images, our hybrid registration algorithm fails catastrophically, with the resulting TREs significantly higher than 2.5mm even when the initial TREs are less than 20mm. We realized that the removed vessel segments was the cause of the failure when we qualitatively examined several of the generated US digital vessel phantom images that resulted in registration failures. The simulated US volumes were indeed significantly sparser due to vessel removal and as such they aligned themselves to the wrong vessels in the larger sized MR vessel volume image. When the same images were not processed with the random presence portion of the simulation and ran with the same initial misalignments, registration of these same images converge and succeed even with the added noise, artifacts, and large vessel dilations.

The reason for the catastrophic failure in registration is clear. Since the initial vessel images used in digital simulation is already quite sparse, masking and vessel removal can further weaken the global minimum to the point as to cause the algorithm to be trapped at one of the many local minima. This introduced ambiguity in effect increased the possible alignments of the smaller and sparser US image with the large amount of vasculature in the MR vessel image. The problem was further exacerbated when the misalignment distance of the images was greater, which required the algorithm to traverse across more local minima and increased the chances that

it would settle into any one of them before reaching the global minimum. Should the vessel removal be extensive enough, the global minimum for registration could be eliminated, causing the registration algorithm to never converge to the correct solution. Although these large failures in alignments are not favourable, there are nevertheless benefits to such a behaviour since it allows technicians and surgeons to easily recognize registration failure through visual inspection, which limits the chance that a wrongly registered image is accepted by the surgeon and used for guidance.

We noticed a reduction in the TRE in all the physical phantom registration trials, and although the values were not below 1mm, visual inspection of the registration results show marked improvements in the alignment of the blood vessel tubes in the phantom (See Fig. 3–9). This is similarly true with the registration results using clinical data, where the corrections showed good alignment not only in vessels (see Fig. 3–10) but also in anatomical structures such as the ventricles and sulci (see Fig. 3–11 and 3–12). Although anatomical structures like ventricles can be useful in registration, they are not as topologically distinct as branching vessels and are not well distributed throughout the brain tissue. Nevertheless, structures such as ventricles and sulci can be used as additional registration features in conjunction with vessels in registration. While we realize we cannot generalize with 4 clinical data sets, these tests do demonstrate that our algorithm can be successfully used to register real clinical images acquired intraoperatively during an operation.

3.5.2 Hybrid Vessel Registration

Ideally, we would have liked to compare our techniques to other US to MR registration techniques such as of [110] and [208], however these techniques are dissimilar

to our own in that (1) they recover linear transformations only and do not recover non-linear deformations in their registration, (2) nor do they take advantage of the vessel information in their images for image registration. As well, these techniques are not publicly available and trying to both implement and run them ourselves might introduce bias. Nevertheless, we have run several tests against Reinertsen et al.[201], which show that our technique, although slower, is more accurate, more robust, and has a higher probability of converging to the correct solution when run on real clinical data and image data from our digital phantom. We intend to continue investigating the use of our technique after and during tumour resection since these situations will likely be more challenging due to the higher tissue distortion and tissue removal. In both cases, the amount of resected tissues will be quite large, but since our registration technique relies on blood vessels for registration and not the removed tissue and can deal with missing vessels segments we believe that it should work well in such situations.

While the total time of 6–8 minutes required for hybrid registration is perhaps pushing the limits of clinical acceptance, this work was done with the intention of evaluating a technique to first determine its functionality and robustness on clinical data prior to further optimization. We believe that optimizing the code for the algorithm as well as adapting it to use hardware acceleration can reduce the registration time required. However, since the present algorithm is highly robust for misalignments up to 20mm (more than 90% success, See Fig. 3–6), it should be possible to account for large absolute displacements by progressively estimating smaller relative displacements during the procedure. For example, the deformation estimated using

the algorithm before dural opening will be used as the starting transformation for the subsequent deformation estimations during or after a surgical procedure. While this method remains to be tested with additional clinical data, we believe the registration algorithm, when used continuously, could correct for deformations of 10-15mm that occur throughout a procedure.

In this work, we concern ourselves solely with the problem of registering US data acquired on the dura. We believe that by being able to correct brain-shift first on the dura, we can subsequently evaluate our registration algorithm in surgery before proceeding to tackle the potentially more difficult problems of image registration after dural opening and tissue resection. We realize that the characteristics of brain shift and the performance of the algorithm may be altered depending on the size and location of the craniotomy or the presence of tumour tissues, but this is outside the scope of our paper and will be addressed in future research.

3.5.3 Conclusion

We have presented a new method for correction of preoperative MR images using intraoperative US for non-linear hybrid vessel registration. Since our vessel registration algorithm does not depend heavily on image preprocessing for robust and accurate results, it is able to avoid the pitfalls of feature-based registration methods that rely on their preprocessing methods such as vessel centerline registration algorithms. The minimum processing to extract the vessels allows us to complete registration in less time than purely intensity-based registration techniques.

In this work, we also developed a digital phantom capable of synthetically generating volumes with the appearance of Doppler US vessel images. These images are

processed from a MR vessel image and have known ground truths for testing the registration robustness and accuracy of various non-linear MR to US vessel registration algorithms.

Our registration algorithm was then validated for robustness and accuracy through multiple trials using synthetic US vessel images generated from our digital phantom, along with US and MR images scanned from a real physical phantom, and finally 4 sets of real clinical data from 3 patients consisting of preoperative MR vessel images and intraoperative Power Doppler US images. Results from these tests show that the estimated transforms recovered by our novel registration algorithm are not only accurate but also robust when processing images that contain large quantities of noise, artifacts and missing vessels commonly seen in clinical vessel images.

3.6 Acknowledgements

We would like to thank Marta Kersten and Lara Bailey for proofreading the manuscript. We are also grateful to the Natural Sciences and Engineering Research Council of Canada (NSERC), the Canadian Institutes of Health Research (CIHR), and Le Fonds Quebec de la Recherche sur la Nature et les Technologies (FQRNT) for funding this project.

CHAPTER 4
Brain Phantom for the Validation of Medical Image Processing

Forward

In Chapter 3 we presented our methods for vessel-based intraoperative registration, and demonstrated their robustness and accuracy in image alignment. However through our registration work, we noticed that the available physical phantom used in the study did not deform realistically in the manner of live human brain and lacked imageable anatomical features and landmarks for validation. Newly developed medical image processing techniques, such as those for image segmentation and registration, need realistic physical imaging phantoms with distinct geometries and known imaging behaviours to properly characterize and validate their accuracy.

In this chapter we describe the design and construction of a multimodal anthropomorphic medical imaging phantom that can be imaged using ultrasound, computed tomography, and several magnetic resonance imaging modalities. We present the chemical formulation of the brain phantom's polyvinyl alcohol cryogel tissue mimicking material. This material has been formulated for contrast in MR, CT, and ultrasound and also to have mechanical properties similar to a live human brain. The phantom's mold was created from a digital model based on the left hemisphere of Holmes *et al.* [103] and contained deep sulci, a full left ventricle, and a complete insular region. As well, multimodal fiducial spheres were implanted to allow for image alignment validation of registration algorithms. Inflatable catheters were also cast

into the phantom to simulate realistic non-rigid soft tissue deformation. Finally, we also present the multiple sets of MR, CT and US data acquired from this phantom, which were made freely available to the public and the medical image processing community.

Using this multimodal imaging phantom, it is possible to validate image segmentation, reconstruction, registration, and denoising techniques. We believe that our phantom can be used to aid in the future development of novel medical image processing techniques.

This chapter has been published in *Medical Physics* [38]:

- S. J.-S. Chen, P. Hellier, M. Marchal, J.-Y. Gauvrit, R. Carpentier, X. Morandi, and D. L. Collins. An anthropomorphic polyvinyl alcohol brain phantom based on Colin27 for use in multimodal imaging. *Medical Physics*, 39(1):554–561, 2012.

Manuscript: An Anthropomorphic Polyvinyl Alcohol Brain Phantom Based on Colin27 for Use in Multimodal Imaging.

Sean Jy-Shyang Chen [1], Pierre Hellier [2], Maud Marchal [3], Jean-Yves Gauvrit [4 5], Romain Carpentier [4 5], D. Louis Collins [1]

[1] McConnell Brain Imaging Centre, Montreal Neurological Institute, McGill University, Montreal, Canada
[2] INRIA Rennes, EPI Serpico, IRISA, F-35042, Rennes, France
[3] INRIA Rennes, Bunraku, IRISA-INSA, F-35042, Rennes, France
[4] INRIA VisAGes U746, IRISA, F-35042 Rennes, France
[5] Université de Rennes 1, 35065, Rennes, France

Abstract

In this paper, the method for the creation of an anatomically and mechanically realistic brain phantom from polyvinyl alcohol cryogel (PVA-C) is proposed for validation of image processing methods such as segmentation, reconstruction, registration, and denoising. PVA-C is material widely used in medical imaging phantoms because of its mechanical similarities to soft tissues. The phantom was cast in a mold designed using the left hemisphere of the Colin27 brain dataset [103]. Marker spheres and inflatable catheters were also implanted to enable good registration comparisons and to simulate tissue deformation, respectively. The phantom contained deep sulci, a complete insular region, and an anatomically accurate left ventricle. It was found to provide good contrast in triple modality imaging, consisting of computed tomography, ultrasound, and magnetic resonance imaging. Multiple sets of multimodal data were acquired from this phantom. The methods for building the anatomically accurate, multimodality phantom were described in this work. All multimodal data is made available freely to the image processing community (`http://pvabrain.inria.fr`). We believe the phantom images could allow for the

validation and further aid in the development of novel medical image processing techniques.

4.1 Introduction

The human cerebrum is a topologically complex organ with deep fissures and sulci over its lateral and medial surfaces, as well as fluid filled ventricles of complex shape and form in its interior. The creation of a physical model capable of depicting the form of the cerebrum is not trivial due in part to these deep structures. Previous works in creating brain phantoms have either reduced the depth of the sulci [240], or only recreated the form of the brain superficially with dessert gelatin molds [200, 199]. Although these phantoms bear a cursory resemblance to the human cerebrum, they do not accurately depict the gross anatomy of the brain. Registering these phantoms to their acquired multimodality images may also not be straightforward since the landmarks on the phantom are not easy to find or image. This may be due to the structures being smaller than the imaging resolution or because of insufficient contrast of the markers with respect to its surroundings. For instance, [199] relied on the presence of bubbles in their phantom to act as landmarks for validation of their phantom. While trapped bubbles can be useful as landmarks in phantom validation, their locations cannot be controlled. Even when the bubbles are present, they may also be difficult to identify uniquely. To address these issues, multimodal landmarks need to be placed in the phantom.

The objective of this study is to create a triple modality human brain phantom with anatomically realistic structures and mechanical properties such as approaching that of a live human brain. Henceforth, we will collectively refer to these properties as

"texture". The material selected for constructing this phantom is polyvinyl alcohol (PVA), which is a polymer synthesized from polyvinyl acetate by hydrolysis of their acetate groups [240].PVA is commonly used in industrial products such as adhesives, strengtheners for fibre products, thickeners for paints and other liquids, as well as in for the creation of films, emulsions, and coatings for various engineering purposes [219, 199]. When liquid PVA solutions undergo a specified period of freezing at a set temperature and are then allowed to thaw slowly to room temperature, this freeze-thaw cycle (FTC) transforms the liquid PVA solution into a elastic semi-opaque gel know as polyvinyl alcohol cryogel (PVA-C) [183, 236, 184, 41].

In previous studies, soft tissue phantoms made from PVA-C have been used to develop, characterize, and refine different imaging or image processing methods [67, 161, 155]. PVA-C is a good material for such studies since it has similar mechanical properties such as compressibility and water content to many soft tissues [67, 161, 155, 84, 115, 199, 240]. PVA-C has many other desirable characteristics for building phantoms. For example, can be stretched 5 to 6 times its original dimensions without tearing or rupturing, while its high degree of elasticity lets it return to its original shape with little permanent deformation [184, 115]. With cold storage and the addition of biocides, PVA is also relatively tough and long-lasting when compared with other similarly textured materials such as gelatin or agar [84, 115]. PVA-C is also safe for normal handling in that it is biocompatible and nontoxic [84]. Finally, the gelling and setting of PVA into PVA-C is relatively uninvolved, requiring only the freezing and thawing of the molded PVA solution.

For these reasons, PVA-C has been used in the construction of soft tissue phantoms and to study a wide variety of tissues including those of the heart [137, 111], breast [161, 155, 241], prostate [115], arterial vasculature [69, 41, 240], and brain [199, 240], in addition to lesions and tumours within these tissues [161, 155, 115]. In the following sections, we describe the methods we used to create our brain phantom. We seek to contribute to the literature a phantom that has:

Anatomical accuracy Deep cortical structures of the Colin27 cerebrum, such as the sulci, the insular region and the ventricles are realistically represented in the cast phantom.

Realistic texture Recipes of PVA-C with textures approaching that of live human cerebral tissues were determined through the feedback of a neurosurgeon who knows the texture of the human brain and tumour tissues.

Multimodal imaging A single phantom that can be imaged effectively in computed tomography (CT), ultrasound (US) and magnetic resonance (MR) modalities with good contrast between phantom and water as well as between the phantom and its implants.

Freely available data Images acquired using the US, MR, and CT scanners are made available through our website to researchers and the general public. Images for this phantom were acquired using magnetic resonance imaging (T1 and T2 weighted, PD, FLAIR, and DTI), ultrasound imaging, and computed tomography, to ensure that the phantom exhibits similar contrast to images of the live cerebrum acquired using these imaging modalities.

We also embedded inflatable catheters in the manner of [200] to simulate deformation from brain-shift, which is caused by the non-linear distortion of brain tissue due to gravity and brain swelling from various physiological factors.

Potentially any PVA-C formula can be used to cast the brain phantom provided that it can be easily removed from the mold and that it holds its form once unmolded. However, we have noticed in past experiments that attaining the right phantom texture is important in getting realistic deformation through catheter inflation. As such, we believe that a PVA-C formulation that approximates live brain texture is desirable for the construction of our anatomically accurate phantom in order to validate non-linear image registration algorithms and other image processing methods. Furthermore, the PVA-C formulation must be able to suspend the contrast agents used in the phantom (i.e., without settling out) during the casting of the phantom.

As such, although an imaging phantom will not necessarily need to have both anatomical accuracy and a realistic texture, in this work we strove to incorporate both of these requirements into our phantom.

In following sections we describe the methods for preparing the PVA-C material, the added contrast agents, the creation of the phantom mold, and our multimodal image acquisition of the phantom. We conclude the paper with a listing of our Results followed by a Discussion of the work.

4.2 Material & Methods

4.2.1 Preparing PVA-C

The PVA solutions used to cast the PVA-C brain phantom and its various components were prepared using 99-100% hydrolysed PVA with an average molecular weight of 86 kilodaltons from Acros Organics (Geel, Belgium; Code:418120010).

Master PVA solutions were prepared in large quantities by combining heated distilled water of a certain mass with PVA solute of another mass. The final mass of PVA solute will make up a specific percentage of final solution's mass. This is known as mass percentage, and is commonly abbreviated as w/w. In our experiments, master PVA solutions of 5% (w/w) and 8% (w/w) were prepared.

The mixture was constantly stirred until the PVA particles are well hydrated upon which the holding vessel of PVA and water mixture was placed in an oven of 93-95°C for several hours. This ensures temperature homogeneity in the liquid and that the PVA granules dissolve properly. We were also careful to keep the temperature of the holding vessels below 100°C to minimize water loss and the formation of polymer films on the liquid surface. These parameters were taken from the solution preparation guidelines of Celvol PVA of a similar grade to what we were using [219].

The finished master solutions were checked visually to ensure that all PVA granules had been dissolved. Small quantities of distilled water were added back into the solutions according to the amounts lost during preparation of the PVA solution. From these PVA master solutions, base solutions of lower mass percentages could be produced by heating the master solution and mixing in additional water.

PVA-C was polymerized from a PVA solution by completely freezing and thawing the solutions, which results into semitransparent flexible gel. The PVA solutions were placed in a room temperature (25°C) chest freezer and cooled to between -25° to -20°C. After 12 hours of freezing at the aforementioned temperatures, the freezer was stopped and its interior was allowed to rise back to room temperature over another 12 hour period. The cycles were varied from 1 to 3 FTCs to produce a range of different PVA-C texture consistencies.

4.2.2 Choosing a PVA-C Formula

Figure 4–1: Samples of PVA-C from 4-8% (left to right) and 1-3 freeze-thaw-cycles (top to bottom). Note that the samples that have undergone 1 freeze-thaw-cycle (FTC) samples are more translucent than higher FTC samples. Note that the 4% 1 FTC sample is deforms significantly under its own weight.

In order to select a PVA-C formula (PVA solution concentration and FTC) that would provide a texture similar to that of a live human brain in our deformable brain phantom, we employed the subjective assessment of a neurosurgeon with 21 years of experience in vascular and skull base surgery, who was familiar with the texture of the human brain and its pathologies. The surgeon was asked to palpate an array

of PVA-C samples that had been prepared with either 1, 2, or 3 FTCs and 4%, 5%, 6%, or 8% PVA solutions (12 PVA-C samples in total; See Fig. 4–1). During this exercise, the samples were palpated at room temperature by the neurosurgeon while gloved and blindfolded. The neurosurgeon was asked rate the similarity of each sample to human brain tissue on a scale of 0 (least similar) to 10 (most similar). The aforementioned procedure was then repeated to choose the samples which felt most like low grade gliomas.

We note that this strategy for selecting a PVA-C formula is subjective and cannot be used to draw conclusions about the quantitative rheological properties of live human brain tissue beyond the needs our tests. These properties should be measured and quantified using elastography or more directly through intraoperative mechanical tests. Along with additional information from the formal characterization of the rheological parameters of our PVA-C samples, we should be able to better select a PVA formula that is quantitatively similar to the mechanical properties of human brain.

4.2.3 Triple Modality Contrast Agents

Commonly available chemicals were used to change the contrast between the phantom and water for all modalities (US, MR, and CT). A PVA-C with the PVA concentration and FTC resembling textures similar to a living human cerebrum was chosen to be the base solution for dissolving the contrast enhancing chemicals. We list all quantities of contrast medium added to the PVA solution as mass percentages (w/w) of the chosen PVA solution.

To increase backscattering of sound waves in US imaging, solutions containing talcum powder at 4%, 2%, 1%, and 0.5% weight of the base solution were mixed. Other materials such as thin-layer chromatography grade silica gel [115] and cellulose [84], along with enamel paint [111] have also been used as acoustic backscatterers but we found that commercial grade talcum powder also performs well. Each of the samples were immersed in water, imaged, and then visually examined for contrast with the surrounding water and implanted PVA markers spheres.

For increasing phantom contrast in CT imaging, a powdered barium sulphate ($BaSO_4$) preparation used for colon enema (Guerbet Micropaque Colon, Guerbet, Villepinte, Île-de-France, France) was mixed into our PVA solutions. Although $BaSO_4$ at concentrations greater than 60% can drastically alter MR relaxation time, lower concentrations of around 1-8% do not appear to significantly alter MR relaxation times or interfere with image signal [141]. Solutions were prepared with 8%, 6%, 3%, and 1% w/w $BaSO_4$ of the initial base solution.

To enhance the signal in T1 weighted images, copper sulphate ($CuSO_4$) was added to the PVA mixture in small quantities. $CuSO_4$ has been widely used as a MR contrast agent since the late 1970s in phantoms used for MR performance validation such as the recently developed ADNI phantom [93]. Minute quantities of $CuSO_4$ dramatically increase the contrast of the PVA sample in T1 and T2 weighted images. To find an optimal concentration of $CuSO_4$, we prepared 0.2%, 0.1%, 0.05%, and 0.025% (w/w) anhydrous $CuSO_4$ PVA-C samples and imaged them with T1 and T2 imaging sequences.

The appropriate concentrations of talcum, $BaSO_4$, and $CuSO_4$ were determined by choosing the PVA-C samples that had the least amount of contrast agent but still gave qualitatively good MR, CT, and US contrast when the PVA-C samples were imaged when submerged in water in a closed container.

4.2.4 Phantom Construction

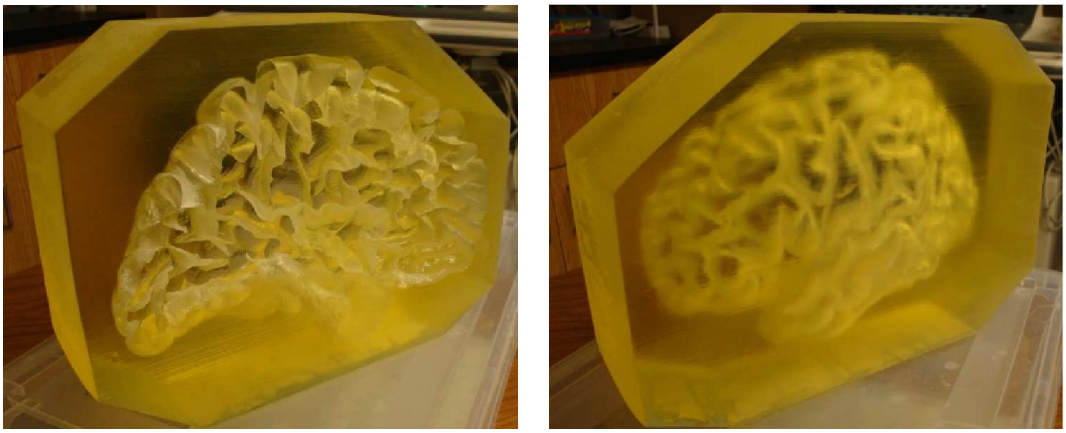

A B

Figure 4–2: Two views of the flexible phantom mold from (A) the inside and (B) the outside.

Brain Mold

The mold for our brain phantom was based on the left hemisphere of the Colin-27 MR data set [103]. The cortical surface of the left hemisphere was segmented using Freesurfer [77] to produce a polygonal surface mesh, which was then processed using the butterfly subdivision module in MeshLab [43] to refine the cortical surface represented by the mesh and also reduce the number of facets in the mesh.

We then subtracted this processed cortical surface mesh from a rectangular prism mesh using the boolean operator in Blender3D (www.blender.org), in order to create

a “negative” of the cortical surface for fabricating our brain mold. After manually correcting the polygonal mesh model for holes, unconnected mesh fragments, and inverse surface normals, the model was then saved in the STL file format, which is commonly used for stereolithographic printing.

We utilized the services of RedEye On Demand (Eden Prairie, MN, USA) for the fabrication of our brain phantom mold using the TangoPlus Polyjet Resin (FC-930) as the material. This clear photopolymer was deposited layer by layer in order to produce a finished three dimensional object (See Fig. 4–2). We found that the mold made using this rubbery material was able to accurately model the sulci and insular region of the cerebral hemisphere while having enough flexibility to allow the PVA-C to be unmolded without damaging the phantom or the mold itself. The mold reverts itself to its original shape when deformed.

The bottom of a plastic tub was cut out and glued around the opening of the flexible rubber mold. This allowed us to cast a base for our phantom when unmolded and also limited its relative movement when placed and imaged in another plastic tub of the same size and format.

The mold component for the left ventricle of the phantom was constructed separately using silicone bathroom caulk. Layers of caulk approximately 2 mm thick were applied to vellum traces from life-size printouts of segmented 2 mm sagittal sections of the left ventricle. These layers were then assembled medially to laterally and aligned using crosshairs on the printout traces to maintain placement accuracy of the sagittal sections and then covered with additional silicone rubber caulk to smooth the mold component surface (See Fig. 4–3).

A B

Figure 4–3: The silicone rubber and cellulose composite mold component used to cast the fluid filled left ventricle in our phantom (A) before and (B) after being covered with additional silicone caulking to smooth the surface.

Implants

To make our phantom useful for tests in image guidance and registration, various structures created from various grades of PVA-C were included into the phantom.

To create spherical registration targets/landmarks, we used a harder PVA-C made from 8% PVA solution that has undergone 2 FTC containing high quantities of contrast agents described in Section II.C for a strong contrast. We found this PVA-C formula to be suitable since it is relatively firm and will not change its shape significantly with phantom deformation. These were molded using the containers for reflective passive spheres used in optical tracking. By using a firmer PVA-C, we limited the amount of distortion that the structure can undergo while enabling the targets to be imaged by US, MR, and CT. These spheres are approximately 11–12 mm in diameter. Together with the phantom cortex landmarks, these internal targets can be used as gold standard markers to verify registration accuracy in the 3

Figure 4–4: The 11–12 mm diameter multimodal spherical markers implanted into our phantom

imaging modalities. (See Fig. 4–4). The spheres can be imaged well with ultrasound since they do not have strong specular reflection due to its similar texture to the surrounding PVA-C tissue. This allowed them to be imaged with relatively even contrast from the edge of the sphere to the center. Furthermore, it prevents the heavy US shadowing of the tissues located "behind" the sphere.

A PVA-C "tumour" was also created using 4% PVA solution with 1 FTC and then embedded into the phantom. The tumour was molded using the ovoid plastic case from inside a Kinder surprise egg (Ferrero, Pino Torinese, Italy). A small hole was drilled on one of the poles of the case to allow for expansion during the FTC. The tumour was then placed in the phantom in order to test guidance accuracy in surgical procedures and also to provide another tissue in the phantom of different texture and contrast.

Phantom Casting

The main brain phantom tissue was cast using the optimal liquid PVA-C identified in the experiments described in Section II.B combined with the contrast agent concentrations selected in Section II.C. The mixture was poured into the brain mold and any air or bubbles trapped in the sulci are removed such that cavities do not form in the sulcal or gyral surfaces of the phantom.

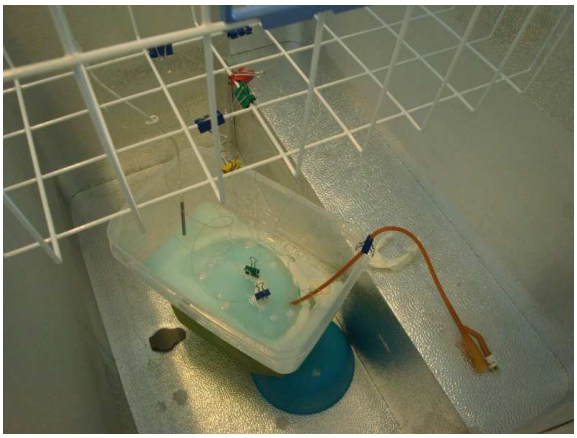

Figure 4–5: The setup for casting the hemispheric portion of the phantom. After the hemispheric part is well frozen, the clamps are removed and PVA solution for casting the base is poured into the mold.

The PVA-C landmark spheres and tumour implants were skewered and suspended using 0.45 mm monofilament fishing lines inside the filled phantom mold at their desired location. The left ventricle mold component was clamped and also suspended with fishing lines in a similar fashion. We found that this technique allowed good positioning of the structures and prevented them from sinking to the bottom of the mold. (See Fig. 4–5).

Finally, we placed the inflatable head of a urinary catheter into the frontal lobe of the phantom and another in the medial portion of the phantom in the cast base of the mold. Each urinary catheter could be inflated with up to 10 millilitres of water using a syringe in the manner described by [199]. This allowed us to vary the extent of deformation on the phantom and conduct experiments on the accuracy of various nonlinear registration algorithms.

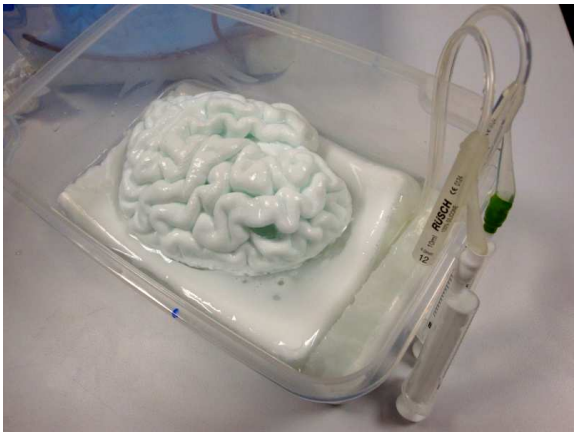

Figure 4–6: The PVA-C phantom cast from our Colin27 based brain phantom mold being prepared for scanning. Note the deep sulci and insular regions of the phantom and the ends of the catheters used to inflate the phantom on the right. For most of our scans, the plastic tub was filled with just enough water to cover the top of the brain phantom.

The entire phantom casting setup was then frozen solid. A thick base for the phantom was cast by pouring an approximately 3 cm thick layer of clear 8% PVA solution over the frozen phantom, which produces a thick layer of PVA-C in the completed phantom of the same thickness. Everything was then allowed to freeze completely and slowed thawed over the course of 48 hours. Once thawed, the brain

phantom readily detaches from the sides of the mold and recovered its original form. An example of the completed phantom can be seen in Fig. 4–6.

4.2.5 Imaging

Modalities and Parameters

Our triple modality imaging includes acquisition of phantom images in MR, CT, and US. All our MR images were acquired on a Siemens Verio 3T MR scanner (Siemens Healthcare, Erlangen, Germany) using the imaging parameters listed in Table 4–1.

Table 4–1: The MR modalities used to image the phantom with deformation and their imaging parameters. The modalities used are: T1-weighted spin-echo (T1-SE), T1-weighted gradient-echo (T1-GE), T2-weighted gradient-echo (T2-GE), proton density (PD), fluid attenuated inversion recovery (FLAIR), and diffusion weighted imaging (DWI). The sequences each have their own repetition times (TR) and echo times (TE), as well as an additional inversion time (TI) for FLAIR imaging. Following the acquisition of the DWI 30 directions, the fractional anisotropy (FA), apparent diffusion coefficient (ADC), and trace weighted images (TWI) were computed.

MR Modality	**TR**	**TE**	**Flip Angle**	**Voxel size**
T1-SE	668 ms	8.9 ms	70°	1×1×3 mm^3
T1-GE	1900 ms	3 ms	9°	1 mm^3 isotropic
T2-GE	6530 ms	840 ms	150°	1×1×3 mm^3
PD	6530 ms	9.4 ms	150°	1×1×3 mm^3
FLAIR (TI=1800 ms)	5000 ms	273 ms	120°	1 mm^3 isotropic
DWI	9300 ms	94 ms	90°	1×1×2 mm^3

CT images of the phantom were acquired for the phantom in 491 axial slices at 1.25 mm thickness using a GE LightSpeed 16 VCT scanner (GE Healthcare, Little Chalfont, Buckinghamshire, UK).

US images were acquired with a Sonosite 180 Plus (Sonosite, Bothell, WA, USA) diagnostic ultrasound system tracked using a Medtronic Stealth neurosurgical

station (Medtronic, Minneapolis, MN, USA). Images for the phantom were acquired as a series of tracked B-mode US images of 44 images in 4-6 sweeps at either 5.2 cm or 7.1 cm depth.

Table 4–2: The inflation volumes on Catheter 1 and 2 used to deform the brain phantom on the 5 multimodality imaging series.

Series	Catheter 1	Catheter 2
1	0 ml	0 ml
2	5 ml	0 ml
3	5 ml	5 ml
4	5 ml	10 ml
5	10 ml	10 ml

Acquisition Methodology

The images of the deformed phantom were acquired in the following manner. A series of images were first acquired for each of the CT, US, multiple MR modalities mentioned. After the image acquisition, the phantom was deformed and then a series of acquisitions with the same imaging parameters was repeated. Deformation is done by inflating each of the two implanted urinary catheters in the phantom (See Fig. 4–6) with 0 ml, 5 ml or 10 ml of water through 5 rounds of inflations in the manner described in Table 4–2. For each given amount of deformation, the phantom was scanned in all the modalities without changing the inflation of the catheters. This ensures that exactly the same physical deformations was scanned in each modality. It is only after the whole series of the multimodal images were acquired for a deformation, that the catheter inflations were changed.

Images for testing super-resolution image processing and scan-rescan reliability testing, were acquired by scanning the phantom without catheter inflation using MP-RAGE T1 weighted gradient echo sequence (TR=1900 ms, TE=3 ms, Flip Angle=9°, 1 mm isotropic). This acquisition was repeated 10 times with water and 10 times without water. Each of these scans were acquired at an isotropic resolution of 0.5 mm, with the phantom displaced slightly (<1 cm) between each of the acquisitions.

Post-Processing

Following the data acquisition, the US images were reconstructed into an US volume using distance weighted interpolation and denoised using the nonlocal means method described in [54]. Transformation from the tracked US probe given by the neuronavigation system were used to reslice all the MR and CT volumes to match each reconstructed 3D US volume.

The MR T1 and T2 times of tissues in our phantom were determined using software available from our institute.

4.3 Results

Table 4–3: PVA sample texture ratings for similarity to live human cerebral tissue by the neurosurgeon who specializes in neurovascular surgery with 21 years experience The samples were rated from 0 to 10 with the former being dissimilar to brain tissue and the latter being exactly like brain tissue. The star (*) indicates a sample that the surgeon believed felt like a low grade gliomas.

	4% PVA	5% PVA	6% PVA	8% PVA
1 FTC	0	4	7	4 *
2 FTC	8	5	0	0
3 FTC	6 *	0	0	0

4.3.1 PVA-C Formula Choice

Based on the neurosurgeon's PVA-C scoring (See Table 4–3), we selected two samples for further analysis:

- 6% PVA with 1 FTC
- 4% PVA with 2 FTC

We found that a large quantity of the contrast agents tended to settle to the bottom of the large brain mold while freezing the 4% PVA mixture. We therefore choose to build the normal brain phantom tissue with 6% PVA with 1 FTC. The low-grade glioma tissue was made using 4% PVA with 3 FTCs, as it was determined to be the best representative sample by the surgeon. In order to further justify our choice for the PVA-C formula used for the normal phantom tissue, a PVA-C sample of 6% PVA 1 FTC was submitted for rheological testing on a 3369 Dual Column system (Instron, Norwood, MA, USA). While only one PVA-C sample was tested, we found that the Young's modulus for the sample was 4.6kPa$\pm$0.5%, which is in the range of Young's modulus measured for human brain. [165]

4.3.2 Triple Modality Contrast

We used the 6% 1 FTC PVA-C formula as the base material to test different concentrations of $BaSO_4$, $CuSO_4$, and talcum powder contrast agent. These different PVA-C samples were then scanned using MR, CT, and US imaging. We found that for the phantom brain tissue, concentrations of 2% $BaSO_4$, 0.025% $CuSO_4$, and 1% talcum as contrast agents worked well for CT, MR, and US, respectively. Through only palpation tests done by the neurosurgeon and the authors, we determined that

the texture of the PVA-C did not change perceivably with the addition of these quantities of contrast agents.

For our triple modality image markers, we found that 5% $BaSO_4$, 0.2% $CuSO_4$, and 5% talcum as contrast agents in 8% PVA with 2 FTC provided adequate contrast for CT, MR, and US, respectively. These contrast concentrations were chosen to provide the markers with sufficient contrast from the surrounding normal tissue PVA-C as to be easily visible on the images of each modality.

4.3.3 Imaging results

A sample of the multimodal images and the result of the inflations can be seen in Figs. 4–7 and 4–8, respectively.

The MR and CT Images aligned and resliced to the US using tracking information given by the neuronavigation system can be seen in Figs. 4–9-I and II, respectively. The corresponding 2D US image can be seen in Fig. 4–9-III.

The MR T1 and T2 times of tissues in our phantom were determined using software available from our institute. T1 and T2 times for the phantom tissue were 1004-1213 ms and 163-182 ms, respectively, while T1 and T2 times for the casted tumour were 1900-2600 ms and 1100-1665 ms respectively.

4.4 Discussion

4.4.1 Image Processing Validation

We believe that the acquired multimodal images with different deformations can be used for validation of many image processing techniques such as segmentation,

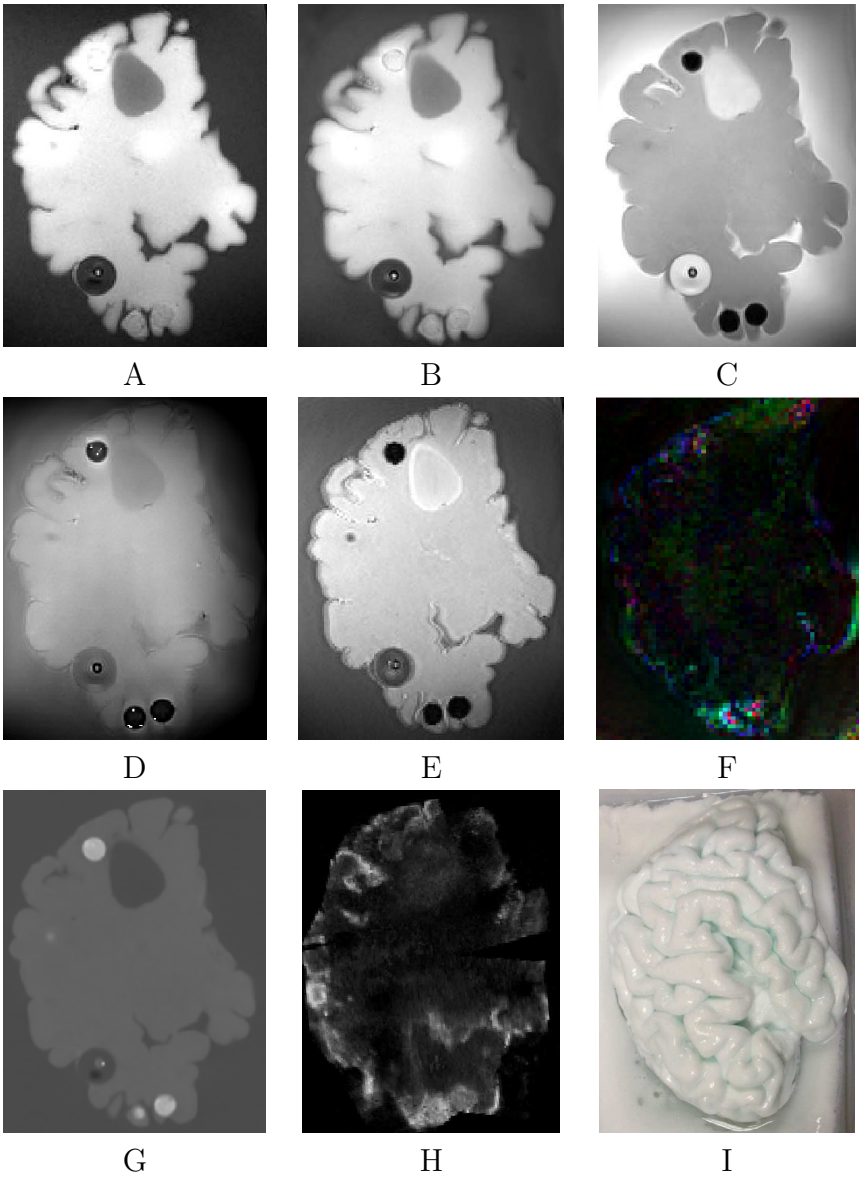

Figure 4–7: A selection of PVA-C brain phantom images acquired using MR T1-weighted gradient-echo(A), MR T1-weighted spin-echo (B), MR T2-weighted (C), MR PD (D), MR FLAIR (E), MR DTI colour map (F), CT (G), a reconstructed US image (H), and a picture of the PVA-C Phantom (I).

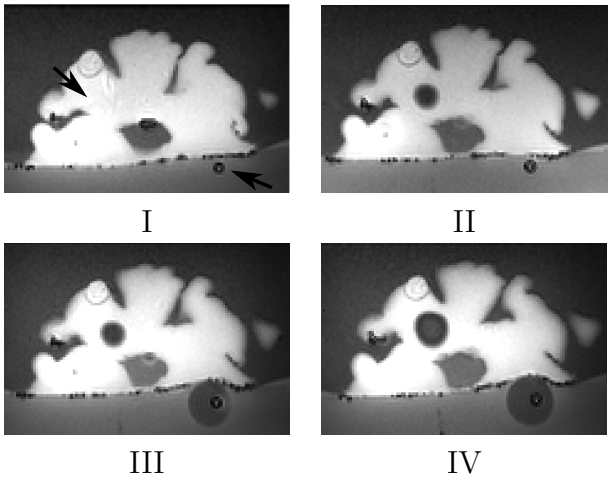

Figure 4–8: Images I–IV shows the same coronal slice of the phantom imaged with T1-weighted gradient-echo at different inflations (Series 1, 2, 3, and 5, of Table 4–2, respectively). The arrows in Image I show the location of the catheters in that slice of the phantom.

image reconstruction, linear or nonlinear registration, and denoising algorithms, using images acquired from one modality to act as the ground truth of another. The deformation images can also be used to validate physical simulation.

As well, the multiple displacement MR images can be used to validate the accuracy of super-resolution algorithm, which can use the information from image redundancies and sub-pixel shifts in low resolution images to recreate a higher resolution image of the original imaged object. Further information on super-resolution methods can be found in [150].

In addition, the phantom may be used for testing and training of stereotatic procedures. such as biopsy needle insertions or deep-brain stimulator placement. Together with the phantom's accurate gross cortical anatomy, its similarity to the

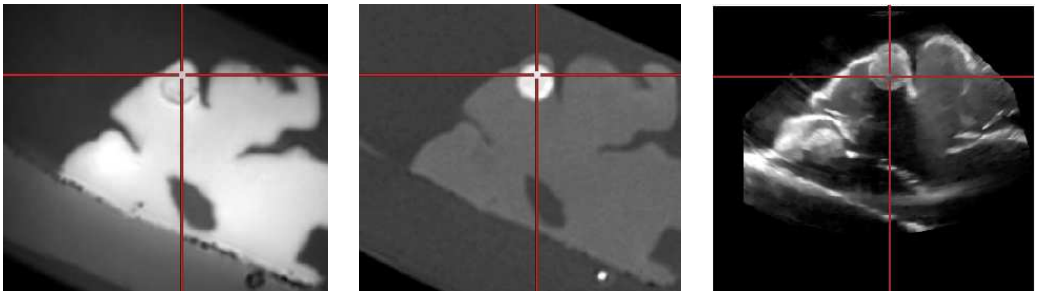

I II III

Figure 4–9: Images I–III show a cropped section of the phantom MR and CT images aligned with the US image.

texture of live brain, and its low cost, the phantom can be useful educational tool in training medical professionals.

4.4.2 Limitations and Future Work

There are several limitations in the current phantom that could be addressed in future work. Notably, our method for selecting the PVA solution concentration and the number of FTCs relies on a subjective assessment. A better approach may be to measure the rheological characteristics of live human brain tissue using MR or US elastography or through direct intraoperative mechanical characterization, and use these results to guide the choice of PVA concentration and number of FTCs. This would allow for the ability to select the PVA concentration and FTC as a function of the desired physical and imaging properties of the material. Experiments quantifying the rheological properties of human brain will have to account for the physiological state of the individual patient since different factors such as blood pressure, the administration of pharmaceuticals (e.g. mannitol), or other physiological conditions [253] can dramatically change the rheological properties of the human brain.

Nevertheless, the concentration and number of freeze-thaw cycles chosen in this study resulted in a texture that was qualitatively comparable to live brain tissue when palpated by an experienced neurosurgeon. Moreover, the phantom created here had rheological characteristics that were similar to those found in the literature in terms of Young's modulus for live human brain and it deforms more realistically than previously proposed deformable brain phantoms in the literature.

The phantom proposed in this study could also be improved by devising a method of simulating heterogeneous tissue, since the current version only allows for homogeneous simulated tissue with discrete punctate insertions. Doing this would make it possible to simulate different brain tissues (e.g. white matter, cortical grey matter, deep grey matter). More sophisticated phantom casting techniques would also make it possible to simulate white matter tracts and blood vessels.

Finally, it was found that over time the $CuSO_4$ MR contrast agents tended to diffuse or leak from the landmark spheres into the surrounding tissue. This difficulty could be resolved either by sealing the landmark spheres to eliminate leaking, or find MR contrast agents that will not diffuse out of the spheres.

4.5 Conclusion

We have presented a method for creating an anthropomorphic human brain phantom that is anatomically and mechanically realistic, which can also be effectively imaged in the multiple modalities of MR, CT, and US imaging.

We have also made all the images acquired from the phantom publicly available to the larger image processing community at: `http://pvabrain.inria.fr`. The

phantom and data will enable validation of image processing methods and facilitate the development of new interventional methods.

4.6 Acknowledgments

We would like to thank the Neurinfo platform team for its financial support and their assistance in processing and acquiring the MR data, as well as Professor Olivier Le Guillou and Florence Le Dret at the chemistry department of the Institut National des Sciences Appliquées (INSA) de Rennes for allowing us to use their equipment for preparing solutions. We are also grateful to the Fonds québécois de la recherche sur la nature et les technologies (FQRNT) and the Collège Doctoral International (CDI) de l'Université européenne de Bretagne (UEB) Bourse de Mobilité Internationale Entrante for funding this project.

CHAPTER 5
Enhancement of Vascular Structures in Medical Images

Forward

Our work in vessel-based intraoperative registration in Chapter 3 also demonstrated the need for an improved vessel enhancement algorithm that can more effectively suppress the non-vessel background paranchymal tissues while enhancing dim vessel structures from angiographic images. By having a better vessel enhancement algorithm, we could also potentially improve the performance of vessel-based registration methods or data preprocessing for other angiographic image processing techniques such as vessel structure extraction. Finally, these enhanced images can be used directly in the clinical setting to aid surgical planning and navigation in IGNS.

In this chapter, we present a novel modification of an existing technique for the enhancement of vessel structures in angiographic medical images. Our enhancement analyzes a larger image region surrounding a pixel or voxel to better identify whether it is actually part of a vessel structure in comparison to techniques which use only local support information from the image Hessian. We present our modifications to the the popular vessel enhancement filter of Frangi *et al.* [81], based on Hessian eigenvalue analysis, by replacing its simple background suppression term ("structureness term") with a more sophisticated term that accounts for a voxel's participation in vessel like features in a larger neighbourhood region. The analysis

of the larger pixel or voxel region is done by using the non-local means (NLM) estimator of Buades et al. [25], which identifies image voxels in a neighbourhood that have similar local patches to a certain voxel. By performing image shape analysis on the NLM generated weightmap, a pixel or voxel can be identified as either belonging or not belonging to a vessel structure.

To show that our method is general enough to work on 2D and 3D images and for angiographies of different imaging modalities, we validated our technique on clinical 2D retinal angiographic images, synthetic 3D helical spiral images, and clinical 3D phase-contrast MRA images. We found that by using our structureness term based on analysis of the NLM weightmap, we could significantly improve the original method's ability to identify lower contrast and thinner vessel structures while better suppressing non-vessel background structures. Tests were also performed to find the theoretical best result for structureness substitution techniques such as our NLM enhancement technique.

This chapter has been submitted to *International Journal of Computer Assisted Radiology and Surgery*.

- S. J-S. Chen, P. Coupé, and D. L. Collins. Blood Vessel Enhancement Through Principal Component Analysis of Non-local Means Weightmaps *International Journal of Computer Assisted Radiology and Surgery*, Nov 14 2013, Submission Number:JCARS-D-13-00259

Manuscript: Blood Vessel Enhancement Through Principal Component Analysis of Non-local Means Weightmaps

Sean Jy-Shyang Chen [1], Pierrick Coupé [2], D. Louis Collins [1]

[1] McConnell Brain Imaging Centre, Montreal Neurological Institute, McGill University, Montreal, Canada
[2] CNRS, UMR 5800, Université Bordeaux, 33405 Talence Cedex, France

Abstract

Purpose: Frangi's vesselness filter is one of the most commonly used vessel enhancement methods in medical image processing and many modifications have been proposed to improve it. We wanted to determine if the *structureness* term in the original technique limits vessel detection and whether replacing it by another term can produce improvements.

Methods: We propose substituting it with one based on analysis of non-local means (NLM) weightmaps using principal component analysis. Our method was validated using synthetic 3D spiral images, 3D clinical magnetic resonance angiographic images, and 2D clinical retinal angiographic images.

Results: Our novel structureness term can identify greater regional vessel features that may be suppressed by Frangi's method due to low image Hessian eigenvalues. Substitution of the original structureness term with our NLM-based term improves vessel enhancement and suppression of background in our validation tests.

Conclusions: These experiments revealed that replacing the structureness term with our NLM structureness term can improve the performance of the original method and allow it to enhance and retain more thin and low contrast vessels.

5.1 Introduction

Angiographic images are highly important in surgical navigation and for the clinical diagnosis of diseases. To improve the quality and contrast of the vessels in these images, vessel enhancement methods are typically used for image preprocessing. There are vast numbers of work in the literature regarding vessel segmentation and enhancement methods, with many of them based on Hessian eigenvalue analysis. The process involves finding the images' Hessian eigenvalues at various scales and analyzing them to determine whether a voxel contains the image characteristics of a vascular structure [81, 143, 216].

One of the most commonly used method of this class is that of Frangi et al. [81], which enhances voxels with eigenvalues ratios conforming to the tubular shape of vessel. The eigenvalues of bright vessels in dark backgrounds (dark-field) are ordered such that $\lambda_1 \leq \lambda_2 \leq \lambda_3$ while dark vessels in bright backgrounds (bright-field) are ordered $\lambda_1 \geq \lambda_2 \geq \lambda_3$. The method analyzes the eigenvalues at multiple scales (s) through 3D vesselness filtering defined for dark-field images as:

$$V(s) = \begin{cases} 0 & \text{if } \lambda_2 > 0 \text{ or } \lambda_3 > 0 \\ (1 - \exp\big(-\frac{R_A^2}{2\alpha^2}\big)) \exp\big(-\frac{R_B^2}{2\beta^2}\big) (1 - \exp\big(-\frac{S^2}{2c^2}\big)) & \text{otherwise} \end{cases} \tag{5.1}$$

where $R_A = |\lambda_2|/|\lambda_3|$ in the first term assures that that the vessel cross-section is relatively circular ("circularity"), $R_B = |\lambda_1|/\sqrt{|\lambda_2\lambda_3|}$ in the second term assures that vessel is more elongated in one axis ("blobness") and $S = \sqrt{\lambda_1^2 + \lambda_2^2 + \lambda_3^2}$ in the third term weighs the intensity of all the eigenvalues making sure that only pixels with higher eigenvalues are enhanced ("structureness"). The α, β, and c terms are set

to 0.5, 0.5, and $0.5max(S)$, respectively, as per the recommendations in [81]. This function effectively enhances dark-field vessel lumen structures that have eigenvalue relationships $|\lambda_1| \approx 0 \ll |\lambda_2| \approx |\lambda_3|$. To adapt Eq. 5.1 for enhancing light-field vessel structures, the vesselness should instead be 0 if $\lambda_2 < 0$ or $\lambda_3 < 0$. The 2D version of the algorithm retains only the latter two terms and is defined for dark-field images as:

$$V(s) = \begin{cases} 0 & \text{if } \lambda_2 > 0 \\ \exp\big(-\frac{R_B^2}{2\beta^2}\big)\,(1 - \exp\big(-\frac{S^2}{2c^2}\big)) & \text{otherwise} \end{cases} \tag{5.2}$$

To adapt eq. 5.2 for enhancing 2D light-field vessel structures, the vesselness should instead be 0 if $\lambda_2 < 0$.

Integration of vesselness filtering at all performed scales is done by:

$$V(\gamma) = \max_{s_{min} \leq s \leq s_{max}} V(s, \gamma) \tag{5.3}$$

where s_{min} and s_{max} are the minimum and maximum scales where at which the vesselness filtering through Eq. 5.1 is performed. Eq. 5.1, 5.2, and 5.3 effectively define Frangi's multiscale vesselness method and were published by Frangi et al. [81].

Although it is effective at enhancing higher contrast and relatively large diameter vessels, Frangi's filter and similar methods employing Hessian eigenvalue ratio analysis do not effectively enhance vessel structures that are low in contrast intensity, thin, and embedded in a noisy background. These vessels may have diameters smaller than the voxel size and would be missed by larger filter scales but also difficult to differentiate from noise when analyzed locally at a smaller scale. Vessel features that

are relatively small to the filter scale, lower in local signal-to-noise ratio (SNR), and have lower regional contrast may not be optimally enhanced with Frangi's filter.

Indeed, the final second order "structureness" parameter in Frangi's vesselness is essentially the Hessian Frobenium norm. Thus, if a voxel's norm is low, it will be suppressed as noise, regardless of whether the voxel is part of a larger discernible regional structure. Therefore, performing eigenvalue analysis-based vascular filter on low SNR data at the minimal scales often results in poorly enhanced or broken vessel segments and much lower responses at vascular bifurcations [153].

Even with these issues, vessel enhancement based on Hessian eigenvalues are used extensively as an initial preprocessing method in many vessel segmentation methods [34, 152, 64, 269]. The vesselness maps are even used as the actual vessel image in various end applications, such as in image registration techniques [202, 91, 39].

There have been several works in the literature that sought to overcome the issues arising from local intensity dependant Hessian based vesselness measures. For instance, methods of Canero and Radeva [34] and Manniesing et al. [153] used diffusion tensors constructed from the Hessian eigenvalues and eigenvectors to enhance and smooth-out the intensities of the vessel segments filtered using Frangi's vesselness measure. Shikata et al. [226] had redefined a Hessian based vesselness filter that is resilient to fluctuations of the eigenvalues in the principle orientation of the vessel axes by incorporating information from gradient features in a larger neighbourhood region. Tankyevych *et al.* [242] proposed a morphological operators-based diffusion scheme, using Hessian eigenvalues to isolate linear vessel segments and apply

structuring elements guided by the orientation of the principle Hessian eigenvectors. More recently, Yuan et al. [269] proposed the use of local line integrals to average the image Hessian eigenvalue values along the Hessian eigenvector principal axis of a vessel segment to provide smoothness to the measured vesselness map.

These methods are important contributions for the effective segmentation of smooth vessel structures and their bifurcations. However, we wanted to see if we could improve Frangi's method by making adjustments to the original method. In this case we have chosen to look more closely at the "second order structureness" term of the method. Depending on how this term was tuned, the method will either be unable to enhance vessels with lower intensities or SNR, or be unable to differentiate actual vascular structures and artifacts caused by background noise. One reason may be that the assumption that the foreground and background can be distinguished based primarily on highly local information from the Hessian, which is computed from a relatively small image region. In low contrast to noise (CNR) image regions, local information alone may not be sufficient to determine whether a voxel is part of a thin or low contrast vessel.

In this work, we wish to characterize Frangi's filter output to evaluate if its Hessian norm structureness term is limiting the enhancement of vessels, and if so can this be resolved through the substitution of another term. Therefore, we propose to replace Frangi's structureness term with a term that evaluates information from larger regional features. We believe that when this information is analyzed, it can help better determine whether a voxel indeed participates in a vessel-like structure. We believe that by modifying the structureness term to account for larger regional

image features, we should subsequently improve Frangi's vesselness measure in its ability to enhance dim and thinner vessel features while suppressing background noise.

5.1.1 Non-Local Means Weightmap

To determine a voxel's participation in larger regional structure, we used the non-local means (NLM) algorithm first introduced by Buades et al. [25]. In its original form, it was used to identify redundant information in an image for the purpose of noise removal. The algorithm restores $u(x)$, the intensity of a voxel of interest x, by finding the weighted average of the voxels x' in the surrounding image region Ω with a size $(2M+1)^3$ for a 3D data set, where M is the radius of region Ω.

$$NLM(u(x)) = \hat{v}(x) = \frac{\sum_{x' \in \Omega} w(x,x')u(x')}{\sum_{x' \in \Omega} w(x,x')} \tag{5.4}$$

The $NLM(u(x))$ is the estimated value $\hat{v}(x)$ of the original value $v(x)$, where $u(x)$ is the noised corrupted value, $u(x) = v(x) + noise$. The method works through weighting of the intensity $u(x')$ using the function $w(x,x')$, where local neighbourhood patch $P(x)$ of x was compared to that of local patch at $P(x')$. In 3D, each patch can be set to a size of $(2d+1)^3$ surrounding the central voxel, where d is the radius of each patch. We maintain $d < M$ such that each patch used in NLM analysis is smaller than the region where the patch centre voxel exists. The comparison to determine similarity between x and x', is done through finding the average Euclidean distance $\| - \|_2$ between two local patches and weighting by the function:

$$w(x,x') = e^{-\frac{\|P(x)-P(x')\|_2}{h^2}} \tag{5.5}$$

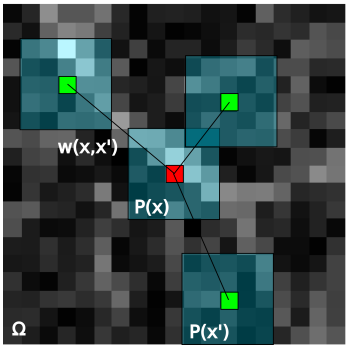

Figure 5–1: A 2D illustration of how the NLM algorithm functions. The local "patch" (in blue overlay) of the red central voxel ($P(x)$) is compared against the local patches of each green central voxels ($P(x')$) in the surrounding region Ω. The resulting pairwise comparisons with generates the weightmap ($w(x, x')$) for voxel x.

where h is the parameter for tuning the filtering bandwidth which is set to $h = \sqrt{min(\|P(x) - P(x')\|_2)}$. By weighting each $x' \epsilon \Omega$ by $w(x, x')$ (See Fig. 5–1) we can generate a NLM weightmap uniquely for the region around x (See Fig. 5–2b).

Although initially used for image denoising, the NLM algorithm has since been used for other image processing methods including super-resolution [150] and image segmentation [53]. Here, we process the weightmap directly as its own image to determine whether x is part of larger structural features in the image (See Fig. 5–2). When the local neighbourhoods of each patch are measured for similarities and mapped, similar voxels in the larger region are enhanced and can then themselves be analyzed to determine their contribution to regional "structureness" in the larger image sub-region. (See Fig. 5–2b).

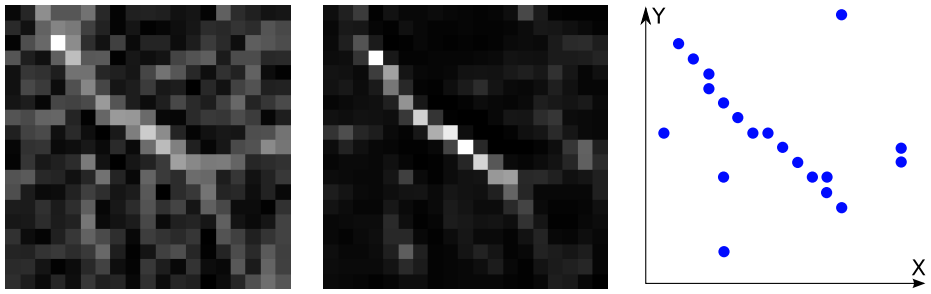

(a) (b) (c)

Figure 5–2: A region surrounding a central pixel (a) and the resulting weightmap produced through the NLM algorithm (b). Note that the pixels with similar local patches are assigned higher values on the weightmap. The voxel coordinates of weightmap voxels greater than a weightmap mean-based threshold were used to construct a point set for PCA (c).

5.1.2 Contributions

In this work we developed a modification to Frangi's vesselness measure, by replacing the method's locally based structureness map with our alternate NLM-based structureness map. We also found the best possible results for this type of substitution method, to have a basis of which to compare our methods results above that of Frangi's method.

5.2 Methods

We propose a modification to Frangi's vesselness measure, by replacing the locally based structureness map with an alternate NLM-based structureness map created from Frangi's structureness map. This structureness map can identify lower contrast but large non-local vessel features in the image. Our method creates the NLM weightmap unique to each image voxel then processes each weightmap using principal component analysis (PCA), resulting in a set of principal eigenvalues that were processed similarly to the circularity and blobness terms in Frangi's algorithm

(See Eq. 5.1). Analyzing the larger NLM weightmap allows us to determine if a current voxel is part of a low CNR elongated structure in the image, something which cannot be determined simply by analyzing small-scaled Hessian with small local kernel support. The strategy of incorporating information from the larger image region to improve Hessian-based vesselness enhancement has been explicitly used by Shikata et al. [226] using the larger regional gradient features around a pixel of interest and by Yuan et al. [269] using the larger region pixels' Hessian along an oriented line from a pixel of interest. Here, we use the NLM technique to identify similar pixels in a larger neighbourhood to detect larger vessel structures.

We account for the fact that a voxel that is part of a longer tubular structure with a certain orientation, as determined by the larger neighbourhood NLM weightmap, should have a similar orientation to that detected from Hessian eigendecomposition, which uses a smaller local support. By comparing the geometric form and structure orientation from both the larger neighbourhood and smaller local support, we can determine if a voxel should be considered part of a vessel. The workflow for our method can be seen in Fig. 5–3.

To begin the processing, the raw image was initially processed at the smallest scale to find its Hessian eigenvalues and eigenvectors. The Hessian eigenvalues were used for Frangi's eigenvalue analysis, calculating the geometric circularity and blobness terms as well as Frangi's structureness term, which we use as a starting image generating the NLM structureness. The eigenvector of the vessel orientation from Hessian analysis (Θ_{Frangi}) was retained for a later phase in our analysis. Both

Frangi's structureness and the orientation Θ_{Frangi} are used for our NLM processing (See. Fig. 5–3)

The NLM algorithm was used to process Frangi's structureness to generate a set of weightmaps. The NLM method of Buades et al. [25] was applied with the region radius set to $M = 5$ and the patch radius for 2D images set to $d = 2$ and 3D images set to $d = 1$. We found that larger patch radii lowered the sensitivity of NLM to voxels in thinner vascular structures. Region radii that were too small can cause our method be more sensitive to noise in the background, while larger region radii tended to include voxels from nearby vessel structures, which can cause the method to not identify a vessel structure correctly. We found through our trials that the described parameters work sufficiently well to balance vessel enhancement with background suppression.

The values of each generated weightmap were intensity normalized to values between 0–1 as suggested by Coupé et al. [53]. The point coordinates of all weightmap voxels with values greater than 2 standard deviations from the mean value of the weightmap were used (See Fig. 5–2c). The point-set derived from high value weightmap voxels have high self-similarity to the central voxel and analyzing them can reveal the shape of the feature in which the central voxel participates. Although it was possible to run PCA directly on the weightmap, from our experience we found that thresholding provided a point-set that greatly improved vessel structure identification. This may be because our threshold discards noise and values that do not contain relevant structural information. This point-set was processed with PCA to acquire a set of eigenvectors and eigenvalues describing the shape of the point-set.

Table 5–1: Structural features detected in 2D and 3D depending on the magnitude of the PCA derived NLM eigenvalues $\lambda_{k_{nlm}}$ (H=high, L=low), which are ordered such that $\lambda_{1_{nlm}} \geq \lambda_{2_{nlm}} \geq \lambda_{3_{nlm}}$. All eigenvalues from PCA are positive.

Structural features	2D		3D		
	$\lambda_{1_{nlm}}$	$\lambda_{2_{nlm}}$	$\lambda_{1_{nlm}}$	$\lambda_{2_{nlm}}$	$\lambda_{3_{nlm}}$
Small blob-like structure	L	L	L	L	L
Line-like structure	H	L	H	L	L
Plane-like structure	-	-	H	H	L
Large blob-like structure	H	H	H	H	H

The eigenvalues from the NLM weightmaps, which we will now refer to as "NLM eigenvalues", were sorted from the largest to the smallest such that $\lambda_{k_{nlm}}$ represents the eigenvalue with the *k-th* smallest magnitude, where in a 3D image $|\lambda_{1_{nlm}}| \geq |\lambda_{2_{nlm}}| \geq |\lambda_{3_{nlm}}|$. The principle NLM weightmap derived PCA eigenvector Θ_{nlm}, which corresponds to $\lambda_{1_{nlm}}$, was recorded since it is the principle direction of the structure in the NLM weightmap image. Different relations in magnitude between the NLM eigenvalues allows for the detection of different structural features (See Table 5–1). Inspired by the filter strategy of Frangi, we seek out eigenvalue relations where $\lambda_{1_{nlm}} \gg \lambda_{2_{nlm}} \approx \lambda_{3_{nlm}}$ to find voxels with regional structure conforming to elongated structural features using:

$$S_r = \exp\Big(- \frac{\sqrt{\lambda_{2_{nlm}} \lambda_{3_{nlm}}}}{\lambda_{1_{nlm}} \beta_{nlm}} \Big) \tag{5.6}$$

which is similar to Frangi's "blobness" term, and determines whether the structure is elongated more on one one axis in relation to its cross-section, which was controlled in the equation using β_{nlm}. This rough NLM map can be seen in Fig. 5–3a.

Voxels that participate in long structures were well identified by Eq. 5.6, however background noise may sometimes also be misidentified as tubular structures.

Additional filtering is performed through the analysis of the principle eigenvectors from Hessian analysis and NLM weightmap PCA. A voxel with an orientation from its larger NLM weightmap should be similar to its orientation from the smaller-support local Hessian analysis. Voxels with different orientations between its longer structures and small features are less likely to contain vessel structures. Curved vessels will change the mean in PCA but maintain the same principle orientation. To achieve this, we added a third term to Eq. 5.6 that performs eigenvector analysis by finding the absolute value of the dot-product of the principle eigenvectors from Hessian analysis (Θ_{Frangi}) and NLM weightmap PCA (Θ_{nlm}). This term was tuned with value c_{nlm} such that orientations similar to one another are given a weight closer to 1. This orientation similarity map can be seen in Fig. 5–3d. Although this term may mistakenly identify short and noisy tubular structures as noise, we find that the vessel filtering was improved with the term. The NLM weightmap terms of each voxel were then multiplied and their values added to produce the output, which gives us Eq. 5.7:

$$S_r = \underbrace{\exp\Big(-\frac{\sqrt{\lambda_{2_{nlm}}\lambda_{3_{nlm}}}}{\lambda_{1_{nlm}}\beta_{nlm}}\Big)}_{\text{NLM elongation}} \underbrace{\exp\Big(-\frac{|\langle\Theta_{Frangi},\Theta_{nlm}\rangle|}{c_{nlm}}\Big)}_{\text{Orientation similarity}} \tag{5.7}$$

The S_r value of each voxel was then multiplied with the voxel's NLM weightmaps then added to a blank image. Essentially, this operation distributes the S_r value at voxel to all voxels that contribute to its participating structure in the image; effectively increasing the intensity values of voxels that participate in a larger elongated vessel structures and decreasing the intensities of those that do not. This intensity map was then normalized with an intensity map created simply through the addition of

voxel NLM weightmaps to produce the NLM structureness map. This operation is defined as:

$$S_{nlm}(j) = \frac{\sum_i W_i(j) S_r(i)}{\sum_i W_i(j)} \tag{5.8}$$

where i and j are voxel coordinates of the input and output image, respectively, W_i is an image of the same size as S_r containing non-zero NLM weightmap values in a region radius centred at i. Thus, the value at voxel j of the output image $S_{nlm}(j)$ is the weighted means of all the values at voxels i in the input image $S_r(i)$, where the weights come from the voxel at coordinate j of each NLM weightmap generated for voxel i ($W_i(j)$).

This structureness map may contain discontinuities in areas of sharp vessel bends and bifurcations, which needs to be regularized and smoothed prior to being used. Although, the NLM method is able to find similar voxels in lower vessel curvatures, the method will not find long vessels structures in areas with sharper bends or bifurcations, thus resulting in "enhancement gaps" in the structureness map. We found that these gaps are small enough that with anisotropic blurring the surrounding high NLM structureness values will cover over these discontinuities. This allows disconnected segments caused by sharp vessel curvature or bifurcations to be smoothed and joined together, thus creating a regularized map which can be used to correctly mask out non-vessel structures. This oriented anisotropic blurring was accomplished by using the PCA eigenvectors and S_{nlm} to control the orientation and shape of a Gaussian blurring kernel. This is done by creating a co-variance transformation matrix, $A = V\Lambda V^{-1}$ from a 3×3 square matrix V formed from the set of PCA eigenvectors v_1, v_2, v_3 arranged in columns such that $V = [v_1 v_2 v_3]$ and a 3×3 diagonal matrix

Λ whose diagonal elements have the values $\lambda_1 = S_{nlm}$, and $\lambda_2 = \lambda_3 = 1/r$, where r is the radius of the kernel support. The transformed Gaussian blurring kernel processed from each voxel is then multiplied by S_{nlm} and added to a blank image and its intensity range normalized to between 0 and 1. This produces our smoothed "NLM structureness" map S_{Snlm} as seen in Fig. 5–3e.

We substitute Frangi's second-order structureness term in Eq. 5.1 with our smoothed NLM structureness term S_{Snlm}:

$$V(s_{min}) = \begin{cases} 0 & \text{if } \lambda_2 > 0 \text{ or } \lambda_3 > 0 \\ \underbrace{(1 - \exp\big(-\frac{R_A^2}{2\alpha^2}\big))}_{\text{Frangi's circularity}} \underbrace{\exp\big(-\frac{R_B^2}{2\beta^2}\big)}_{\text{Frangi's blobness}} \underbrace{\exp(-S_{Snlm})}_{\text{NLM structureness}} & \text{otherwise} \end{cases} \tag{5.9}$$

where all terms of the equation corresponds exactly to Eq. 5.1 except Frangi's second-order structureness term $(1 - \exp\big(-\frac{-S^2}{2c^2}\big))$ is replaced by our NLM PCA structureness term S_{Snlm}. Although our methods can be used to replace the Frangi vesselness filter at each scale by increasing the patch size d, we find that our method complemented Frangi's filter quite well when applied solely at the minimal filter scale $V(s_{min})$. This is because there is often significant noise present at the smaller scales that hide the thin and low contrast vessel structures then at the larger filter scales. We apply our NLM structureness only to the smallest scale filters in our test.

Our algorithm was completely implemented in Matlab (2012a, The MathWorks, Natick, Massachusetts, U.S.A.) with the algorithm for NLM weightmap processing implemented as a C++ MEX-file.

5.3 Experiments

In order to compare our proposed NLM vessel enhancement algorithm against Frangi's vessel enhancement algorithm, we performed a set of quantitative tests. First, we characterized the algorithm through quantitative testing of the two algorithms on synthetic vessel images with different levels of contrast and noise. We then tested the algorithm on real clinical 2D retinal and 3D MR data.

We also tested our method against a publicly available ITK implementation of the anisotropic diffusion vessel enhancement filter [72] of Manniesing et al. [153] on our 3D MR data. This filter modified upon Frangi's vesselness and incorporates diffusion, which is similar to oriented blurring used by our method.

5.3.1 Purpose

The purpose of the experiments is to determine the efficacy of our method on smaller diameter and lower contrast vessels. In medical angiographic images, the smallest vessels that can be imaged is relative to the size of the image voxel, the contrast between the vessel structure and its background, and any image noise present. In this paper, we refer to vessel structures in the image that have diameters of one or less one voxel as "small" or "thin vessels", and vessels that have less than 50% contrast in respect to its regional background as "low contrast vessels".

5.3.2 Parameters

Similar to the parameters of Frangi's vesselness filter method (Eq. 5.1) described in Section 5.1, we set our parameters of the modified vesselness filter Eq. 5.9 were set to $\alpha = 0.5$, $\beta = 0.5$ and $c = 0.5max(S)$, where $max(S)$ was calculated for each filter scale. For the parameters in our NLM structureness term, we set the parameters to

$\beta_{nlm} = 0.12$ and $c_{nlm} = 0.1$, which we found to produce good structureness maps though our own experimentation.

The sigmas of 2, 1.5, 1, 0.5 pixels were chosen for 2D retinal angiographic image test and 2, 1.5, 0.8 voxels for the 3D MRA image test. These sigmas scales were chosen since their full-width-half-max (FWHM $= 2\sqrt{2\ln\sigma}$) approximately match the voxel (or pixel) radii of the vessel in the image being processed. Through our preliminary tests, we found that using 4 filter scales for the retinal angiographic images produced qualitatively better results than using less than this number of filter scales, while 3 filter scales were used for the 3D images for the same reason. For our images, using more filter scales did not appear to improve the filtering and increased processing time. The smallest scale sigmas for 2D angiographic and 3D MRA images were set to 0.5 pixel and 0.8 voxel, respectively. Although some of the sigmas are less than the voxel size, we find that the slight smoothing provided by Gaussian kernels at these sigmas help regularize the background while retaining these smaller vessels.

For the anisotropic diffusion vessel enhancement of Manniesing [153], we specified the same range between 0.8 and 2 sigmas at 3 scales with 12 rounds of vessel diffusion. We did not have direct control of the which sigmas were used and found that the implementation generated sigmas of 2, 1.3, and 0.8. These value are similar to our 3D MRA tests sigmas of 2, 1.5, and 0.8. We chose the 12 rounds of diffusion since it smooths vessels without appearing to remove the finer vessels in our MRA image. The values for sensitivity (S), w-strength (w), and epsilon (ϵ), were left at

the default values of 4, 24, 0.01, respectively. We refer the reader to [153] for detailed information regarding these parameters.

5.3.3 Validation data

We evaluated our NLM vessel enhancement method on three different data sets: a set of 3D synthetic spiral data, a set of 2D clinical retinal angiography data, and a set of 3D clinical MRA data.

To compare our NLM enhancement against other methods, we ran our method against images from the DRIVE retinal image database of Staal et al. [235], which have publicly available results of other methods that also ran on this database. This is a good comparison since, these methods have been tuned by their developers. A comparison of our NLM vessel enhancement method against other technique can be found in Section 5.4.2. All experiments were performed on a Intel Core2 Quad CPU Q6600 2.40GHz machine.

Synthetic spiral data

We created a set of synthetic spiral images of varying image noise and contrast with either (1) the same image contrast but at different regional noise levels and (2) the same noise level but at different regional contrasts. These tests allowed us to characterize the performance of our vessel enhancement method on images with multiple noise or contrast levels. For such images, it is not possible to simply find a global threshold to isolate the vessel structures from the image background since both noise and contrast alters the intensity of the Hessian norm.

The images were created by combining five $100 \times 100 \times 100$ voxels images containing a 1 voxel diameter spiralling conical helix curve decreasing in curve diameter with

each turn. Each of these spiral images were generated by tracing a partial volume conical helix into a 100×100×100 isotropic volume using a curve to voxel distance based spatial domain antialiasing method similar to [263]. The intensities of the image were then normalized to $[0, 1]$ and used as the ground truth helical vessel. Each spiral image was than combined with 5 different structure to background contrasts at $10, 20, 40, 80, 100\%$ and 5 different Gaussian noise levels with $\infty, 1, 0.5, 0.2, 0.1$ SNR to produce 25 images with all possible permutations of contrast and noise. The contrast level was defined as $(I_v - I_b)/I_b)$, where I_v is the intensity of the spiral vessel and I_b is the mean background value.

The final synthetic spiral images were made by concatenating together 5 of aforementioned 100×100×100 images of the same noise or contrast levels, thus creating multiple 100×100×500 images. Four sets of spiral images with 5 varying contrast and 5 varying noise levels were generated for our tests, giving us a total of 40 spiral test images. These generated test synthetic spiral image volumes can been seen in Fig. 5–4, which consist of a "stack" of 5 different concatenated 100×100×100 spiral images.

Clinical retinal angiography data

We used the twenty 2D retinal angiographic blood vessel data sets and ground-truths from the DRIVE retinal image database of Staal et al. [235]. The images were captured digitally using a Canon CR5 nonmydriatic 3CCD camera at 45° field of view. The images are 768×584 pixels, 8 bits colour channel with a 540 pixel diameter field of view. The 20 ground truth images were segmented by two observers by labelling image pixels when they were at least "70% certain" that the pixels were

vessel structures. The database is commonly used for validation and comparison of general vessel enhancement algorithms. For more details on the test database, we refer the reader to Staal et al.[235].

Clinical MRA data

We used the twenty real clinical 3D phase-contrast MRA (PC MRA) images from Aubert-Broche et al. [11, 10] as test images. Vessel bronze standard images were created through manual segmentation by the first author to label the visible blood vessels in each of the twenty PC MRA images as described below.

Our strategy for creating higher quality bronze standards involved manually segmenting the MRA at the original resolution, and then resampling them to the lower resolution of the test images. Using the original high resolution images for labelling allowed us to confidently identify large and high contrast vessel structures, thus producing higher quality bronze standard images. Our test images were generated by resampling the original higher resolution image to half its resolution. These lower resolution test images have smaller and lower contrast vessels that have been confidently identified in the bronze standard. Using these bronze standards and test images allows us to better evaluate the efficacy of our vessel enhancement methods.

The following is the detail of how the processing for the test images of bronze standard images were performed:

1. The *clinical PC MRA test images* of 20 young normal subjects were originally acquired at 384×512×176 voxels, with voxel dimensions of 0.47×0.47×0.9 mm at TR=71 ms, TE=8.2 ms, angle=15 °. The images were linearly registered to the International Consortium for Brain Mapping average brain space

(ICBM)[74] and were then resampled with linear interpolation to 181×217×181 1mm^3 voxels to make the voxels isotropic and reduce the image resolution. The images were then masked to remove all non-brain tissue using an implementation of the brain extraction algorithm of Smith [232]. These images were used as the test images for our vessel enhancement validation.

2. The *bronze standard segmentations* of the 20 PC MRA images were generated by first linearly registering and resampling the original 384×512×176 anisotropic voxel image to ICBM stereotaxic space at 362×434×362 isotropic voxels and manually labelling them with voxels of label values $\{0.0, 1.0\}$. We then convolved these manually segmented images with a 3D isotropic Gaussian kernel of $\sigma = 1$ voxel. This is similar to Gaussian spatial pre-filtering used in anti-aliasing to smooth and assign partial volumes to a structure's voxel surroundings [58]. The images were then down-sampled to half the resolution with trilinear interpolation to create our 181×217×181 1mm isotropic bronze standard clinical vessel images. In relabelling two of the MRA images, we calculated a Dice's kappa of 0.77 for intrarater variability, which is comparable to that reported for the retinal database [235].

5.3.4 Evaluation metrics

3D data

In our 3D synthetic spiral and clinical MRA data, both our ground truth images and filter output consisted of continuous-valued labels. In order to accurately measure the differences between two partial volume label classes (either vessel or background) we used the Generalized Tanimoto Coefficient fractional differences measure

by Crum et al. [55] defined as:

$$\mathrm{GTC} = \frac{\sum_i \mathrm{MIN}(A_i, B_i)}{\sum_i \mathrm{MAX}(A_i, B_i)}$$

where GTC is the General Tanimoto Coefficient defined for continuous label values, and A_i and B_i for each voxel i and where $A_i, B_i \in [0, 1]$.

We validated our technique on the 3D synthetic spiral and clinical PD MRA data by measuring the GTC metric from the NLM filter and Frangi filter for each of the test images.

The GTC metric measures the absolute intensity differences between test and bronze standard images. Therefore, unlike a binary measure such as Dice's Kappa, which measures the proportion of overlap in discrete label class, slight differences in intensities would be reflected in a lower GTC scores. We take advantage of this aspect of the GTC measure since it allows us to measure how effectively a method enhances a vessel structure, and how closely this enhancement approaches intensities of the ground truth labels. This is particularly important for comparing blood vessels with small diameters in relation to the image's resolution or voxel size, which often have much lower enhancement intensities than the same vessels manually identified in a ground truth.

2D data

Since our NLM and Frangi's vessel enhancement method operates on grey-scale images, we first convert the RGB colour retinal angiography images to grey-scale by applying the luminosity-based digital colour to grey-scale conversion standards the International Telecommunications Union [107]. This standard conversion

scheme is based on the coefficients for human perception of colour, and converts the red (R), green (G), and blue (B) components of the images to grey-scale (V) by: $\mathrm{V} = 0.21R + 0.72G + 0.07B$. The resulting grey-scale image were then used in our 2D validation tests. While some groups used only the green component in their test, luminosity colour desaturation incorporates information from all three colour channels in a manner similar to the human eye, which we believe should be used for proper image analysis.

For all our clinical 2D retinal angiographic test sets, we evaluate our enhancement algorithm also using GTC metric as with the case of our 3D tests. Since the provided ground truths were labelled with discrete binary values we calculated the receiver operating characteristic (ROC) curve by varying the threshold on the filter output images. By taking the area under the curve (AUC) of the ROC curve, we were thus able to compare our NLM enhancement method against other published vessel enhancement methods.

On top of our tests between Frangi's original method and our NLM modified enhancement method, we also attempted to find the best possible theoretical result (ROC, AUC, and GTC) for our type of class of technique. Namely, what are the best results obtainable for Frangi's method if we had the optimal structureness term, while keeping the first two geometric terms the same. To achieve this we replaced the structureness term with the ground truth, which provided us the best possible results for second-order structureness replacement techniques.

5.4 Results

5.4.1 Synthetic spiral data

In the our helical spiral image tests, the NLM filter had a mean GTC of 0.136 versus 0.07 with Frangi's filter in noise varied images and a mean GTC differences of 0.24 versus 0.10 for contrast varied images. The mean percent improvements of the NLM filter over Frangi's filter were 93% and 234% for noise and contrast varied images, respectively. The p-values from the paired t-tests for our 40 test images for noise and contrast were 2.12×10^{-3} and 1.52×10^{-4} indicating a significant improvement of the NLM method in vessel enhancement. The enhancement results for the noise and contrast images can be seen in Fig. 5–5 and Fig 5–6.

We found that the NLM filter performed significantly better than Frangi's filter at all contrast varied images. Frangi's filter monotonically improved in performance with the increase of image contrast (See Fig. 5–6). On images with varied noise levels, the NLM filter also performs significantly better than Frangi's filter. Both Frangi's and the NLM filter decreases monotonically in performance with an increase in noise, but both relatively insensitive to noise except NLM at at infinite SNR. In fact, the NLM filter experiences a sharper decrease in performance when there is noise in the image compared to the noiseless image ($SNR = \infty$). This can be seen in Fig 5–5 when the SNR is ∞ versus at 1.0, 0.5, 0.2, or 0.1.

5.4.2 Clinical retinal angiography data

Measuring our results in GTC, our NLM vesselness filter was able to enhance at worse 24% more and at best 77% more of the retinal vessels compared to Frangi's

filter (See Table 5–2). From these tests, the NLM filter yields mean enhancement improvement of 41% over Frangi's filter.

Through our tests, we saw that Frangi's enhancement method is limited by the structureness term. If the structureness does not highlight a vessel due to low Hessian eigenvalues then it will not be properly enhanced. As such, replacing the structureness term with the ground truth, enables us to see how well the first two terms enhance vessels and what is the best possible enhancement of a structureness replacement enhancement method such as ours. The mean GTC for Frangi's results, our NLM results, and the best possible structureness replacement filter is 0.13, 0.22, and 0.30, respectively. The mean performance of NLM filter was 73% of the best possible replacement filter versus Frangi's filter which 43%. The reason why on 73% is because (1) we could not get ALL the fine vessels in the ground truth and (2) some of the detected Hessian features were actually not vessels but other structures.

We calculated the ROC curves and the AUC of our NLM vesselness filter technique to that of Frangi's filter and found the mean AUC of all 20 retinal angiography images to be 0.83 ± 0.025 and 0.78 ± 0.022 for NLM and Frangi's filter, respectively. The AUC and standard deviation for the best possible structureness replacement result is 0.89 and 0.020, respectively. These AUC values and their standard deviations are reported in Table 5–3 along with the reported AUC of other published retinal angiography vessel enhancement methods.

The average ROC curves for NLM, Frangi, and the best for structureness replacement can be seen in Fig. 5–7. It should be noted that the ROC curve for the best result, exceeded the sensitivity and specificity of a human observer since the

Table 5–2: GTC results of the clinical retinal angiography data on Frangi's filter and our NLM vessel enhancement filter on MR angiography images of 20 subjects. The GTC between each subject's manually segmented vessel ground truth image and the compared techniques (Frangi and NLM) are shown and well as the percentage (% Improvement) of vessels enhanced by NLM above Frangi's algorithm. The GTC of the best possible structureness replacement type filter (Best) and the percentage of our NLM GTC to Best GTC (NLM % Best) are also shown.

Subjects	1	2	3	4	5	6	7	8	9	10
Frangi	0.19	0.18	0.07	0.13	0.15	0.03	0.15	0.09	0.05	0.18
NLM	0.30	0.27	0.18	0.22	0.20	0.14	0.21	0.20	0.14	0.24
% Improvement	37%	33%	62%	41%	27%	77%	31%	57%	61%	25%
NLM % Best	78%	80%	80%	70%	74%	68%	69%	78%	70%	72%
Best	0.38	0.33	0.22	0.32	0.27	0.21	0.31	0.26	0.20	0.34

Subjects	11	12	13	14	15	16	17	18	19	20
Frangi	0.23	0.12	0.13	0.10	0.28	0.14	0.04	0.10	0.11	0.12
NLM	0.30	0.19	0.20	0.23	0.35	0.22	0.16	0.17	0.23	0.20
% Improvement	24%	39%	38%	58%	19%	37%	76%	42%	53%	42%
NLM % Best	70%	69%	68%	76%	71%	70%	73%	67%	72%	67%
Best	0.42	0.28	0.30	0.30	0.49	0.31	0.22	0.26	0.32	0.30

human observer specificity is determined through a separate set of manual segmentations by a different human observer. In our best enhancement, we used the same manual ground truth as the structureness replacement thus exceeding the results of a human observer results.

Sample results from the retinal angiography clinical tests can be seen in Fig. 5–8 and Fig. 5–9. In Fig. 5–8, note that Frangi's filter, using only the Hessian norm as "structureness measure", identifies more background artifacts as vessels, while the NLM filter has better background suppression while still enhancing relatively dim vessels (See Fig. 5–8h and 5–8i). As well, as expected, the best result reveals the finest vessels that are not enhanced by the NLM and Frangi's methods (See Fig. 5–8g). The close ups and effect of adjusting thresholds on the filter results can be seen in Fig. 5–9.

Table 5–3: Average AUC (AUC Mean) and standard deviation (AUC SD) for images from the DRIVE database for Frangi's filter (Frangi), the NLM filter (NLM), the best possible result for second-order structureness replacement (Best), and the published results from other retinal vessel enhancement methods.

	AUC Mean	AUC SD
Frangi	0.784	0.0291
NLM	0.832	0.0255
Best	0.891	0.0202
Jiang[113]	0.911	-
Staal[235]	0.952	-
Zana[270]	0.898	-
Chauduri[36]	0.788	-

Processing each retinal image on our Matlab-based NLM enhancement implementation takes approximately 10 minutes, compared with around 1 minute required by Frangi's method.

5.4.3 Clinical MRA data

In our clinical 3D MRA data tests, we found that the proposed NLM vesselness filter was able to effectively suppress the background structures while preserving the lower contrast and thinner vessel structures. The NLM vesselness filter at was able to enhance vessel structures 36–44% more effectively than Frangi's algorithm (See Table 5–4). From these tests with the 20 real clinical images, we saw a mean enhancement improvement of 39% by the NLM filter over Frangi's filter with a t-test p-value of 7.15×10^{-21} and a mean enhancement improvement of 36% by the NLM filter over the anisotropic vessel enhancement diffusion filter with a t-test p-value of 7.01×10^{-15} (See Fig. 5–10). Example results from the clinical MRA tests can be seen in Fig. 5–11, Fig. 5–12, and Fig. 5–13.

We found that Frangi's method did not effectively enhance many of the thinner and lower contrast vessels compared to the bronze standard. Although, the

Table 5–4: Results of standard Frangi and our NLM vessel enhancement algorithm on MR angiography images of 20 subjects. The results are shown as the GTC [55] between each subject's manually segmented vessel bronze standard image and Frangi the Anisotropic Vessel Enhancement Diffusion (Aniso) and NLM. The percentage of vessel enhanced by NLM above Frangi's ($\%_F$) and the Aniso filter ($\%_A$) results are also shown.

Subjects	1	2	3	4	5	6	7	8	9	10
Frangi	0.12	0.11	0.12	0.12	0.11	0.11	0.11	0.13	0.11	0.12
Aniso	0.14	0.11	0.12	0.12	0.12	0.13	0.14	0.13	0.13	0.12
NLM	0.22	0.19	0.19	0.20	0.19	0.18	0.18	0.21	0.19	0.18
$\%_F$	44%	42%	39%	38%	40%	40%	39%	37%	40%	36%
$\%_A$	37%	42%	40%	40%	35%	27%	26%	38%	31%	33
Subjects	11	12	13	14	15	16	17	18	19	20
Frangi	0.12	0.12	0.11	0.12	0.11	0.12	0.11	0.11	0.13	0.13
Aniso	0.12	0.14	0.12	0.12	0.11	0.14	0.13	0.10	0.13	0.15
NLM	0.20	0.19	0.19	0.20	0.18	0.19	0.18	0.19	0.21	0.21
$\%_F$	42%	37%	42%	42%	37%	36%	36%	42%	36%	40%
$\%_A$	40%	29%	35%	40%	41%	28%	28%	50%	41%	29

anisotropic vessel enhancement diffusion filter enhances more of these lower contrast vessel though the oriented diffusion, we found that it also enhanced artifacts and noise from the raw MRA data sets (see Fig. 5–11). We also found that the NLM enhancement method was able to suppress much of the noise and artifacts. Although the NLM filter enhanced specks of noise that do not appear to be vessel structures, it also enhanced many low contrast vessels that were not identified in the bronze standard.

We see that Frangi's structureness term itself removes the thinner and lower intensity vessels with the default c=0.5×max(S), but tuning this parameter to be more sensitive resulted in enhanced background artifacts in addition to the extra vessels (see Fig. 5–12). When c was set to the default value, Frangi's vessel enhancement algorithm fails to enhance the fine and low contrast vessels (see Fig. 5–12 "c=0.5"),

however the NLM filter is able to enhance these vessels while suppressing the background. When c is tuned to c=0.01×max(S) large amounts of the background structures are enhanced along with the vessels (see Fig. 5–12 "c=0.01"). Note however, the NLM method does misidentify vessels as seen in some of the disconnected specks. Frangi's structureness, unlike our NLM structureness term, suppresses background noise based only on the eigenvalue magnitudes and does not explicitly account for whether a voxel is part of a strong and elongated region structure (see Fig. 5–13).

Processing each 181×217×181 MRA image on our Matlab-based implementation takes approximately 46 minutes. The less computationally intensive Frangi's vesselness method takes approximately 2 minutes on the same machine.

5.5 Discussion and Conclusion

Background structures arising from image noise or textures of the paranchymal tissue, which are caused by their enhancement through Frangi's geometric ratio terms (circularity and blobness), must be removed before the filtered vessel image can be properly interpreted. While the Hessian norm structureness measure used by Frangi's original algorithm removes these background structures quite effectively, it also suppresses large amounts of vessels correctly highlighted by the geometric terms. For instance, entire vascular branches may be eliminated due to image noise, vessel thinness, or their relatively low contrast with the background.

In this work, we have shown that:

1. In examining a voxel in context to a greater image region, we can better determine a voxel's participation in angiographic vessel structures angiographic.

2. Improving structureness at the lowest scale of Frangi's method can significantly improve the original algorithm.
3. The NLM weightmap can reveal structural features in a image that may be used in subsequent image processing steps.

Our NLM structureness-replacement based filter effectively suppressed background artifacts while preserving thinner and lower contrast vessels in comparison to Frangi. By using PCA to analyze the NLM weightmap, we can perform geometric shape analysis to identify whether a voxel is part of a larger vessel structure. This prevents lower intensity vessel structures from being suppressed due to its low Hessian norm, which is determined only through local convolution (Fig. 5–13). By detecting and taking into account the structures in a large region, our method can improve vessel enhancement by preserving vessels suppressed by the original structureness term while properly suppressing background noise and artifacts. This is important since a voxel's participation in fine or dim vessel structures can be better determined by analyzing a larger region than that covered by the image Hessian. Through our NLM structureness filter, even larger vessel structures that were dimly enhanced at the smallest filter scales were also correctly identified as vessel structures and enhanced (Fig. 5–13). Comparisons to our manually labelled bronze standards also showed that the method was able to identify vessels that were not seen by the manual labeller. (Fig. 5–11)

From our results, we can see that the NLM method improves upon Frangi by providing a more effective structureness term. However, we also saw that improving the structureness term alone cannot conclusively resolve the issues of enhancing

thin and low-contrast vessel. In this case, our NLM method still under-enhances many vessels. Even the *best* structureness term, which uses the ground truth as structureness, cannot optimally enhance all the thinner vessel structures (Fig. 5–9). Indeed, we see this through the low GTC values throughout our tests. The sensitivity of the GTC measure to intensity differences allows us to see that the filter output intensities of our methods and even that using the best structureness term is still far from the optimum intensities of the manually labelled standards. This leads us to conclude that perhaps the formulation of the Frangi's first two filter terms are also not ideal and could be improved through future work.

This may also be why our method and even our ground-truth based *best* structureness term, did not perform better compared to some existing techniques that are not based on Hessian eigenvalue ratio analysis. Rather these techniques used either 0th-order information [270, 113], or applying feature detection on regions around minima ridges [235]. We believe that these methods either use information that is less susceptible to noise (0th-order data) or take advantage of different image information not used in our methods, such as vessel centerline approximating ridges. This indicates that additional topological and non-derived raw image data may be essential for better vessel enhancement, and incorporating them may help improve our vessel enhancement method for retinal images.

It should be noted that we are not proposing a method that completely replaces Frangi's filter. For the most part, the original filter is quite effective in geometrically identifying vessel-like structures using Hessian eigenvalue ratios alone, especially in

structures of higher contrasts and larger image scales. However, dim and thin vessels that are less visible will likely be suppressed by the original structureness term.

For our future work we intend to further improve upon our method using NLM weightmaps or exploring the possibility of using other self-similarity based techniques. Other types of image data, such as the original image data, gradient information, and topological data such as vessel centerlines can also be integrated into the NLM weightmap analysis to improve vessel enhancement. Our proposed method illustrates how the NLM weightmap can be used for vessels feature identification. We believe that further exploration of the feature enhancement characteristics of NLM weightmap may reveal other applications in image analysis. The speed of the algorithm can also be greatly improve by optimizing the code or reimplementing it in a lower level language such as C or C++.

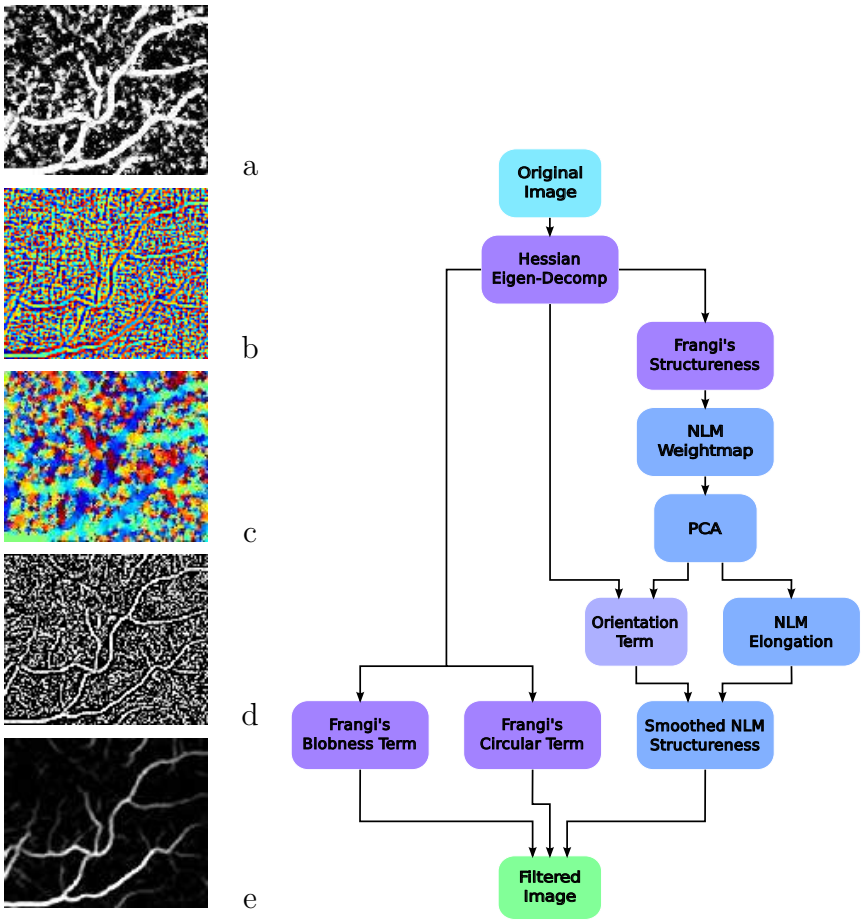

Figure 5–3: The workflow for the modified vesselness measure using NLM structureness and the intermediate maps used for processing. The *Original image* was processed through *Hessian Eigen-Decomposition* to get the Hessian eigenvalues, which was used to calculate *Frangi's Structureness* as the raw image to calculate the *NLM weightmaps*. Each voxel's NLM weightmap is then processed using *PCA* to find the "NLM eigenvalues" for filtering using Equation (5.6) giving us a *NLM elongation* map (a). *Hessian Eigen-Decomposition* and *NLM weightmaps PCA* also give us their principle orientations (b and c; $-\frac{\pi}{2}$ to $\frac{\pi}{2}$ with the spectral colours of red to blue, respectively.), and comparing them gives us the *orientation similarity* map (d). The combined *NLM elongation* and *orientation similarity* map is then processed through anisotropic blurring guided by the principle NLM eigenvector to smooth over discontinuities in the image. This produces our *Smoothed NLM Structureness* term (e) that is combined with *Frangi's circular and blobness terms* (see Equation 5.9) to produce the *Filtered image*.

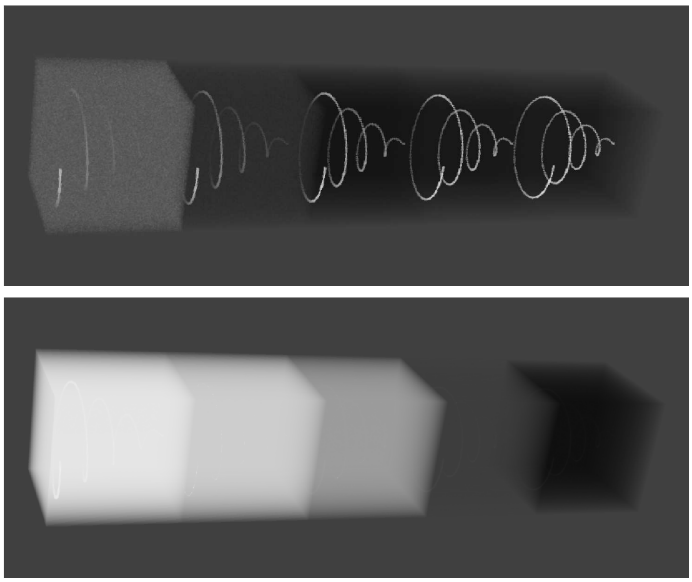

Figure 5–4: A synthetic spiral image with all five noise levels at 100% contrast (top) and a contrast varied spiral image with all five contrasts and ∞ SNR (bottom) visualized in oblique view using 3D ray-casted volume rendering. The transfer function used in visualizing the noise varied spiral image had been adjusted to clearly show the noise. The noise varied images have different noise levels in each part of the image while the contrast are kept the same. Contrast varied images have different contrast levels in each part of the image while the noise levels are kept the same. This allows us to evaluate how a vessel enhancement algorithm performs on images with different noise or contrast levels.

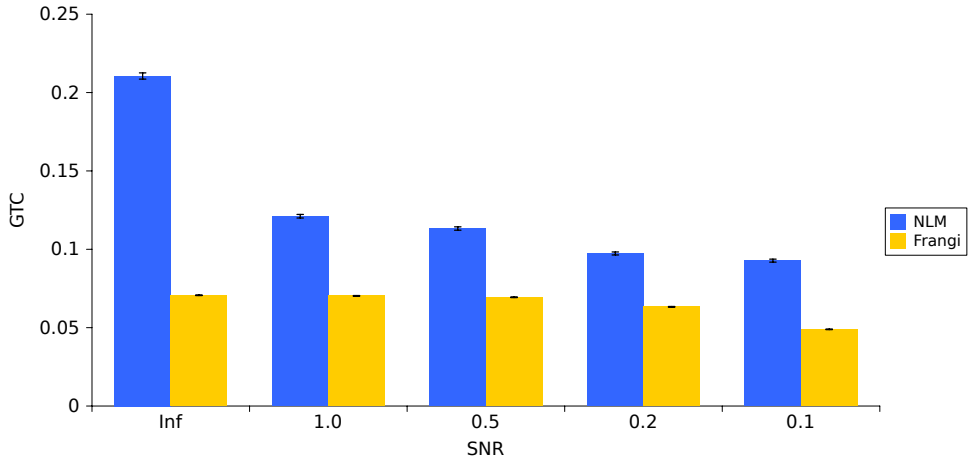

Figure 5–5: Enhancement results on the noise varied synthetic helical vessel images for the NLM filter compared with Frangi's filter. The error bars indicate one standard deviation for each tests at each noise level. The mean improvement of the NLM filter over Frangi's filter is 93%.

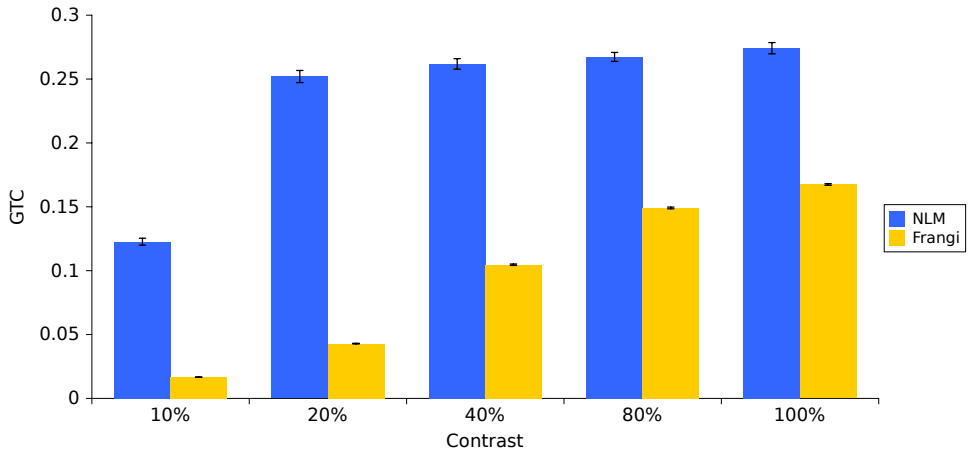

Figure 5–6: Enhancement results on the contrast varied synthetic helical vessel images for the NLM filter compared with Frangi's filter. The error bars indicate one standard deviation for each tests at each contrast level. The mean improvement of the NLM filter over Frangi's filter is 234%.

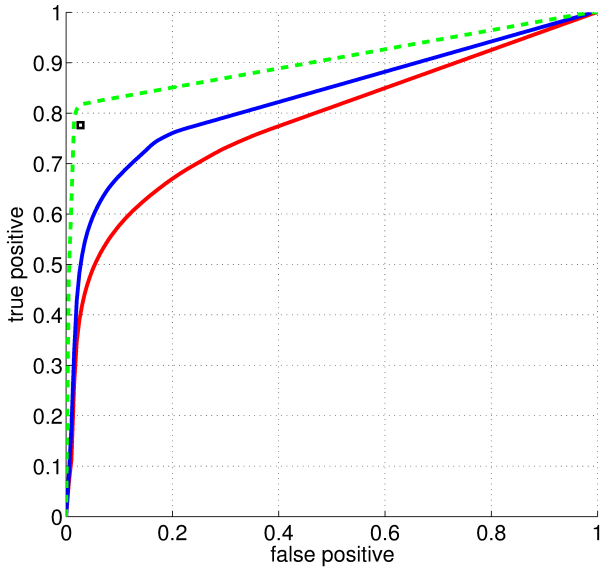

Figure 5–7: Average ROC curves for the results of the NLM filter (blue), Frangi's filter (red) and the best possible result (green) for the test images from the DRIVE database, generated by varying the threshold of the filter results from its minimum to maximum value. The black box indicates the sensitivity (true positive) and the specificity (1-false positive) of a human observer in [235].

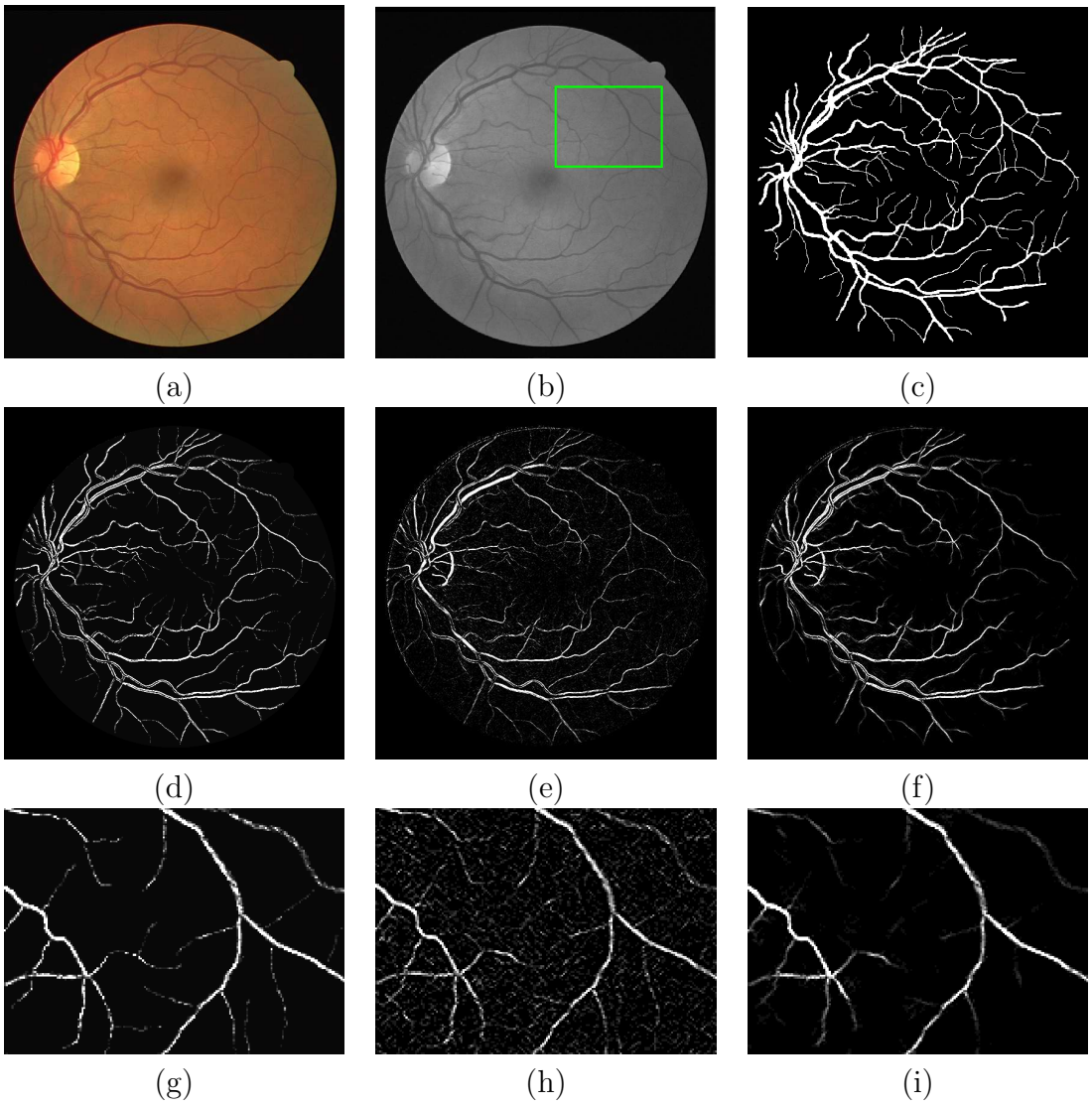

Figure 5–8: An example vessel enhancement result from the DRIVE retinal angiography database [235], with the original image (a), the desaturated image (b), and the provided segmentation ground truth (c), The best possible enhancement result (d), the result from Frangi's method (e), and the results from NLM modified filter (f) are shown next to their respective close-up in (g), (h), and (i), with the area of close-up from the green box in (b).

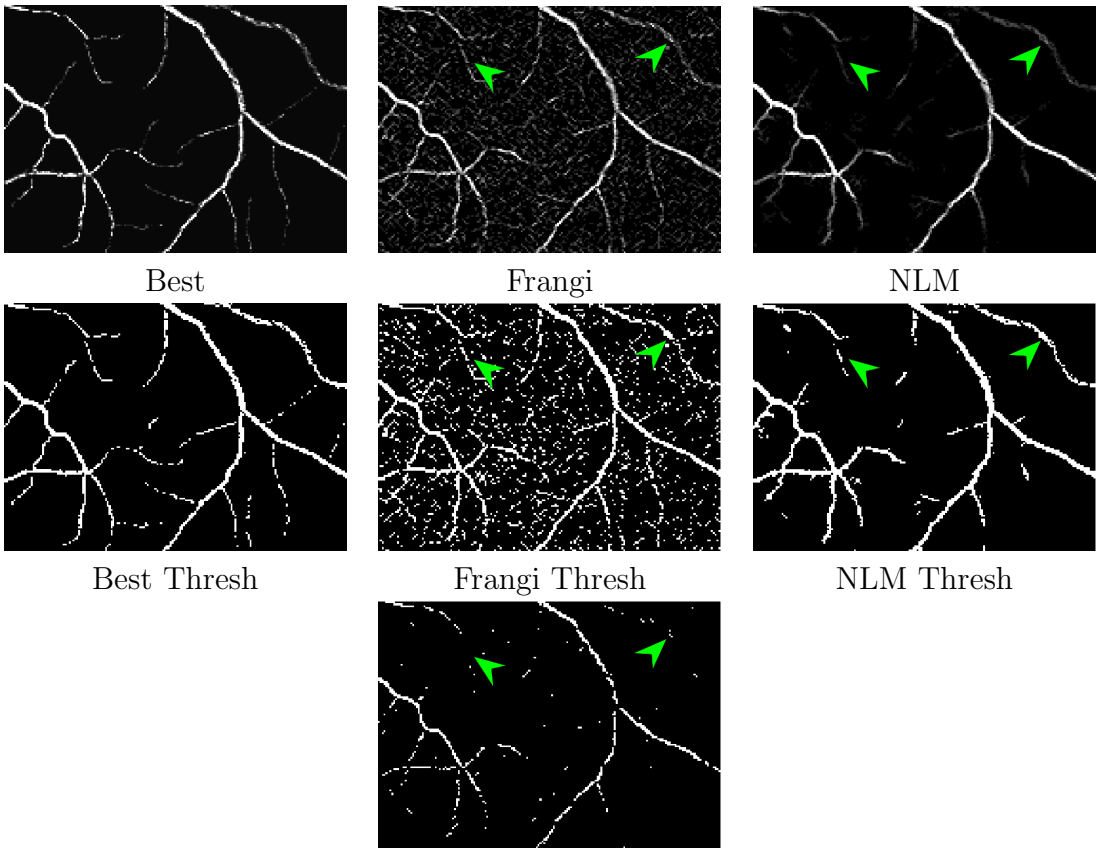

Figure 5–9: Close-ups of an example vessel enhancement results from the DRIVE retinal angiography database [235] Showing the histogram matched best possible filter result (Best), Frangi's vesselness filter result (Frangi), and our NLM modified filter (NLM). When the above images were thresholded to an intensity value corresponding to Frangi's result at 95% specificity, we get (Best Thresh), (Frangi Thresh), and (NLM Thresh). The green arrows show dim vessels structures that were well enhanced by the NLM method. In (Frangi High Thresh), we see Frangi's result thresholded at 99.5% specificity, which reduces background artifacts but also the dimmer vessels.

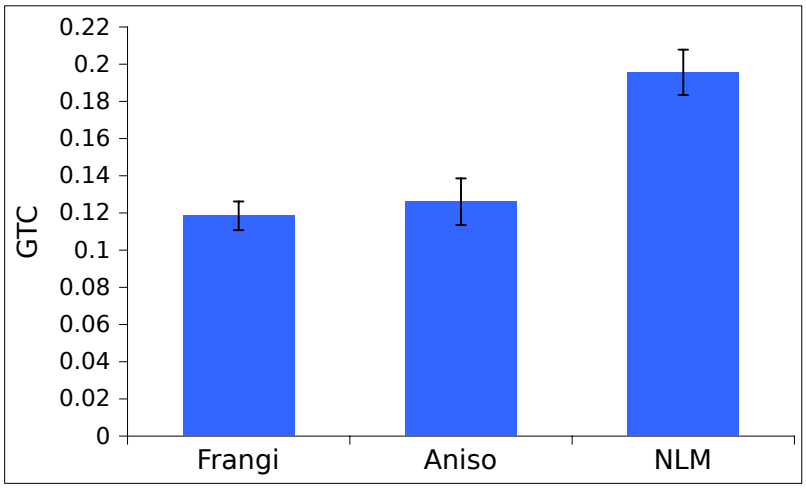

Figure 5–10: The mean and standard deviation of results from Frangi's vesselness filter (Frangi), the anisotropic vessel enhancement diffusion filter (Aniso), and the NLM vessel filter on the clinical 3D phase contrast MRA data sets.

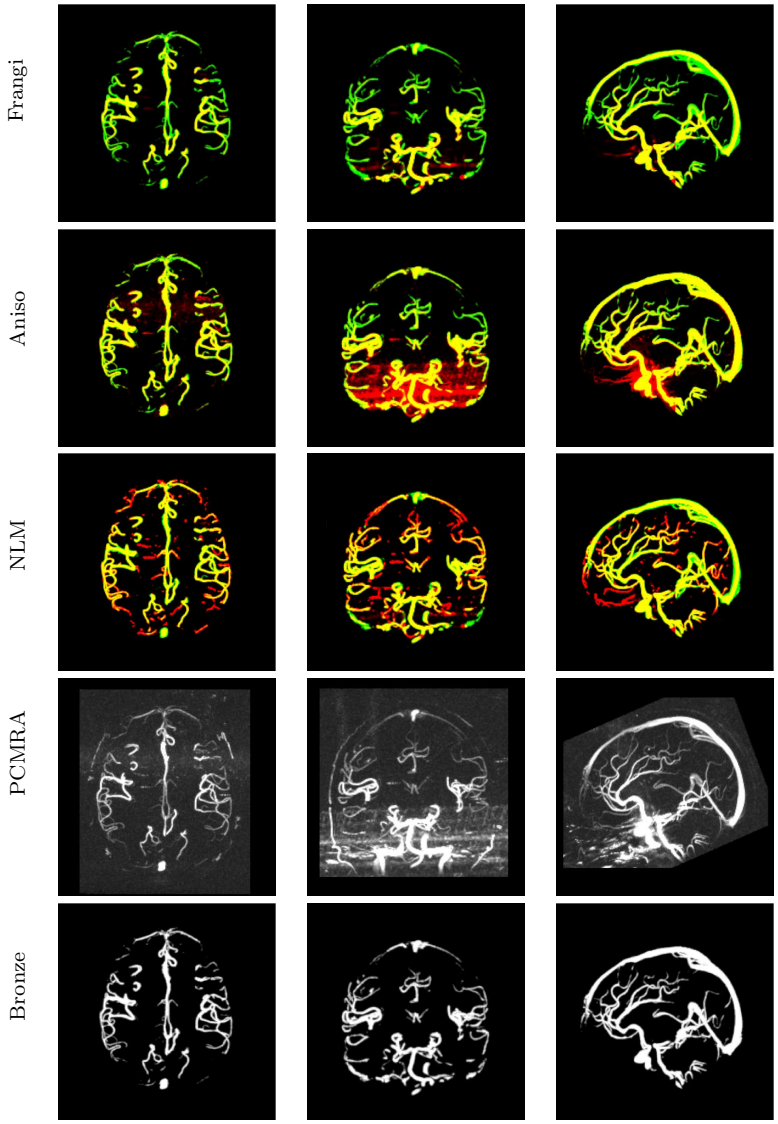

Figure 5–11: The results from one of our twenty 3D MRA enhancement tests. The vessel enhancement results (red) were overlayed over the bronze standard image (green) in transverse (left), coronal (middle), and sagittal (right) views in 31 voxel-thick slabs using maximum intensity projection. The yellow voxels show the complete intersection of the vessel enhancement results with the bronze standard image. Results of Frangi's vesselness (Frangi), the anisotropic diffusion vessel enhancement (Aniso), and the proposed NLM vessel enhancement filter (NLM) are shown. The bronze standard, which consist of manually segmented vessels (Bronze), and the original PC-MRA image without skull masking are also shown.

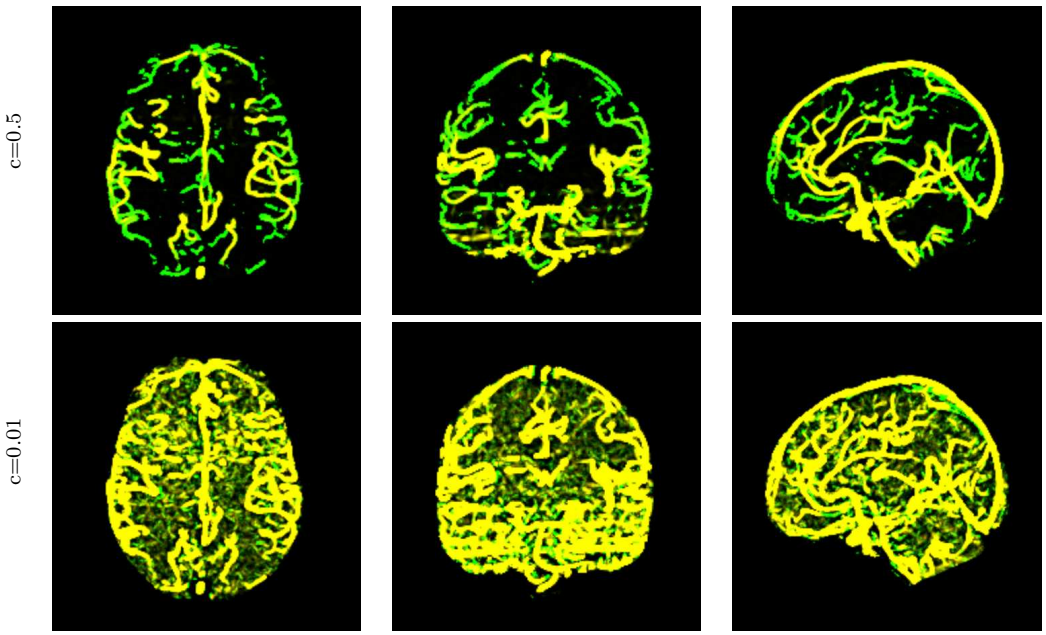

Figure 5–12: Vessel enhancements using our NLM modified filter (green) and Frangi's filter (red) in the same views as Fig 5–11. The yellow voxels show the complete intersection of Frangi's results with the NLM filter results. The NLM filter and Frangi's filter results with c tuned to the default setting of $c = 0.5\times\max(S)$ (top) and an increase sensitivity setting $c = 0.01\times\max(S)$ (bottom) are shown overlayed.

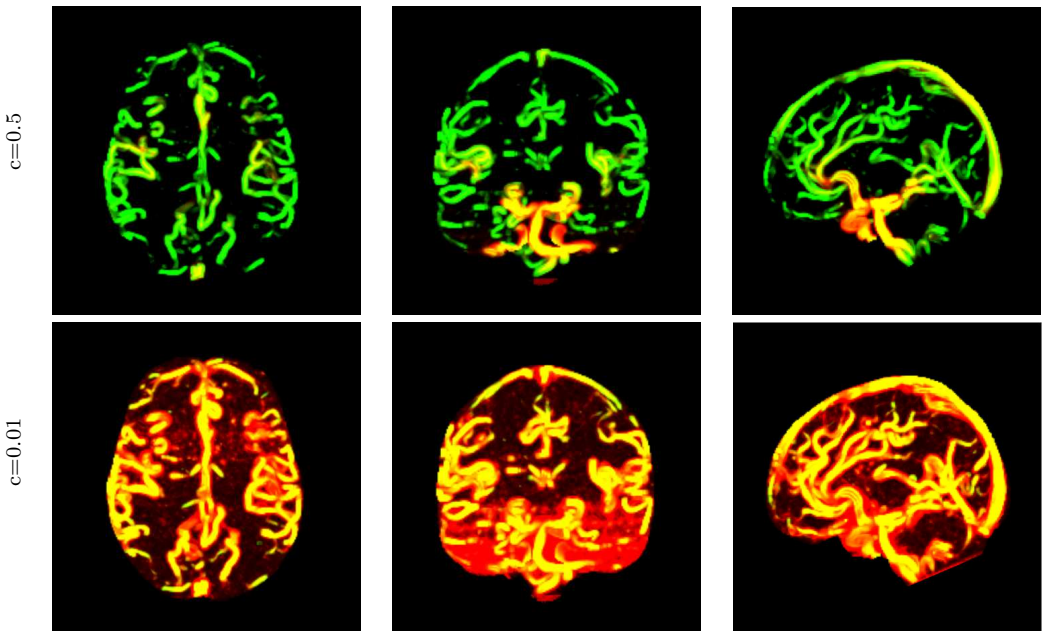

Figure 5–13: The smallest filter scale structureness map from our NLM filter (green) and Frangi's structureness (red) in the same views as Fig 5–11. Yellow voxels indicate the complete intersection of Frangi's and the NLM structureness. The images show the results with c equals to either 0.5×max(S) (c=0.5) or 0.01×max(S) (c=0.01).

CHAPTER 6
Discussion and Conclusions

The overall goal of this thesis was to create a set of techniques that would contribute to several areas of IGNS, addressing specific issues that pose challenges in the deployment and practice of computer assistance or image guidance in neurosurgery. We focused on the use of cerebrovascular information in neurosurgery and its effective integration into the image guidance framework for improved guidance and visualization. Accordingly, we developed techniques in this thesis to effectively process raw angiographic medical images and tools to validate their efficacy for use in IGNS.

6.1 Summary of Original Contributions

In observing that vessel information can be useful in intraoperative registration, we began by developing a registration method using angiographic images to robustly align a patient's pre-operative images to their intraoperative state. A successfully performed registration could correctly update the position, orientation, and deformations of the pre-operatively acquired anatomical guidance images such that they accurately represent the location and state of the patient's brain in the surgical field. Through intraoperative registration, more accurate guidance can be provided to help a surgeon during a procedure. This in turn can help reduce surgical time and the possibility of post-operative complications.

6.1.1 Vessel-based Registration

In Chapter 3, we described and validated our hybrid non-linear vessel registration algorithm for intraoperative registration of magnetic resonance (MR) and Doppler ultrasound images. The vessel structures from the MR images were enhanced using Frangi's vesselness filter [81] and vessels found in the Doppler ultrasound images were extracted using colour saturation thresholds. The vessel images then undergo multiple rounds of linear alignment and non-linear registration using the ANIMAL algorithm [47]. The recovered transforms were then modelled using thin-plate spline (TPS) transforms [68], assuring a continuous smooth deformation even with relatively sparse vessel data. The method was then validated using images from our digital US vessel simulator, a real physical phantom created by [199], and four sets of real clinical data gathered intraoperatively from patients.

One contribution in the thesis was this vessel-based registration method that is accurate and robust in presence of noise and missing vessel segments and can be used effectively under real-world clinical conditions. We also developed a technique that can simulate Doppler ultrasound vessel images from MR vessels data for the validation of inter-modality registration methods. As well, our validation work confirmed the clinical observation of Hill *et al.* [98] that significant non-linear brain-shifts do occur before dura opening.

6.1.2 Brain Phantom

Through our work in vessel-based registration and enhancement, we discovered the need for a more anatomically realistic brain phantom and thus introduced techniques to produce a physical anthropomorphic phantom for validating novel medical

image processing techniques. In Chapter 4, we described an anthropomorphic triple modality medical imaging phantom with realistic brain structures that can be effectively imaged in ultrasound, MR, and computed tomography (CT) for inter-modality validation of image processing techniques. This phantom was cast in a mold based on the digital geometric model of Holmes *et al.* [103]. It contains deep cortical features found in a human brain, and has the mechanical similarities of live brain tissue. Multiple sets of multimodality data were then acquired from this phantom.

With our novel phantom method we introduced a technique for producing anatomically accurate brain phantoms by using elastic 3D printed molds that can deform to accommodate the unmolding of topologically complex casts without damaging either the mold or casting. We also contributed a formula for phantom brain tissue that has similar mechanical properties to live human brain and also contains determined quantities of contrast agents for effective multimodal imaging. Furthermore, all our acquired phantom image data was made freely available for download by the medical image processing community. Since making this database available, we have been contacted by several research groups about using this data set for their own algorithm validations.

6.1.3 Vessel Enhancement

Our experiences from our registration work, made evident the need for an improved vessel enhancement method. The vessel enhancement results can not only be used for image preprocessing, but also they may be used by a neurosurgeon to visualize the blood vessels for surgical planning and guidance. In Chapter 5, we developed

a vessel enhancement method, which modified the Hessian eigenvalue analysis methods of Frangi [81] to improve its performance in enhancing thinner and lower contrast 2D and 3D vessel structures. We kept the two first geometric terms of the original filter method but substituted the third "structureness" term with a novel term that uses the non-local means (NLM) estimator [25] for patch-based region analysis. The NLM-based method produces a weightmap isolating voxels with similar local patches in the neighbourhood that can then be analyzed using principle component analysis (PCA) to determine if they form part of an elongated vascular structure. This analysis produces our NLM structureness map which we substituted into Frangi's method.

Our vessel enhancement work showed that by examining information from larger neighbourhood regions around a voxel we can effectively determine whether it participates in a vessel feature. We also contributed a novel method analyzing the NLM weightmap using PCA for region shape analysis. Our results showed that substituting our NLM structureness map for Frangi's structureness at the smallest scale can greatly improve the original method's ability to enhance fine and lower contrast vessel structures.

6.2 Discussion

Medical image processing using registration or enhancement and segmentation methods is necessary for many diagnostic, planning, and navigation procedures in IGNS. Due to the importance of these methods in modern neurosurgery, the development of accurate and robust image registration and enhancement methods is an

ongoing and highly active area of research. In this thesis, we presented our vessel-based image registration method, our vessel enhancement method, as well as a phantom built for validation of medical image processing methods. Although the subjects of registration, structure enhancement, and phantom development may appear related only by their common use in IGNS, the methods themselves are intimately interconnected by function.

This is particularly true for structure enhancement or segmentation methods and image registration methods. Registration and enhancement/segmentation methods both rely on slightly different aspects of the same image information, with the former aligning images based on their feature similarities, and the latter labelling features in the image based on their similarity according to a given model. The link between these two techniques has been noted in the literature, and there have been approaches proposing to combine, or "unify" registration with segmentation [9, 70, 145]. In this approach, information acquired from image segmentation provides structural features to guide accurate image registration, while a set of properly registered images in turn provides robust image information through redundancy to enhance image features for improved image segmentation. Using this strategy, the performance of each type of method may be improved.

In our work, information from image registration for image enhancement, and *vice versa*, was only used in a superficial manner. However even the interchange of information was important for the function of the image processing methods developed. In our multimodal registration method, the input images first undergo vessel

enhancement and extraction, detecting the vessel structures needed for image alignment. Our vessel enhancement method uses a non-local estimator to identify voxels with similar image regions through a registration-based similarity metric. In some ways, one can see this as using information derived from image registration to drive vessel enhancement. Ultimately, this link between both image processing schemes indicates the possibility that techniques for improving one method can be translated for improving the other and as such, warrants further exploration. More general improvements, such as computational optimizations, can also be adapted to both registration and structure enhancement methods to improve computational speeds.

The development of medical image enhancement and registration methods also necessitates the creation of devices that can be used to validate the methods' accuracy and characterize their behaviours. This led us to develop a physical anthropomorphic multimodal phantom for evaluating and testing medical image processing methods including registration, segmentation, denoising, and super-resolution methods. However, the phantom could be modified with more anatomical structures and tissues or constructed using different materials in order to improve its multimodal imaging capabilities or further extend it to other imaging modalities.

While the physical phantom is highly useful in certain applications, it may nevertheless have its limitations when very fine brain structures are needed or when one needs to rapidly include anatomical variations or tissue deformations in the phantom. We believe these challenges could be more easily addressed using digital phantoms such as that developed in our vessel registration project.

6.3 Future Work

6.3.1 Expert priors/atlases for vessel enhancement

Using the patch-based similarity matching of NLM, it may be possible to perform vessel enhancement by matching individual voxels through atlas-based label fusion. This approach of matching voxel similarities to atlas-based expert-priors for the purpose of image segmentation has been previously used by Coupé *et al.* [53] for segmentation of the human hippocampus in MR images and Eskildsen *et al.* [73] to roughly segment the human brain for skull-stripping in MR head images.

A registration based vessel structure enhancement method that uses a whole-brain probabilistic vessel atlas was proposed by Passat *et al.* [179]. This method globally registers a subject image to a probabilistic atlas through maximization of image similarity measure, and then transfers the labels to the subject voxels according to their local structures and relative locations on the atlas. Such a method depends significantly on a vessel's global position, potentially limiting the method's ability to account for variations in vessel anatomy. However, by using an atlas with NLM patches, it may be possible to find similar patches with vessels structures from different regions of the brain and transfer their labels over to properly enhance image vessels. Such a method would allow for improved enhancement in anatomies with vessel variations and provide more information redundancy to reduce the chances of mislabelling a voxel.

6.3.2 Combining vessel features

To help improve the accuracy and robustness of hybrid vessel-registration, other vessel features can be extracted and introduced on top of image intensity information

to. Vessel centerpoints, bifurcation points, or bifurcation graphs [91] can be processed and used to help align vessel structures in a non-ambiguous manner. This may be useful especially when vessel structures in the acquired images show up with different diameters due to their tuned imaging parameters. This is true in the case between MR and Doppler ultrasound angiographic images [201] where higher ultrasound gain settings may results in imaged vessels being 2-3 times the size of the same vessel acquired in MR. In our work in Chapter 3, we handled this by relying on cross-sectional intensities of the vessels in both MR and US images to assure registration success. Nevertheless, even in our method the use of other vessel features may help assure higher registration success and improve rates of registration convergence.

This strategy of using a combination of different vessel structure information can also be applied to help improve vessel enhancement. One of the ways in which sets of different vessel information can be combined is through the use of adaptive boosting methods [83] or multiple classifiers systems [100]. For instance, the use of multiple classifiers has been applied to brain segmentation by combining the output of different atlases and differently tuned atlas registration parameters [211]. In the case of vessel enhancement, different vessel information could be obtained by using kernel-based filters or extracted via skeletonization and then combined via multiple classifier techniques. If implemented correctly, a vessel enhancement method that uses several classifiers may be able to overcome the limitations of any one of its classifiers and be able to obtain more accurate and robust results.

6.3.3 Weightmap image feature analysis

The vessel-based registration and vessel enhancement methods developed here both utilize shape-based filtering to accomplish their purpose in medical image processing. However, the application of more sophisticated feature analysis methods could be used to improve the efficacy of both types of methods.

In our vessel enhancement work, we introduced and demonstrated the application of feature analysis on NLM weightmaps for the enhancement of vessel-like features. We believe that NLM weightmaps, which highlight regional voxel image structures, can be used for feature analysis and be extended to detect other types of image structures beyond simple cylindrical and line-like geometries. For instance, eigenvalues from the PCA of NLM weightmaps can be used to enhance plane-like or nodule-like geometries by taking into account different eigenvalue ratios [143, 81]. By examining the voxel's larger neighbourhood regions together with its smaller Hessian support, we may also be able to effectively enhance lower contrast sulcal or nodule features in medical images.

The voxel self-similarity information from the NLM weightmaps used in our vessel enhancement method may also be analyzed with other techniques beyond PCA. For instance, active shape models [50] could be used by training models to detect elongated line-like structures and effectively find the sometimes noisy line structures in the NLM weightmap. Similarly, one can also use regulated morphological operations to produce fuzzy sphere representations of structures in the weightmap [2], thus identifying line-like structures. It may also be possible to apply 2D curve consistency filters [273] or 3D curve inference filters [217] to NLM weightmaps to determine if

a voxel is part of an oriented curved line. When combined with our method, these sophisticated shape analysis techniques may be able to more effectively and robustly determine if given a voxel is participating in a vessel structure. For instance, preliminary results of applying 2D curve consistency filters to our method appears to help in connecting and enhancing thin and broken vessel segments in 2D angiographic images.

It may also be possible to extend weightmap feature analysis through the use of other self-similarity estimation techniques. One option is through the use of the rotation-invariant histogram earth-mover distance (EMD) technique [213]. Instead of comparing voxel patches, histograms of the local area of each voxel would be generated and the histograms' similarities used to create the voxel's weightmap. Preliminary results of applying such a technique seems to help effectively identify image features with parts in different orientations, such as a curving vessel or an organ surface.

The output of an improved vessel or sulcal feature enhancement method can perhaps also be applied to help improve the performance of image registration. While vessel structures alone are quite useful for registration due to their unique topology and features, using vessel information on its own can prove problematic in certain cases. For instance, if insufficient vessel structures are acquired in the image or if the vessels themselves cannot be properly extracted, the accuracy of a vessel-based registration method could be adversely affected. In many cases, it may be useful to also extract other image features together with vessels from the raw medical images to help improve image registration. In neurosurgery for example, sulci are readily

acquired and are highly visible features in B-mode ultrasound and MR images. Sulcal features have been shown to be feasible for use in intra-modality non-rigid registration [250] and multimodality intraoperative rigid registration [52]. Combining vascular, sulcal, or even nodule-like pathological structures for use as registration feature, can all help produce more accurate and robust algorithms for medical image registration.

6.3.4 Parallel computation

Parallel computation, either on multiple processor cores or on the graphics processing units (GPU) of modern graphics cards could be used to enhance the processing speeds of our vessel enhancement and vessel-based registration methods.

Our hybrid registration method performs in an intraoperatively feasible time of typically less than 6 minutes. Although this speed is acceptable for most surgical cases, it would be ideal if registration was done at speeds approaching real-time (around a second). Although code optimization can improve registration time, we believe that the hybrid registration algorithm should be reimplemented to use the GPU to accelerate the computational processes. GPU based rigid, affine linear, and non-linear registration methods using image feature and image intensities strategies have been previously implemented [223, 79]. The linear portions of our method should be straightforward for reimplemented for the GPU since image Gaussian blurring is implemented for all modern graphics processes, the downhill simplex algorithm used in our technique is partially parallelizable, and the cross-correlation objective function is simple to implement as single instructions on most GPU architectures [223]. The non-linear portion of our registration technique will require more involved

development, but the piece-wise linear ANIMAL algorithm appears in theory to also be parallelizable.

Our NLM-based vessel enhancement algorithm is computationally expensive. Its current implementation in MATLAB also lengthens its run-time. By optimizing the code or implementing it in a lower level language such as C or C++, the speed of this algorithm can be greatly improved. We do believe, however, that the NLM-based vessel enhancement algorithm should be implemented for parallel computing, more specifically for computation on modern GPUs. The NLM algorithm performs a large number of relatively simple image block sum-squared difference computations for an even larger number of image voxels. While this requires significant computational power, this algorithmic structure is also well suited for adaptation to GPU processing. The fact that medical image segmentation and other blocks-wise computational methods have been successfully implemented on the GPU [195] indicates that a block-wise NLM-based vessel enhancement method may be feasibly implemented for GPU processing. While it is difficult to determine exactly what speed enhancements can be expected of a GPU NLM vessel enhancement algorithm, our preliminary results using parallel for-loops in MATLAB suggests that implementing the algorithm as 4 separate parallel processing threads can improve the execution speed by more than 3 times. This suggests that the more than 100 parallel threads available from even a low-end modern GPU would provide drastic improvements to the original speed.

6.3.5 Phantom contrast agents

Although the contrast agents used for our multimodal imaging phantom can be effectively imaged, future work should be done to find better contrast agents for phantom construction. For instance, we found that our $CuSO_4$ MR contrast agents tended to diffuse out from our phantom tissue mimicking material and landmark spheres over time. This reduced the MR intensity of the cortical surface and the contrast of the spherical landmarks with the surrounding tissue material. Finding an effective non-diffusing MR contrast agent could be beneficial to MR phantom designs that use gel-like materials as tissue mimicking materials. Alternatively, diffusion can be greatly reduced or eliminated by sealing the landmark spheres with an impermeable coating. However, possible materials for such coatings would need to be explored and characterized.

In our study, we used separate contrast agents for CT and ultrasound in our phantoms. We have noticed however, through separate tests, that it may be possible to also use the CT contrast agent, $BaSO_4$, as an ultrasound back-scattering contrast agent, something that has also been observed by [49] for photoacoustic imaging. Proper evaluation and characterization of $BaSO_4$ for ultrasound imaging could provide a multimodal contrast agent for phantom fabrication, reducing the number of contrast agents and the complexity of phantom construction. If possible a non-diffusing contrast agent effective in MR, CT, and ultrasound should be found to create medical imaging phantoms for these three ubiquitous imaging modalities. While we have not seen examples of this in the literature, it may also be possible to

use $BaSO_4$ as a clinical contrast agent for ultrasound imaging of the gastrointestinal tract instead of limiting its clinical use in x-ray modalities.

6.3.6 Phantom tissue-types

The phantom proposed in this work can be improved by simulating heterogeneous brain tissues such as white matter, cortical grey matter and deep grey matter. This would allow validation of tissue segmentation methods and testing of newly developed imaging modalities. The casting of these multiple tissue layers can be done through methods similar to that of [22, 24] developed for producing multi-layered arterial flow phantoms. For instance, one could cast the white matter tissue type in a white matter mold and then place the finished cast into a grey matter mold to cast on a grey matter tissue layer. An anatomically accurate brain phantom with realistically produced tissues can be used for cortical segmentation and registration studies.

More anatomically realistic flow enabled vessel structure can also be introduced into the brain phantom by employing the lost material casting methods of [45, 5], which would allow highly accurate vessel lumen cavities to be cast into the brain phantom's tissue mimicking materials. Although the phantom of [199] included vessel structures for Doppler ultrasound registration validation, these vessels consisted of plastic tubing that were not anatomically realistic and when imaged, produced thick and high-contrast vessel walls not found in real clinical images. While the larger veins and arteries of the brain can be fabricated, the capillary bed would be more difficult to mimic.

It is also possible to simulate white matter tracts in an anthropomorphic brain phantom. This can be done by including tightly bunched synthetic fibres [188] into the tissue mimicking materials, causing water diffusion within the space between the fibres to become anisotropic and allow imaging for diffusion tensor imaging.

An area that has not been thoroughly explored for anthropomorphic brain phantoms is the inclusion of tissues for validating capillary blood perfusion. Older blood perfusion phantoms have used dialysis cartridges [252] while more recent perfusion devices have used micro-fabrication techniques to create the device's microchannels [71, 168]. If the materials, contrast agents, and fabrication techniques used to produce perfusion phantoms can be incorporated into an anthropomorphic multimodal brain phantom, the resulting brain phantom can then be used for the quantitative simulation of cerebral blood perfusion. Such a phantom could be used for the verification of cross-modality perfusion metrics and for the validation of cerebral blood perfusion based image processing techniques such as hydrodynamic segmentation [146].

6.3.7 Graphics digital phantoms

In developing our registration method, we also concurrently developed a computer graphics based Doppler ultrasound simulation phantom for registration validation, which we believe can be further improved. The phantom can be enhanced to simulate more realistic shadowing, contain better depth dependant image speckle, and allow for tunable Doppler intensity gains. Although there are first-principle physics-based methods for the simulation of Doppler ultrasound [109], these programs and algorithms are difficult to use for individuals who are not familiar with

ultrasound RF signal processing and typically take significant computational time to simulate a full 3D Doppler ultrasound image.

Computer graphics techniques described in this work can be used to create different ultrasound simulating phantoms that fulfil specific image processing validation needs. For instance, a digital phantom can be designed to produce images similar in appearance to real B-mode, Doppler, or contrast-enhanced ultrasound images for use in validating ultrasound image segmentation, denoising, or registration, with the latter being the case of our work. By using modern computer graphics hardware, computer-based phantoms could be fast enough for the simulation of realistic ultrasound images in real-time [29], and can potentially be used for validating real-time ultrasound image processing methods.

The challenge and potential issue of using non-physics-based digital phantoms is that they may not generate sufficiently accurate images to model real clinical images. If the simulated images from the digital phantom does not behave similarly to real images, the validation results of an image processing method would be inaccurate or even erroneous. Therefore, it is important to validate non-physics-based digital phantoms to demonstrate the synthetic images it generates are sufficiently similar to real ultrasound images for its intended test application. For instance, in our digital Doppler ultrasound vessel phantom, we demonstrated that the generated synthetic vessel images had highly similar registration cross-correlation curves compared to real vessel images such that it can be used for validating ultrasound to MR vessel-registration methods. Digital ultrasound phantoms based on both physics and computer graphics have been created in order to validate ultrasound denoising

methods [187]. As such, partially computer graphics-based phantoms could also be created as tools to aid evaluation of novel segmentation or registration techniques.

6.4 Conclusions

The goal of this thesis was to develop vascular image processing techniques for IGNS that are accurate and robust, as well as a device for validating the efficacy of medical image processing techniques. The vessel enhancement and vessel-based registration method described in this thesis have been extensively validated to demonstrate that they are accurate, robust, and provided improvements over previous techniques. The resulting multimodal imaging phantom realistically reproduces cerebral anatomical structures, their mechanical properties, and also provides improvements over previous brain phantoms.

We believe that the novel vessel-based image processing methods and validation devices presented in this thesis can help streamline present medical image processing workflows in surgical preparation and improve the overall accuracy and clinical outcomes of surgical procedures in IGNS. These contributions are a step towards achieving the promises of IGNS to allow precision in neurosurgery, to aid the neurosurgeon in delivering treatment, and ultimately to improve patient recovery from the prescribed surgical treatment.

References

[1] D. Adalsteinsson and J. A. Sethian. A fast level set method for propagating interfaces. *Journal of Computational Physics*, 118(2):269 – 277, 1995.

[2] G. Agam, I. Armato, S.G., and C. Wu. Vessel tree reconstruction in thoracic ct scans with application to nodule detection. *Medical Imaging, IEEE Transactions on*, 24(4):486–499, 2005.

[3] G. Agam and C. Wu. Probabilistic modeling based vessel enhancement in thoracic ct scans. In *Computer Vision and Pattern Recognition, 2005. CVPR 2005. IEEE Computer Society Conference on*, volume 2, pages 649–654, 2005.

[4] L. Allard, G. Soulez, B. Chayer, Z. Qin, D. Roy, and G. Cloutier. A multimodality vascular imaging phantom of an abdominal aortic aneurysm with a visible thrombus. *Medical Physics*, 40(6):063701, 2013.

[5] L. Allard, G. Soulez, B. Chayer, F. Treyve, Z. Qin, and G. Cloutier. Multimodality vascular imaging phantoms: A new material for the fabrication of realistic 3d vessel geometries. *Medical Physics*, 36(8):3758–3763, 2009.

[6] N. Alperin, D. N. Levin, and C. A. Pelizzari. Retrospective registration of x-ray angiograms with mr images by using vessels as intrinsic landmarks. *Journal of Magnetic Resonance Imaging*, 4(2):139–144, 1994.

[7] L. Alvarez, P. Lions, and J. Morel. Image selective smoothing and edge detection by nonlinear diffusion. ii. *SIAM Journal on Numerical Analysis*, 29(3):845–866, 1992.

[8] T. Arbel, X. Morandi, R. M. Comeau, and D. L. Collins. Automatic nonlinear MRI-ultrasound registration for the correction of intra-operative brain deformations. *Computer Aided Surgery*, 9(4):123–136, 2004.

[9] J. Ashburner and K. J. Friston. Unified segmentation. *NeuroImage*, 26(3):839 – 851, 2005.

[10] B. Aubert-Broche, A. C. Evans, and L. Collins. A new improved version of the realistic digital brain phantom. *NeuroImage*, 32(1):138 – 145, 2006.

[11] B. Aubert-Broche, M. Griffin, G. Pike, A. Evans, and D. Collins. Twenty new digital brain phantoms for creation of validation image data bases. *Medical Imaging, IEEE Transactions on*, 25(11):1410 –1416, nov. 2006.

[12] S. Aylward, E. Bullitt, S. Pizer, and D. Eberly. Intensity ridge and widths for tubular object segmentation and description. In *Mathematical Methods in Biomedical Image Analysis, 1996., Proceedings of the Workshop on*, pages 131–138, 1996.

[13] S. Aylward, J. Jomier, S. Weeks, and E. Bullitt. Registration and analysis of vascular images. *International Journal of Computer Vision*, 55(2-3):123–138, 2003.

[14] S. R. Aylward and E. Bullitt. Initialization, noise, singularities, and scale in height ridge traversal for tubular object centerline extraction. *Medical Imaging, IEEE Transactions on*, 21(2):61–75, 2002.

[15] S. R. Aylward, J. Jomier, J.-P. Guyon, and S. Weeks. Intra-operative 3d ultrasound augmentation. In *In: IEEE International Symposium on Biomedical Imaging*, pages 421–424, 2002.

[16] D. Barber, E. Oubel, A. Frangi, and D. Hose. Efficient computational fluid dynamics mesh generation by image registration. *Medical Image Analysis*, 11(6):648 – 662, 2007.

[17] P. Besl and H. McKay. A method for registration of 3-d shapes. *Pattern Analysis and Machine Intelligence, IEEE Transactions on*, 14(2):239 –256, feb 1992.

[18] A. Biesdorf, K. Rohr, D. Feng, H. von Tengg-Kobligk, F. Rengier, D. Bckler, H.-U. Kauczor, and S. Wrz. Segmentation and quantification of the aortic arch using joint 3d model-based segmentation and elastic image registration. *Medical Image Analysis*, 16(6):1187 – 1201, 2012.

[19] J. C. Blechinger, E. L. Madsen, and G. R. Frank. Tissue-mimicking gelatin–agar gels for use in magnetic resonance imaging phantoms. *Medical Physics*, 15(4):629–636, 1988.

[20] T. Boskamp, D. Rinck, F. Link, B. Kmmerlen, G. Stamm, and P. Mildenberger. New vessel analysis tool for morphometric quantification and visualization of vessels in ct and mr imaging data sets1. *Radiographics*, 24(1):287–297, 2004.

[21] N. Boussion, G. Soulez, J. A. D. Guise, M. Daronat, Z. Qin, and G. Cloutier. Geometrical accuracy and fusion of multimodal vascular images: A phantom study. *Medical Physics*, 31(6):1434–1443, 2004.

[22] J. Brunette, R. Mongrain, G. Cloutier, M. Bertrand, O. Bertrand, and J.-C. Tardif. A novel realistic three-layer phantom for intravascular ultrasound imaging. *The International Journal of Cardiovascular Imaging*, 17(5):371–381, 2001.

[23] J. Brunette, R. Mongrain, J. Laurier, R. Galaz, and J. Tardif. 3d flow study in a mildly stenotic coronary artery phantom using a whole volume PIV method. *Medical Engineering & Physics*, 30(9):1193 – 1200, 2008.

[24] J. Brunette, R. Mongrain, and J. Tardif. A realistic coronary artery phantom for particle image velocimetry. *Journal of Visualization*, 7(3):241–248, 2004.

[25] A. Buades, B. Coll, and J. Morel. A review of image denoising algorithms, with a new one. *Multiscale Modeling and Simulation*, 4(2):490–530, 2006.

[26] A. Buades, B. Coll, and J.-M. Morel. Nonlocal image and movie denoising. *International journal of computer vision*, 76(2):123–139, 2008.

[27] R. Bucholz, D. Yeh, J. Trobaugh, L. McDurmont, C. Sturm, C. Baumann, J. Henderson, A. Levy, and P. Kessman. The correction of stereotactic inaccuracy caused by brain shift using an intraoperative ultrasound device. In *CVRMed-MRCAS'97*, pages 459–466, 1997.

[28] E. Bullitt, A. Liu, S. R. Aylward, C. Coffey, J. Stone, S. K. Mukherji, K. E. Muller, and S. M. Pizer. Registration of 3d cerebral vessels with 2d digital angiograms: Clinical evaluation. *Academic Radiology*, 6(9):539 – 546, 1999.

[29] B. Burger, S. Bettinghausen, M. Radle, and J. Hesser. Real-time gpu-based ultrasound simulation using deformable mesh models. *Medical Imaging, IEEE Transactions on*, 32(3):609–618, 2013.

[30] S. Briault, Y. Xiao, L. Bailey, D. L. Collins, A. F. Sadikot, and G. B. Pike. Towards computer-assisted deep brain stimulation targeting with multiple active contacts. In *Medical Image Computing and Computer-Assisted Intervention*

MICCAI 2012, volume 7510 of *Lecture Notes in Computer Science*, pages 487–494. Springer, 2012.

[31] J. Cao and S. Rittgers. Particle motion within in vitro models of stenosed internal carotid and left anterior descending coronary arteries. *Annals of Biomedical Engineering*, 26(2):190–199, 1998.

[32] W. H. Castro, H. Halm, J. Jerosch, J. Malms, J. Steinbeck, and S. Blasius. Accuracy of pedicle screw placement in lumbar vertebrae. *Spine*, 21(11):1320–1324, 1996.

[33] F. Catt, P. Lions, J. Morel, and T. Coll. Image selective smoothing and edge detection by nonlinear diffusion. *SIAM Journal on Numerical Analysis*, 29(1):182–193, 1992.

[34] C. Caero and P. Radeva. Vesselness enhancement diffusion. *Pattern Recognition Letters*, 24(16):3141 – 3151, 2003.

[35] T. Chanwimaluang, G. Fan, and S. Fransen. Hybrid retinal image registration. *Information Technology in Biomedicine, IEEE Transactions on*, 10(1):129–142, 2006.

[36] S. Chaudhuri, S. Chatterjee, N. Katz, M. Nelson, and M. Goldbaum. Detection of blood vessels in retinal images using two-dimensional matched filters. *IEEE Transactions on medical imaging*, 8(3):263–269, 1989.

[37] L. Chen, Y. Xiang, Y. Chen, and X. Zhang. Retinal image registration using bifurcation structures. In *Image Processing (ICIP), 2011 18th IEEE International Conference on*, pages 2169–2172, 2011.

[38] S. J.-S. Chen, P. Hellier, M. Marchal, J.-Y. Gauvrit, R. Carpentier, X. Morandi, and D. L. Collins. An anthropomorphic polyvinyl alcohol brain phantom based on colin27 for use in multimodal imaging. *Medical Physics*, 39(1):554–561, 2012.

[39] S.-S. Chen, I. Reinertsen, P. Coup, C. Yan, L. Mercier, D. Del Maestro, and D. Collins. Validation of a hybrid doppler ultrasound vessel-based registration algorithm for neurosurgery. *International Journal of Computer Assisted Radiology and Surgery*, 7(5):667–685, 2012.

[40] S. Chibbaro and L. Tacconi. Image-guided microneurosurgical management of vascular lesions using navigated computed tomography angiography. an

advanced igs technology application. *The International Journal of Medical Robotics and Computer Assisted Surgery*, 2(2):161–167, 2006.

[41] K. C. Chu and B. K. Rutt. Polyvinyl alcohol cryogel: An ideal phantom material for MR studies of arterial flow and elasticity. *Magnetic Resonance in Medicine*, 37(2):314–319, 1997.

[42] A. Chung, J. Noble, and P. Summers. Vascular segmentation of phase contrast magnetic resonance angiograms based on statistical mixture modeling and local phase coherence. *Medical Imaging, IEEE Transactions on*, 23(12):1490–1507, 2004.

[43] P. Cignoni, M. Callieri, M. Corsini, M. Dellepiane, F. Ganovelli, and G. Ranzuglia. Meshlab: an open-source mesh processing tool. In *Sixth Eurographics Italian Chapter Conference*, pages 129–136, 2008.

[44] P. Cimalla, D. Graf, P. Duscha, T. Meyer, J. Ku, R. Steinmeier, E. Koch, and U. Morgenstern. Methods for determining the blood flow velocity in cerebral vessels using intraoperative indocyanine green fluorescence video angiography. In J. Sloten, P. Verdonck, M. Nyssen, and J. Haueisen, editors, *4th European Conference of the International Federation for Medical and Biological Engineering*, volume 22 of *IFMBE Proceedings*, pages 1446–1449. Springer Berlin Heidelberg, 2009.

[45] G. Cloutier, G. Soulez, S. D. Qanadli, P. Teppaz, L. Allard, Z. Qin, F. Cloutier, and L.-G. Durand. A multimodality vascular imaging phantom with fiducial markers visible in dsa, cta, mra, and ultrasound. *Medical Physics*, 31(6):1424–1433, 2004.

[46] V. Coenen, S. Dammert, M. Reinges, M. Mull, J. Gilsbach, and V. Rohde. Image-guided microneurosurgical management of small cerebral arteriovenous malformations: the value of navigated computed tomographic angiography. *Neuroradiology*, 47(1):66–72, 2005.

[47] D. Collins and A. Evans. ANIMAL: Validation and application of non-linear registration-based segmentation. *IJPRAI*, 11(8):1271–1294, 1997.

[48] R. M. Comeau, A. F. Sadikot, A. Fenster, and T. M. Peters. Intraoperative ultrasound for guidance and tissue shift correction in image-guided neurosurgery. *Medical Physics*, 27(4):787–800, 2000.

[49] J. R. Cook, R. R. Bouchard, and S. Y. Emelianov. Tissue-mimicking phantoms for photoacoustic and ultrasonic imaging. *Biomedical optics express*, 2(11):3193, 2011.

[50] T. Cootes, C. Taylor, D. Cooper, and J. Graham. Active shape models-their training and application. *Computer Vision and Image Understanding*, 61(1):38 – 59, 1995.

[51] P. Coupé, P. Hellier, X. Morandi, and C. Barillot. Probe Trajectory Interpolation for 3D Reconstruction of Freehand Ultrasound. *Medical Image Analysis*, 11(6):604–615, December 2007.

[52] P. Coupé, P. Hellier, X. Morandi, and C. Barillot. 3d rigid registration of intraoperative ultrasound and preoperative mr brain images based on hyperechogenic structures. *Journal of Biomedical Imaging*, 2012, Jan. 2012.

[53] P. Coupé, J. V. Manjón, V. Fonov, J. Pruessner, M. Robles, and D. L. Collins. Patch-based segmentation using expert priors: Application to hippocampus and ventricle segmentation. *NeuroImage*, 54(2):940954, 2011.

[54] P. Coupé, P. Yger, S. Prima, P. Hellier, C. Kervrann, and C. Barillot. An Optimized Blockwise Non Local Means Denoising Filter for 3D Magnetic Resonance Images. *IEEE Transactions on Medical Imaging*, 27(4):425–441, April 2008.

[55] W. Crum, O. Camara, and D. Hill. Generalized overlap measures for evaluation and validation in medical image analysis. *Medical Imaging, IEEE Transactions on*, 25(11):1451 –1461, nov. 2006.

[56] W. Dabrowski, J. Dunmore-Buyze, H. Cardinal, and A. Fenster. A real vessel phantom for flow imaging: 3-d doppler ultrasound of steady flow. *Ultrasound in Medicine & Biology*, 27(1):135 – 141, 2001.

[57] W. Dabrowski, J. Dunmore-Buyze, R. N. Rankin, D. W. Holdsworth, and A. Fenster. A real vessel phantom for imaging experimentation. *Medical Physics*, 24(5):687–693, 1997.

[58] F. Dachille and A. Kaufman. High-degree temporal antialiasing. In *Computer Animation 2000. Proceedings*, pages 49–54, 2000.

[59] A. Danilchenko and J. Fitzpatrick. General approach to first-order error prediction in rigid point registration. *Medical Imaging, IEEE Transactions on*, 30(3):679 –693, march 2011.

[60] C. L. de Korte, E. Cspedes, A. F. van der Steen, and C. T. Lance. Intravascular elasticity imaging using ultrasound: Feasibility studies in phantoms. *Ultrasound in Medicine & Biology*, 23(5):735 – 746, 1997.

[61] K. Deng, J. Tian, J. Zheng, X. Zhang, X. Dai, and M. Xu. Retinal fundus image registration via vascular structure graph matching. *Journal of Biomedical Imaging*, 2010:14:1–14:13, Jan. 2010.

[62] T. Deschamps and L. D. Cohen. Fast extraction of minimal paths in 3d images and applications to virtual endoscopy. *Medical Image Analysis*, 5(4):281 – 299, 2001.

[63] M. Descoteaux, L. Collins, and K. Siddiqi. A multi-scale geometric flow for segmenting vasculature in mri. In M. Sonka, I. Kakadiaris, and J. Kybic, editors, *Computer Vision and Mathematical Methods in Medical and Biomedical Image Analysis*, volume 3117 of *Lecture Notes in Computer Science*, pages 169–180. Springer Berlin Heidelberg, 2004.

[64] M. Descoteaux, L. Collins, and K. Siddiqi. A multi-scale geometric flow for segmenting vasculature in mri : Theory and validation. *Medical Image Analysis*, 12(4):497–513, August 2008.

[65] S. Ding, M. Miga, R. Thompson, and B. Dawant. Robust vessel registration and tracking of microscope video images in tumor resection neurosurgery. In *Biomedical Imaging: From Nano to Macro, 2009. ISBI '09. IEEE International Symposium on*, pages 1043–1046, 2009.

[66] S. Ding, M. Miga, R. Thompson, P. Dumpuri, A. Cao, and B. Dawant. Estimation of intra-operative brain shift using a tracked laser range scanner. In *Engineering in Medicine and Biology Society, 2007. EMBS 2007. 29th Annual International Conference of the IEEE*, pages 848–851, October 2007.

[67] F. Duboeuf, A. Bbasarab, H. Liebgott, E. Brusseau, P. Delechartre, and D. Vray. Investigation of pva cryogel young's modulus stability with time, controlled by a simple reliable technique. *Medical Physics*, 36(2):656–661, 2009.

[68] J. Duchon. Splines minimizing rotation-invariant semi-norms in sobolev spaces. In W. Schempp and K. Zeller, editors, *Constructive Theory of Functions of Several Variables*, volume 571 of *Lecture Notes in Mathematics*, pages 85–100. Springer Berlin / Heidelberg, 1977. 10.1007/BFb0086566.

[69] D. Dumont, E. Miller, J. Allen, C. Moyer, S. Hsu, and G. Trahey. Peripheral vascular arfi imaging: phantom and clinical results. In *Ultrasonics Symposium, 2005 IEEE*, volume 1, pages 605–608, 2005.

[70] E. DAgostino, F. Maes, D. Vandermeulen, and P. Suetens. A unified framework for atlas based brain image segmentation and registration. In J. Pluim, B. Likar, and F. Gerritsen, editors, *Biomedical Image Registration*, volume 4057 of *Lecture Notes in Computer Science*, pages 136–143. Springer Berlin Heidelberg, 2006.

[71] B. Ebrahimi, S. Swanson, and T. Chupp. A microfabricated phantom for quantitative mr perfusion measurements: Validation of singular value decomposition deconvolution method. *Biomedical Engineering, IEEE Transactions on*, 57(11):2730–2736, 2010.

[72] A. Enquobahrie, L. Ibanez, E. Bullitt, and S. Aylward. Vessel enhancing diffusion filter. *The Insight Journal - 2007 MICCAI Open Science Workshop*, 07 2007.

[73] S. F. Eskildsen, P. Coupé, V. Fonov, J. V. Manjón, K. K. Leung, N. Guizard, S. N. Wassef, L. R. Ostergaard, and D. L. Collins. Beast: Brain extraction based on nonlocal segmentation technique. *NeuroImage*, 59(3):2362 – 2373, 2012.

[74] A. Evans, D. Collins, S. Mills, E. Brown, R. Kelly, and T. Peters. 3d statistical neuroanatomical models from 305 mri volumes. In *Nuclear Science Symposium and Medical Imaging Conference, 1993., 1993 IEEE Conference Record.*, pages 1813 –1817 vol.3, oct-6 nov 1993.

[75] R. Fahrig, H. Nikolov, A. J. Fox, and D. W. Holdsworth. A three-dimensional cerebrovascular flow phantom. *Medical Physics*, 26(8):1589–1599, 1999.

[76] L. Fieten, K. Schmieder, M. Engelhardt, L. Pasalic, K. Radermacher, and S. Heger. Fast and accurate registration of cranial ct images with a-mode ultrasound. *International Journal of Computer Assisted Radiology and Surgery*, 4:225–237, 2009. 10.1007/s11548-009-0288-z.

[77] B. Fischl, A. Liu, and A. Dale. Automated manifold surgery: constructing geometrically accurate andtopologically correct models of the human cerebral cortex. *IEEE Transactions on Medical Imaging*, 20(1):70–80, 2001.

[78] M. A. Fischler and R. C. Bolles. Random sample consensus: a paradigm for model fitting with applications to image analysis and automated cartography. *Commun. ACM*, 24(6):381–395, June 1981.

[79] O. Fluck, C. Vetter, W. Wein, A. Kamen, B. Preim, and R. Westermann. A survey of medical image registration on graphics hardware. *Computer Methods and Programs in Biomedicine*, 104(3):e45 – e57, 2011.

[80] A. Frangi, W. Niessen, R. Hoogeveen, T. Van Walsum, and M. Viergever. Model-based quantitation of 3-d magnetic resonance angiographic images. *Medical Imaging, IEEE Transactions on*, 18(10):946–956, 1999.

[81] A. F. Frangi, W. J. Niessen, K. L. Vincken, and M. A. Viergever. Muliscale vessel enhancement filtering. In *MICCAI 1998*, pages 130–137, 1998.

[82] R. Frayne, L. M. Gowman, D. W. Rickey, D. W. Holdsworth, P. A. Picot, M. Drangova, K. C. Chu, C. B. Caldwell, A. Fenster, and B. K. Rutt. A geometrically accurate vascular phantom for comparative studies of x-ray, ultrasound, and magnetic resonance vascular imaging: construction and geometrical verification. *Medical Physics*, 20(2):415–425, 1993.

[83] Y. Freund and R. E. Schapire. A desicion-theoretic generalization of on-line learning and an application to boosting. In *Computational learning theory*, pages 23–37. Springer, 1995.

[84] J. Fromageau, J.-L. Gennisson, C. Schmitt, R. Maurice, R. Mongrain, and G. Cloutier. Estimation of polyvinyl alcohol cryogel mechanical properties with four ultrasound elastography methods and comparison with gold standard testings. *IEEE Transactions on Ultrasonics, Ferroelectrics and Frequency Control*, 54(3):498–509, 2007.

[85] R. Gan, A. Chung, W. Wong, and S. Yu. Vascular segmentation in three-dimensional rotational angiography based on maximum intensity projections. In *Biomedical Imaging: Nano to Macro, 2004. IEEE International Symposium on*, volume 1, pages 133–136, 2004.

[86] G. Gerig, O. Kubler, R. Kikinis, and F. Jolesz. Nonlinear anisotropic filtering of mri data. *IEEE Trans. Med. Imaging*, 11(2), 1992.

[87] D. G. Gobbi, R. M. Comeau, and T. M. Peters. Ultrasound probe tracking for real-time ultrasound/mri overlay and visualization of brain shift. In *Proceedings of the Second International Conference on Medical Image Computing and Computer-Assisted Intervention*, MICCAI '99, pages 920–927, London, UK, 1999. Springer-Verlag.

[88] D. G. Gobbi and T. M. Peters. Generalized 3d nonlinear transformations for medical imaging: an object-oriented implementation in VTK. *Computerized Medical Imaging and Graphics*, 27(4):255 – 265, 2003.

[89] D. C. Goldstein, H. L. Kundel, M. E. Daube-Witherspoon, L. E. Thibault, and E. J. Goldstein. A silicone gel phantom suitable for multimodality imaging. *Investigative Radiology*, 22(2):153–157, 1987.

[90] R. Greaby, V. Zderic, and S. Vaezy. Pulsatile flow phantom for ultrasound image-guided HIFU treatment of vascular injuries. *Ultrasound in Medicine & Biology*, 33(8):1269 – 1276, 2007.

[91] M. Groher, T. F. Jakobs, N. Padoy, and N. Navab. Planning and intraoperative visualization of liver catheterizations: New CTA protocol and 2d-3d registration method. *Academic Radiology*, 14(11):1325 – 1340, 2007.

[92] M. Groher, D. Zikic, and N. Navab. Deformable 2d-3d registration of vascular structures in a one view scenario. *Medical Imaging, IEEE Transactions on*, 28(6):847–860, 2009.

[93] J. L. Gunter, M. A. Bernstein, B. J. Borowski, C. P. Ward, P. J. Britson, J. P. Felmlee, N. Schuff, M. Weiner, and C. R. Jack. Measurement of mri scanner performance with the adni phantom. *Medical Physics*, 36(6):2193–2205, 2009.

[94] N. Haberland, K. Ebmeier, R. Hliscs, J. P. Grunewald, J. Silbermann, J. Steenbeck, H. Nowak, and R. Kalff. Neuronavigation in surgery of intracranial and spinal tumors. *Journal of Cancer Research and Clinical Oncology*, 126(9):529–541, Aug. 2000.

[95] S. J. Hammer, J. Dineley, W. J. Easson, and P. R. Hoskins. An arterial wall motion test phantom for the evaluation of wall motion software. *Ultrasound in Medicine & Biology*, 33(9):1504 – 1511, 2007.

[96] M. Hassouna, A. Farag, S. Hushek, and T. Moriarty. Statistical-based approach for extracting 3d blood vessels from tof-myra data. In R. Ellis and T. Peters, editors, *Medical Image Computing and Computer-Assisted Intervention - MICCAI 2003*, volume 2878 of *Lecture Notes in Computer Science*, pages 680–687. Springer Berlin Heidelberg, 2003.

[97] P. Hastreiter, C. Rezk-Salama, G. Soza, M. Bauer, G. Greiner, R. Fahlbusch, O. Ganslandt, and C. Nimsky. Strategies for brain shift evaluation. *Medical Image Analysis*, 8(4):447 – 464, 2004.

[98] D. Hill, C. Maurer, R. Maciunas, J. Barwise, J. Fitzpatrick, and M. Wang. Measurement of intraoperative brain surface deformation under a craniotomy. *Neurosurgery*, 43(3):514–528, 1998.

[99] J. Hipwell, G. Penney, R. McLaughlin, K. Rhode, P. Summers, T. Cox, J. Byrne, J. Noble, and D. Hawkes. Intensity-based 2-d - 3-d registration of cerebral angiograms. *Medical Imaging, IEEE Transactions on*, 22(11):1417–1426, 2003.

[100] T. K. Ho, J. J. Hull, and S. N. Srihari. Decision combination in multiple classifier systems. *Pattern Analysis and Machine Intelligence, IEEE Transactions on*, 16(1):66–75, 1994.

[101] E. Hoffman, P. D. Cutler, W. Digby, and J. Mazziotta. 3-d phantom to simulate cerebral blood flow and metabolic images for pet. *Nuclear Science, IEEE Transactions on*, 37(2):616–620, 1990.

[102] R. S. Holland and R. E. Kellogg. The dependence of quantum noise on screen sharpness. *Proc. SPIE*, 0096:164–171, 1976.

[103] C. Holmes, R. Hoge, L. Collins, R. Woods, A. Toga, and A. Evans. Enhancement of MR images using registration for signal averaging. *Journal of Computer Assisted Tomography*, 22(2):324, 1998.

[104] M. Holtzman-Gazit, R. Kimmel, N. Peled, and D. Goldsher. Segmentation of thin structures in volumetric medical images. *Image Processing, IEEE Transactions on*, 15(2):354–363, 2006.

[105] X. Huang, A. Abdalbari, S. Zaheer, T. Looi, J. Ren, and J. Drake. Fast deformable registration for soft organs with large motion in hifu treatment. In

Proc. SPIE 8671, Medical Imaging 2013: Image-Guided Procedures, Robotic Interventions, and Modeling, volume 8671, pages 86711J–86711J–7. SPIE, 2013.

[106] H. Imamura, N. Ida, N. Sugimoto, S. Eiho, S.-i. Urayama, K. Ueno, and K. Inoue. Registration of preoperative cta and intraoperative fluoroscopic images for assisting aortic stent grafting. In T. Dohi and R. Kikinis, editors, *Medical Image Computing and Computer-Assisted Intervention MICCAI 2002*, volume 2489 of *Lecture Notes in Computer Science*, pages 477–484. Springer Berlin Heidelberg, 2002.

[107] International Telecommunications Union. Bt.709 : Parameter values for the hdtv standards for production and international programme exchange. *International Telecommunications Union-Recommendations*, 2002.

[108] I. Isgum, M. Staring, A. Rutten, M. Prokop, M. Viergever, and B. Van Ginneken. Multi-atlas-based segmentation with local decision fusion – application to cardiac and aortic segmentation in ct scans. *Medical Imaging, IEEE Transactions on*, 28(7):1000–1010, 2009.

[109] J. Jensen. Ultrasound imaging and its modeling. In M. Fink, W. Kuperman, J.-P. Montagner, and A. Tourin, editors, *Imaging of Complex Media with Acoustic and Seismic Waves*, volume 84 of *Topics in Applied Physics*, pages 135–166. Springer Berlin Heidelberg, 2002.

[110] S. Ji, Z. Wu, A. Hartov, D. Roberts, and K. Paulsen. Mutual-information-based image to patient re-registration using intraoperative ultrasound in image-guided neurosurgery. *Medical physics*, 35:4612–4624, 2008.

[111] C. Jia, K. Kim, T. Kolias, W. Weitzel, J. Rubin, and M. O'Donnell. Left ventricular phantom with pulsatile circulation for ultrasound strain rate imaging. In *IEEE Ultrasonics Symposium*, pages 1317–1320, 2006.

[112] C.-P. Jiang. Vessel phantom fabrication using rapid prototyping technique for investigating thermal dosage profile in hifu surgery. *Rapid Prototyping Journal*, 16(6):417–423, 2010.

[113] X. Jiang and D. Mojon. Adaptive local thresholding by verification-based multithreshold probing with application to vessel detection in retinal images. *Pattern Analysis and Machine Intelligence, IEEE Transactions on*, 25(1):131–137, 2003.

[114] J. Jomier and S. R. Aylward. Rigid and deformable vasculature-to-image registration: A hierarchical approach. In C. Barillot, D. R. Haynor, and P. Hellier, editors, *Medical Image Computing and Computer-Assisted Intervention MICCAI 2004*, volume 3216 of *Lecture Notes in Computer Science*, pages 829–836. Springer Berlin / Heidelberg, 2004.

[115] W. Khaled, T. Neumann, H. Ermert, S. Reichling, A. Arnold, and O. Bruhns. Evaluation of material parameters of pva phantoms for reconstructive ultrasound elastography. *IEEE Ultrasonics Symposium*, pages 1329 –1332, 2007.

[116] M. F. Khan, K. Mewes, and O. Skrinjar. Brain shift analysis for deep brain stimulation surgery. *IEEE ISBI: Nano to Macro*, pages 654 – 657, April 2006.

[117] T. Kim, S. Joo, J. Lee, S. Jung, J. Kim, S. Kim, S. Kang, and W. Yoon. Neuronavigation-assisted surgery for distal anterior cerebral artery aneurysm. *min-Minimally Invasive Neurosurgery*, 50(03):140–144, 2007.

[118] D. M. King, A. J. Fagan, C. M. Moran, and J. E. Browne. Comparative imaging study in ultrasound, mri, ct, and dsa using a multimodality renal artery phantom. *Medical Physics*, 38(2):565–573, 2011.

[119] C. Kirbas and F. Quek. 3d wave propagation and traceback in vascular extraction. In *Engineering in Medicine and Biology, 2002. 24th Annual Conference and the Annual Fall Meeting of the Biomedical Engineering Society EMBS/BMES Conference, 2002. Proceedings of the Second Joint*, volume 2, pages 1078–1079 vol.2, 2002.

[120] C. Kirbas and F. Quek. Vessel extraction in medical images by 3d wave propagation and traceback. In *Bioinformatics and Bioengineering, 2003. Proceedings. Third IEEE Symposium on*, pages 174–181, 2003.

[121] C. Kirbas and F. Quek. A review of vessel extraction techniques and algorithms. *ACM Comput. Surv.*, 36(2):81–121, June 2004.

[122] Y. Kita, D. Wilson, and J. Noble. Real-time registration of 3d cerebral vessels to x-ray angiograms. In W. Wells, A. Colchester, and S. Delp, editors, *Medical Image Computing and Computer-Assisted Interventation MICCAI98*, volume 1496 of *Lecture Notes in Computer Science*, pages 1125–1133. Springer Berlin Heidelberg, 1998.

[123] N. Kocer, O. Kizilkilic, D. Babic, D. Ruijters, and C. Islak. Fused magnetic resonance angiography and 2d fluoroscopic visualization for endovascular intracranial neuronavigation: Technical note. *Journal of neurosurgery*, 118(5):1000–1002, 2013.

[124] T. Koller, G. Gerig, G. Szekely, and D. Dettwiler. Multiscale detection of curvilinear structures in 2-d and 3-d image data. In *Computer Vision, 1995. Proceedings., Fifth International Conference on*, pages 864–869, 1995.

[125] R. König, C. Heinen, G. Antoniadis, T. Kapapa, M. Pedro, A. Gardill, C. Wirtz, T. Kretschmer, and T. Schmidt. Image guided aneurysm surgery in a brainsuite® iomri miyabi 1.5 t environment. In *Intraoperative Imaging*, pages 107–110. Springer, 2011.

[126] K. Krissian. Flux-based anisotropic diffusion applied to enhancement of 3-d angiogram. *Medical Imaging, IEEE Transactions on*, 21(11):1440–1442, 2002.

[127] K. Krissian, G. Malandain, N. Ayache, R. Vaillant, and Y. Trousset. Model-based detection of tubular structures in 3d images. *Computer Vision and Image Understanding*, 80(2):130171, 2000.

[128] C. Lacoste, X. Descombes, and J. Zerubia. Point processes for unsupervised line network extraction in remote sensing. *IEEE Transactions on Pattern Analysis and Machine Intelligence*, 27(10):1568–1579, 2005.

[129] A. Landry and A. Fenster. Theoretical and experimental quantification of carotid plaque volume measurements made by three-dimensional ultrasound using test phantoms. *Medical Physics*, 29(10):2319–2327, 2002.

[130] T. Lange, S. Eulenstein, M. Hünerbein, and P.-M. Schlag. Vessel-based non-rigid registration of MR/CT and 3D ultrasound for navigation in liver surgery. *Computer Aided Surgery*, 8(5):228–240, 2003.

[131] T. Lange, S. Eulenstein, M. Hnerbein, H. Lamecker, and P.-M. Schlag. Augmenting intraoperative 3d ultrasound with preoperative models for navigation in liver surgery. In C. Barillot, D. Haynor, and P. Hellier, editors, *Medical Image Computing and Computer-Assisted Intervention MICCAI 2004*, volume 3217 of *Lecture Notes in Computer Science*, pages 534–541. Springer Berlin Heidelberg, 2004.

[132] M. Law and A. Chung. Three dimensional curvilinear structure detection using optimally oriented flux. In D. Forsyth, P. Torr, and A. Zisserman, editors, *Computer Vision ECCV 2008*, volume 5305 of *Lecture Notes in Computer Science*, pages 368–382. Springer Berlin Heidelberg, 2008.

[133] Y. Law, K. Johnston, H. Routh, and R. Cobbold. On the design and evaluation of a steady flow model for doppler ultrasound studies. *Ultrasound in Medicine & Biology*, 15(5):505 – 516, 1989.

[134] J. Lee, P. Beighley, E. Ritman, and N. Smith. Automatic segmentation of 3d micro-ct coronary vascular images. *Medical Image Analysis*, 11(6):630 – 647, 2007.

[135] W. R. Leo. *Techniques for nuclear and particle physics experiments: a how-to approach*. Springer, 1994.

[136] D. Lesage, E. D. Angelini, I. Bloch, and G. Funka-Lea. A review of 3d vessel lumen segmentation techniques: Models, features and extraction schemes. *Medical Image Analysis*, 13(6):819 – 845, 2009.

[137] B. Lesniak-Plewinska, M. Kowalski, S. Cygan, E. Kowalik, and K. Kaluzynski. Experimental setup with dual chamber cardiac phantom for ultrasonic elastography. *4th European Conference of the International Federation for Medical and Biological Engineering*, pages 559–562, 2009.

[138] M. M. J. Letteboer, P. W. A. Willems, M. A. Viergever, and W. J. Niessen. Brain shift estimation in image-guided neurosurgery using 3-D ultrasound. *IEEE Trans Biomed Eng*, 52(2):268–276, Feb 2005.

[139] K. Levenberg. A method for the solution of certain problems in least squares. *Quart. Applied Math.*, 2:164–168, 1944.

[140] Q. Li, S. Sone, and K. Doi. Selective enhancement filters for nodules, vessels, and airway walls in two- and three-dimensional ct scans. *Medical Physics*, 30(8):2040–2051, 2003.

[141] H. I. Litt and A. S. Brody. Baso4-loaded agarose: A construction material for multimodality imaging phantoms. *Academic Radiology*, 8(5):377–383, May 2001.

[142] A. Liu, E. Bullitt, and S. Pizer. 3d/2d registration via skeletal near projective invariance in tubular objects. In W. Wells, A. Colchester, and S. Delp, editors,

Medical Image Computing and Computer-Assisted Intervention MICCAI98, volume 1496 of *Lecture Notes in Computer Science*, pages 952–963. Springer Berlin Heidelberg, 1998.

[143] C. Lorenz, I.-C. Carlsen, T. Buzug, C. Fassnacht, and J. Weese. Multi-scale line segmentation with automatic estimation of width, contrast and tangential direction in 2d and 3d medical images. In J. Troccaz, E. Grimson, and R. Msges, editors, *CVRMed-MRCAS'97*, volume 1205 of *Lecture Notes in Computer Science*, pages 233–242. Springer Berlin Heidelberg, 1997.

[144] L. Lorigo, O. Faugeras, W. Grimson, R. Keriven, R. Kikinis, A. Nabavi, and C.-F. Westin. Curves: Curve evolution for vessel segmentation. *Medical Image Analysis*, 5(3):195 – 206, 2001.

[145] C. Lu, S. Chelikani, and J. Duncan. A unified framework for joint segmentation, nonrigid registration and tumor detection: Application to mr-guided radiotherapy. In G. Szkely and H. Hahn, editors, *Information Processing in Medical Imaging*, volume 6801 of *Lecture Notes in Computer Science*, pages 525–537. Springer Berlin Heidelberg, 2011.

[146] C.-F. Lu, W.-Y. Guo, F.-C. Chang, S.-R. Huang, Y.-C. Chou, and Y.-T. Wu. Hemodynamic segmentation of brain perfusion images with delay and dispersion effects using an expectation-maximization algorithm. *PLoS ONE*, 8(7):e68986, 07 2013.

[147] E. L. Madsen and G. D. Fullerton. Prospective tissue-mimicking materials for use in NMR imaging phantoms. *Magnetic Resonance Imaging*, 1(3):135 – 141, 1982.

[148] E. L. Madsen, J. A. Zagzebski, R. A. Banjavie, and R. E. Jutila. Tissue mimicking materials for ultrasound phantoms. *Medical Physics*, 5(5):391–394, 1978.

[149] S. Maeda, H. Kim, J. K. Tan, S. Ishikawa, S. Murakami, and T. Aoki. Nonrigid image registration method for thoracic ct images using vessel structure information. In *Systems, Man, and Cybernetics (SMC), 2012 IEEE International Conference on*, pages 1413–1417, 2012.

[150] J. V. Manjón, P. Coupé, A. A Buades, D. L. Collins, and M. A Robles. MRI Superresolution Using Self-Similarity and Image Priors. *International Journal of Biomedical Imaging*, 2010, 2010.

[151] R. Manniesing and W. Niessen. Local speed functions in level set based vessel segmentation. In C. Barillot, D. Haynor, and P. Hellier, editors, *Medical Image Computing and Computer-Assisted Intervention MICCAI 2004*, volume 3216 of *Lecture Notes in Computer Science*, pages 475–482. Springer Berlin Heidelberg, 2004.

[152] R. Manniesing, M. A. Viergever, and W. J. Niessen. Vessel enhancing diffusion: A scale space representation of vessel structures. *Medical Image Analysis*, 10(6):815 – 825, 2006.

[153] R. Manniesing, M. A. Viergever, and W. J. Niessen. Vessel axis tracking using topology constrained surface evolution. *IEEE TRANSACTIONS ON MEDICAL IMAGING*, 26(3):309–316, MARCH 2007.

[154] I. Mano, H. Goshima, M. Nambu, and M. Iio. New polyvinyl alcohol gel material for mri phantoms. *Magnetic Resonance in Medicine*, 3(6):921–926, 1986.

[155] S. Manohar, A. Kharine, J. C. G. van Hespen, W. Steenbergen, and T. G. van Leeuwen. Photoacoustic mammography laboratory prototype: imaging of breast tissue phantoms. *Journal of Biomedical Optics*, 9(6):1172–1181, 2004.

[156] Y. Masutani, T. Schiemann, and K.-H. Hhne. Vascular shape segmentation and structure extraction using a shape-based region-growing model. In W. Wells, A. Colchester, and S. Delp, editors, *Medical Image Computing and Computer-Assisted Interventation MICCAI98*, volume 1496 of *Lecture Notes in Computer Science*, pages 1242–1249. Springer Berlin Heidelberg, 1998.

[157] T. Mathiesen, I. Peredo, G. Edner, L. Kihlstrm, M. Svensson, E. Ulfarsson, and T. Andersson. Neuronavigation for arteriovenous malformation surgery by intraoperative three-dimensional ultrasound angiography. *Neurosurgery*, 60(4):345–351, 2007.

[158] J. Maurer, C.R., D. Hill, A. Martin, H. Liu, M. McCue, D. Rueckert, D. Lloret, W. Hall, R. Maxwell, D. Hawkes, and C. Truwit. Investigation of intraoperative brain deformation using a 1.5-t interventional mr system: preliminary results. *Medical Imaging, IEEE Transactions on*, 17(5):817–825, Oct. 1998.

[159] E. C. McCullough. Anthropomorphic phantoms for computed tomography scanner performance evaluation. *Journal of Computer Assisted Tomography*, 2(1), 1978.

[160] T. McInemey and D. Terzopoulos. Topology adaptive deformable surfaces for medical image volume segmentation. *Medical Imaging, IEEE Transactions on*, 18(10):840–850, 1999.

[161] H. Mehrabian and A. Samani. Constrained hyperelastic parameters reconstruction of pva (polyvinyl alcohol) phantom undergoing large deformation. *Medical Imaging 2009: Visualization, Image-Guided Procedures, and Modeling*, 7261, March 2009.

[162] D. Meier, S. Maier, and P. Bsiger. Quantitative flow measurements on phantoms and on blood vessels with mr. *Magnetic Resonance in Medicine*, 8(1):25–34, 1988.

[163] E. Meijering, W. Niessen, J. Weickert, and M. Viergever. Evaluation of diffusion techniques for improved vessel visualization and quantification in three-dimensional rotational angiography. In W. Niessen and M. Viergever, editors, *Medical Image Computing and Computer-Assisted Intervention MICCAI 2001*, volume 2208 of *Lecture Notes in Computer Science*, pages 177–185. Springer Berlin Heidelberg, 2001.

[164] C. Metz, M. Schaap, A. van der Giessen, T. van Walsum, and W. Niessen. Semi-automatic coronary artery centerline extraction in computed tomography angiography data. In *Biomedical Imaging: From Nano to Macro, 2007. ISBI 2007. 4th IEEE International Symposium on*, pages 856–859, 2007.

[165] H. Metz, J. McElhaney, and A. K. Ommaya. A comparison of the elasticity of live, dead, and fixed brain tissue. *Journal of Biomechanics*, 3(4):453 – 458, 1970.

[166] M. Miga, K. Paulsen, P. Hoopes, F. Kennedy Jr, A. Hartov, and D. Roberts. In vivo quantification of a homogeneous brain deformation model for updating preoperative images during surgery. *IEEE Transactions on Biomedical Engineering*, 47(2), 2000.

[167] J. Mille and L. Cohen. Deformable tree models for 2d and 3d branching structures extraction. In *Computer Vision and Pattern Recognition Workshops, 2009. CVPR Workshops 2009. IEEE Computer Society Conference on*, pages 149–156, 2009.

[168] J. S. Miller, K. R. Stevens, M. T. Yang, B. M. Baker, D.-H. T. Nguyen, D. M. Cohen, E. Toro, A. A. Chen, P. A. Galie, X. Yu, R. Chaturvedi, S. N. Bhatia,

and C. S. Chen. Rapid casting of patterned vascular networks for perfusable engineered three-dimensional tissues. *Nature Material*, 11(9), 2012.

[169] U. Mitrovic, Z. Spiclin, B. Likar, and F. Pernus. 3d-2d registration of cerebral angiograms: A method and evaluation on clinical images. *Medical Imaging, IEEE Transactions on*, PP(99):1–1, 2013.

[170] S. Mollus, J. Lbke, A. J. Walczuch, H. Schumann, and J. Weese. Model-to-image based 2d-3d registration of angiographic data. In J. Reinhardt and J. Pluim, editors, *Proc. SPIE 6914, Medical Imaging 2008: Image Processing*, volume 6914, pages 69142S–69142S–12. SPIE, 2008.

[171] A. Nabavi, P. McL. Black, D. T. Gering, C.-F. Westin, V. Mehta, R. S. J. Pergolizzi, M. Ferrant, S. K. Warfield, N. Hata, R. B. Schwartz, W. M. I. Wells, R. Kikinis, and F. A. Jolesz. Serial intraoperative magnetic resonance imaging of brain shift. *Neurosurgery*, 48(4):787–798, April 2001.

[172] S. Nakajima, H. Atsumi, R. Kikinis, T. M. Moriarty, D. C. Metcalf, F. A. Jolesz, and P. M. Black. Use of cortical surface vessel registration for image-guided neurosurgery. *Neurosurgery*, 40(6):1201–1210, 1997.

[173] J. A. Nelder and R. Mead. A simplex method for function minimization. *The Computer Journal*, 7(4):308–313, 1965.

[174] O. G. Nimsky, P. Hastreiter, and R. Fahlbusch. Intraoperative compensation for brain shift. *Surgical Neurology*, 10:357365, 2001.

[175] T. O'Donnell, M.-P. Jolly, and A. Gupta. A cooperative framework for segmentation using 2d active contours and 3d hybrid models as applied to branching cylindrical structures. In *Computer Vision, 1998. Sixth International Conference on*, pages 454–459, 1998.

[176] M. M. Orkisz, C. Bresson, I. E. Magnin, O. Champin, and P. C. Douek. Improved vessel visualization in mr angiography by nonlinear anisotropic filtering. *Magnetic Resonance in Medicine*, 37(6):914–919, 1997.

[177] K. Palgyi and A. Kuba. A 3d 6-subiteration thinning algorithm for extracting medial lines. *Pattern Recognition Letters*, 19(7):613 – 627, 1998.

[178] S. L. Parker, M. J. McGirt, S. H. Farber, A. G. Amin, A.-M. Rick, I. Suk, A. Bydon, D. M. Sciubba, J.-P. Wolinsky, Z. L. Gokaslan, et al. Accuracy of

free-hand pedicle screws in the thoracic and lumbar spine: analysis of 6816 consecutive screws. *Neurosurgery*, 68(1):170–178, 2011.

[179] N. Passat, C. Ronse, J. Baruthio, J.-P. Armspach, and C. Maillot. Magnetic resonance angiography: From anatomical knowledge modeling to vessel segmentation. *Medical Image Analysis*, 10(2):259 – 274, 2006.

[180] A. H. Payne, K. C. Goodrich, E. G. Kholmovski, R. B. Roemer, and D. L. Parker. Isolated kidney phantom for development of biothermal vascular models with application to high intensity focused ultrasound therapy. *Medical Physics*, 35(10):4426–4434, 2008.

[181] G. P. Penney, J. M. Blackall, M. S. Hamady, T. Sabharwal, A. Adam, and D. J. Hawkes. Registration of freehand 3d ultrasound and magnetic resonance liver images. *Medical Image Analysis*, 8(1):81–91, Mar 2004.

[182] G. P. Penney, J. Weese, J. A. Little, P. Desmedt, D. L. Hill, et al. A comparison of similarity measures for use in 2-d-3-d medical image registration. *Medical Imaging, IEEE Transactions on*, 17(4):586–595, 1998.

[183] N. A. Peppas. Turbidimetric studies of aqueous poly(vinyl alcohol) solutions. *Die Makromolekulare Chemie*, 176(11):3433–3440, 1975.

[184] N. A. Peppas and S. R. Stauffer. Reinforced uncrosslinked poly (vinyl alcohol) gels produced by cyclic freezing-thawing processes: a short review. *Journal of Controlled Release*, 16(3):305–310, 1991.

[185] K. Perlin. Improving noise. In *SIGGRAPH '02: Proceedings of the 29th annual conference on Computer graphics and interactive techniques*, pages 681–682, New York, NY, USA, 2002. ACM.

[186] P. Perona and J. Malik. Scale-space and edge detection using anisotropic diffusion. *Pattern Analysis and Machine Intelligence, IEEE Transactions on*, 12(7):629–639, 1990.

[187] C. Perreault and M.-F. Auclair-Fortier. Speckle simulation based on b-mode echographic image acquisition model. In *Computer and Robot Vision, 2007. CRV '07. Fourth Canadian Conference on*, pages 379–386, 2007.

[188] M. Perrin, C. Poupon, B. Rieul, P. Leroux, A. Constantinesco, J.-F. Mangin, and D. LeBihan. Validation of q-ball imaging with a diffusion fibre-crossing

phantom on a clinical scanner. *Philosophical Transactions of the Royal Society B: Biological Sciences*, 360(1457):881–891, 2005.

[189] A. Pizurica and W. Philips. Estimating the probability of the presence of a signal of interest in multiresolution single- and multiband image denoising. *Image Processing, IEEE Transactions on*, 15(3):654–665, March 2006.

[190] J. Pluim, J. Maintz, and M. Viergever. Mutual-information-based registration of medical images: a survey. *Medical Imaging, IEEE Transactions on*, 22(8):986 –1004, aug. 2003.

[191] T. L. Poepping, H. N. Nikolov, M. L. Thorne, and D. W. Holdsworth. A thin-walled carotid vessel phantom for doppler ultrasound flow studies. *Ultrasound in Medicine & Biology*, 30(8):1067 – 1078, 2004.

[192] R. Poli and G. Valli. An algorithm for real-time vessel enhancement and detection. *Computer Methods and Programs in Biomedicine*, 52(1):1 – 22, 1997.

[193] B. Porter, D. Rubens, J. Strang, J. Smith, S. Totterman, and K. Parker. Three-dimensional registration and fusion of ultrasound and mri using major vessels as fiducial markers. *Medical Imaging, IEEE Transactions on*, 20(4):354–359, 2001.

[194] K. Potter, C. Reed, D. Green, G. Hankey, and L. Arnolda. Ultrasound settings significantly alter arterial lumen and wall thickness measurements. *Cardiovascular Ultrasound*, 6(1):6, 2008.

[195] G. Pratx and L. Xing. Gpu computing in medical physics: A review. *Medical Physics*, 38(5):2685–2697, 2011.

[196] C. Pudney. Distance-ordered homotopic thinning: A skeletonization algorithm for 3d digital images. *Computer Vision and Image Understanding*, 72(3):404 – 413, 1998.

[197] F. Quek and C. Kirbas. Simulated wave propagation and traceback in vascular extraction. In *Medical Imaging and Augmented Reality, 2001. Proceedings. International Workshop on*, pages 229–234, 2001.

[198] A. Raabe, J. Beck, S. Rohde, J. Berkefeld, and V. Seifert. Three-dimensional rotational angiography guidance for aneurysm surgery. *Journal of neurosurgery*, 105(3):406–411, 2006.

[199] I. Reinertsen and D. L. Collins. A realistic phantom for brain-shift simulations. *Medical Physics*, 33(9):3234–3240, 2006.

[200] I. Reinertsen, M. Descoteaux, S. Drouin, K. Siddiqi, and D. Collins. Vessel driven correction of brain shift. In C. Barillot, D. Haynor, and P. Hellier, editors, *Medical Image Computing and Computer-Assisted Intervention MICCAI 2004*, volume 3217 of *Lecture Notes in Computer Science*, pages 208–216. Springer Berlin Heidelberg, 2004.

[201] I. Reinertsen, M. Descoteaux, K. Siddiqi, and D. Collins. Validation of vessel-based registration for correction of brain shift. *Medical Image Analysis*, 11(4):374 – 388, 2007.

[202] I. Reinertsen, F. Lindseth, G. Unsgaard, and D. Collins. Clinical validation of vessel-based registration for correction of brain-shift. *Medical Image Analysis*, 11(6):673–684, Dec. 2007.

[203] M. H. T. Reinges, H.-H. Nguyen, T. Krings, B.-O. Htter, V. Rohde, and J. M. Gilsbach. Course of brain shift during microsurgical resection of supratentorial cerebral lesions: limits of conventional neuronavigation. *Acta Neurochirurgica*, 146(4):369–377, Apr. 2004.

[204] C. P. Renaudin, B. Barbier, R. Roriz, D. Revel, and M. Amiel. Coronary arteries: new design for three-dimensional arterial phantoms. *Radiology*, 190(2):579–582, 1994.

[205] J. R. Rice, R. H. Milbrandt, E. L. Madsen, G. R. Frank, E. J. Boote, and J. C. Blechinger. Anthropomorphic [sup 1]h mrs head phantom. *Medical Physics*, 25(7):1145–1156, 1998.

[206] D. Rickey, P. Picot, D. Christopher, and A. Fenster. A wall-less vessel phantom for doppler ultrasound studies. *Ultrasound in Medicine & Biology*, 21(9):1163 – 1176, 1995.

[207] D. Roberts, M. Miga, A. Hartov, S. Eisner, J. Lemery, F. Kennedy, and K. Paulsen. Intraoperative brain shift and deformation: a quantitative analysis of cortical displacement in 28 cases. *Neurosurgery*, 43(5):749760, 1998.

[208] A. Roche, X. Pennec, G. Malandain, and N. Ayache. Rigid registration of 3-D ultrasound with mr images: a new approach combining intensity and gradient information. *IEEE TMI*, 20(10):1038–1049, 2001.

[209] M. Rochery, I. Jermyn, and J. Zerubia. Higher order active contours. *International Journal of Computer Vision*, 69(1):27–42, 2006.

[210] V. Rohde, P. Spangenberg, L. Mayfrank, M. Reinges, J. Gilsbach, and V. Coenen. Advanced neuronavigation in skull base tumors and vascular lesions. *min-Minimally Invasive Neurosurgery*, 48(01):13–18, 2005.

[211] T. Rohlfing and C. R. M. Jr. Multi-classifier framework for atlas-based image segmentation. *IEEE Pattern Recognition Letters*, 26(13):2070 – 2079, 2005.

[212] K. Rossmann, A. G. Haus, and G. D. Dobben. Improvement in the image quality of cerebral angiograms. *Radiology*, 96(2):361–366, 1970.

[213] Y. Rubner, C. Tomasi, and L. Guibas. A metric for distributions with applications to image databases. In *Computer Vision, 1998. Sixth International Conference on*, pages 59–66, 1998.

[214] D. Rueckert, L. I. Sonoda, C. Hayes, D. L. G. Hill, M. O. Leach, and D. Hawkes. Nonrigid registration using free-form deformations: application to breast mr images. *Medical Imaging, IEEE Transactions on*, 18(8):712–721, 1999.

[215] T. Sandor and P. Nott. Effect of radiographic magnification on image contrast of blood vessels. *American Journal of Roentgenology*, 134(1):159–192, 1980.

[216] Y. Sato, S. Nakajima, N. Shiraga, H. Atsumi, S. Yoshida, T. Koller, G. Gerig, and R. Kikinis. 3d multi-scale line filter for segmentation and visualization of curvilinear structures in medical images. *Med. Image Anal.*, 2:143168, 1998.

[217] P. Savadjiev, J. S. Campbell, G. B. Pike, and K. Siddiqi. 3d curve inference for diffusion MRI regularization and fibre tractography. *Medical Image Analysis*, 10(5):799 – 813, 2006.

[218] M. J. N. C. Schulten-Wijman, P. C. Struijk, C. Brezinka, N. De Jong, and E. A. P. Steegers. Evaluation of volume vascularization index and flow index: a phantom study. *Ultrasound in Obstetrics and Gynecology*, 32(4):560–564, 2008.

[219] Sekisui Specialty Chemicals. *Celvol Polyvinyl Alcohol... Solution Preparation Guidelines*. Sekisui Specialty Chemicals U.S., 1603 West LBJ Freeway, Dallas, TX, 2009.

[220] J. A. Sethian. A fast marching level set method for monotonically advancing fronts. *Proceedings of the National Academy of Sciences*, 93(4):1591–1595, 1996.

[221] R. Shamir, L. Joskowicz, S. Spektor, and Y. Shoshan. Localization and registration accuracy in image guided neurosurgery: a clinical study. *International Journal of Computer Assisted Radiology and Surgery*, 4:45–52, 2009. 10.1007/s11548-008-0268-8.

[222] R. R. Shamir and L. Joskowicz. Geometrical analysis of registration errors in point-based rigid-body registration using invariants. *Medical Image Analysis*, 15(1):85 – 95, 2011.

[223] R. Shams, P. Sadeghi, R. Kennedy, and R. Hartley. A survey of medical image registration on multicore and the gpu. *Signal Processing Magazine, IEEE*, 27(2):50–60, 2010.

[224] S. Sherebrin, A. Fenster, R. N. Rankin, and D. Spence. Freehand three-dimensional ultrasound: implementation and applications. In *Proc. SPIE 2708, 296*, 1996.

[225] H. Shikata, E. A. Hoffman, and M. Sonka. Automated segmentation of pulmonary vascular tree from 3d ct images. *Proc. SPIE 5369, Medical Imaging 2004*, pages 107–116, 2004.

[226] H. Shikata, G. McLennan, E. A. Hoffman, and M. Sonka. Segmentation of pulmonary vascular trees from thoracic 3d ct images. *Journal of Biomedical Imaging*, 2009:24:1–24:11, Jan. 2009.

[227] K. Siddiqi, S. Bouix, A. Tannenbaum, and S. Zucker. Hamilton-jacobi skeletons. *International Journal of Computer Vision*, 48(3):215–231, 2002.

[228] P. J. Slomka, J. Mandel, D. Downey, and A. Fenster. Evaluation of voxel-based registration of 3-d power doppler ultrasound and 3-d magnetic resonance angiographic images of carotid arteries. *Ultrasound in Medicine & Biology*, 27(7):945 – 955, 2001.

[229] R. F. Smith, R. Frayne, M. Moreau, B. K. Rutt, A. Fenster, and D. W. Holdsworth. Stenosed anthropomorphic vascular phantoms for digital subtraction angiography, magnetic resonance, and doppler ultrasound investigations.

In *Proc. SPIE 2163, Medical Imaging 1994: Physics of Medical Imaging*, volume 235, pages 235–242. SPIE, 1994.

[230] R. F. Smith, B. K. Rutt, A. J. Fox, and R. N. Rankin. Geometric characterization of stenosed human carotid arteries. *Academic Radiology*, 3(11):898 – 911, 1996.

[231] R. F. Smith, B. K. Rutt, and D. W. Holdsworth. Anthropomorphic carotid bifurcation phantom for mri applications. *Journal of Magnetic Resonance Imaging*, 10(4):533–544, 1999.

[232] S. M. Smith. Fast robust automated brain extraction. *Human Brain Mapping*, 17(3):143–155, 2002.

[233] O. V. Solberg, F. Lindseth, H. Torp, R. E. Blake, and T. A. N. Hernes. Freehand 3d ultrasound reconstruction algorithms–a review. *Ultrasound in Medicine & Biology*, 33(7):991 – 1009, 2007.

[234] A. F. Sol, A. Lpez, and G. Sapiro. Crease enhancement diffusion. *Computer Vision and Image Understanding*, 84(2):241 – 248, 2001.

[235] J. Staal, M. Abramoff, M. Niemeijer, M. Viergever, and B. van Ginneken. Ridge-based vessel segmentation in color images of the retina. *Medical Imaging, IEEE Transactions on*, 23(4):501–509, 2004.

[236] S. R. Stauffer and N. A. Peppas. Poly (vinyl alcohol) hydrogels prepared by freezing-thawing cyclic processing. *Polymer*, 33(18):3932–3936, 1992.

[237] T. Sugahara, Y. Korogi, T. Hirai, Y. Shigematu, Y. Ushio, and M. Takahashi. Contrast-enhanced t1-weighted three-dimensional gradient-echo mr imaging of the whole spine for intradural tumor dissemination. *American Journal of Neuroradiology*, 19(9):1773–9, 1998.

[238] A. Sulaiman, L. Boussel, F. Taconnet, J. M. Serfaty, H. Alsaid, C. Attia, L. Huet, and P. Douek. In vitro non-rigid life-size model of aortic arch aneurysm for endovascular prosthesis assessment. *European Journal of Cardio-Thoracic Surgery*, 33(1):53–57, 2008.

[239] Z. Sun and C. Ferris. Optimal scanning protocol of multislice CT virtual intravascular endoscopy in pre-aortic stent grafting: In vitro phantom study. *European Journal of Radiology*, 58(2):310 – 316, 2006. ¡ce:title¿Liver Lesions¡/ce:title¿.

[240] K. J. M. Surry, H. J. B. Austin, A. Fenster, and T. M. Peters. Poly(vinyl alcohol) cryogel phantoms for use in ultrasound and mr imaging. *Physics in Medicine and Biology*, 49(24):5529–5546, 2004.

[241] K. J. M. Surry, W. L. Smith, L. J. Campbell, G. R. Mills, D. B. Downey, and A. Fenster. The development and evaluation of a three-dimensional ultrasound-guided breast biopsy apparatus. *Medical Image Analysis*, 6(3):301–312, Sept. 2002.

[242] O. Tankyevych, H. Talbot, and P. Dokladal. Curvilinear morpho-hessian filter. In *Biomedical Imaging: From Nano to Macro, 2008. ISBI 2008. 5th IEEE International Symposium on*, pages 1011–1014, 2008.

[243] M. Tashiro, S. Minohara, T. Kanai, K. Yusa, H. Sakurai, and T. Nakano. Three-dimensional velocity mapping of lung motion using vessel bifurcation pattern matching. *Medical Physics*, 33(6):1747–1757, 2006.

[244] C. J. Teirlinck, R. A. Bezemer, C. Kollmann, J. Lubbers, P. R. Hoskins, P. Fish, K.-E. Fredfeldt, and U. G. Schaarschmidt. Development of an example flow test object and comparison of five of these test objects, constructed in various laboratories. *Ultrasonics*, 36(15):653–660, 1998.

[245] Y. Thakur, H. N. Nikolov, I. B. Gulka, D. W. Holdsworth, and M. Drangova. Design and construction of a multipath vessel phantom for interventional training. *British Journal of Radiology*, 83(995):979–982, 2010.

[246] R. Toledo, X. Orriols, X. Binefa, P. Radeva, J. Vitria, and J. Villanueva. Tracking elongated structures using statistical snakes. In *Computer Vision and Pattern Recognition, 2000. Proceedings. IEEE Conference on*, volume 1, pages 157–162, 2000.

[247] P. T. H. Truc, M. A. U. Khan, Y.-K. Lee, S. Lee, and T.-S. Kim. Vessel enhancement filter using directional filter bank. *Comput. Vis. Image Underst.*, 113(1):101–112, Jan. 2009.

[248] G.-A. Turgeon, G. Lehmann, G. Guiraudon, M. Drangova, D. Holdsworth, and T. Peters. 2d-3d registration of coronary angiograms for cardiac procedure planning and guidance. *Medical Physics*, 32(12):3737–3749, 2005.

[249] G. Unsgaard, S. Ommedal, O. M. Rygh, and F. Lindseth. Operation of arteriovenous malformations assisted by stereoscopic navigation-controlled display

of preoperative magnetic resonance angiography and intraoperative ultrasound angiography. *Neurosurgery*, 56(4):281–290, 2005.

[250] M. Vaillant and C. Davatzikos. Mapping the cerebral sulci: Application to morphological analysis of the cortex and to non-rigid registration. In J. Duncan and G. Gindi, editors, *Information Processing in Medical Imaging*, volume 1230 of *Lecture Notes in Computer Science*, pages 141–154. Springer Berlin Heidelberg, 1997.

[251] A. Vasilevskiy and K. Siddiqi. Flux maximizing geometric flows. *Pattern Analysis and Machine Intelligence, IEEE Transactions on*, 24(12):1565–1578, 2002.

[252] C. Veltmann, S. Lohmaier, T. Schlosser, S. Shai, A. Ehlgen, C. Pohl, H. Becher, and K. Tiemann. On the design of a capillary flow phantom for the evaluation of ultrasound contrast agents at very low flow velocities. *Ultrasound in Medicine & Biology*, 28(5):625 – 634, 2002.

[253] E. Walsh and A. Schettini. Calculation of brain elastic parameters in vivo. *American Journal of Physiology- Regulatory, Integrative and Comparative Physiology*, 247(4):693, 1984.

[254] D. J. Warren, N. Hoggard, L. Walton, M. W. R. Radatz, A. A. Kemeny, D. M. C. Forster, I. D. Wilkinson, and P. D. Griffiths. Cerebral arteriovenous malformations: comparison of novel magnetic resonance angiographic techniques and conventional catheter angiography. *Neurosurgery*, 48(5):973–983, 2001.

[255] J. Weickert. Theoretical foundations of anisotropic diffusion in image processing. In W. Kropatsch, R. Klette, F. Solina, and R. Albrecht, editors, *Theoretical Foundations of Computer Vision*, volume 11 of *Computing Supplement*, pages 221–236. Springer Vienna, 1996.

[256] C.-F. Westin, L. Wigstrm, T. Loock, L. Sjqvist, R. Kikinis, and H. Knutsson. Three-dimensional adaptive filtering in magnetic resonance angiography. *Journal of Magnetic Resonance Imaging*, 14(1):63–71, 2001.

[257] M. Wilkinson and M. Westenberg. Shape preserving filament enhancement filtering. In W. Niessen and M. Viergever, editors, *Medical Image Computing and Computer-Assisted Intervention MICCAI 2001*, volume 2208 of *Lecture Notes in Computer Science*, pages 770–777. Springer Berlin Heidelberg, 2001.

[258] P. W. Willems, T. Van Walsum, P. A. Woerdeman, E. B. Van De Kraats, G. A. De Kort, W. J. Niessen, and J. W. B. Van Der Sprenkel. Image-guided vascular neurosurgery based on three-dimensional rotational angiography: Technical note. *Journal of neurosurgery*, 106(3):501–506, 2007.

[259] D. Wilson and J. Noble. An adaptive segmentation algorithm for time-of-flight mra data. *Medical Imaging, IEEE Transactions on*, 18(10):938–945, 1999.

[260] R. J. Winder, Z. Sun, B. Kelly, P. K. Ellis, and D. Hirst. Abdominal aortic aneurysm and stent graft phantom manufactured by medical rapid prototyping. *Journal of Medical Engineering & Technology*, 26(2):75–78, 2002.

[261] O. Wink, W. Niessen, and M. Viergever. Multiscale vessel tracking. *Medical Imaging, IEEE Transactions on*, 23(1):130–133, 2004.

[262] S. W. Wise, K. D. Hopper, T. A. Schwartz, T. R. Ten Have, and C. J. Kasales. Technical factors of ct angiography studied with a carotid artery phantom. *American Journal of Neuroradiology*, 18(3):401–8, 1997.

[263] X. Wu. An efficient antialiasing technique. *ACM SIGGRAPH Computer Graphics*, 25(4):143–152, 1991.

[264] C. Yan, B. Goulet, J. Pelletier, S.-S. Chen, D. Tampieri, and D. Collins. Towards accurate, robust and practical ultrasound-ct registration of vertebrae for image-guided spine surgery. *International Journal of Computer Assisted Radiology and Surgery*, 6(4):523–537, 2011.

[265] P. Yan and A. A. Kassim. Segmentation of volumetric MRA images by using capillary active contour. *Medical Image Analysis*, 10(3):317 – 329, 2006.

[266] Y. Yang, A. Tannenbaum, and D. Giddens. Knowledge-based 3d segmentation and reconstruction of coronary arteries using ct images. In *Engineering in Medicine and Biology Society, 2004. IEMBS '04. 26th Annual International Conference of the IEEE*, volume 1, pages 1664–1666, 2004.

[267] P. Yim, J. Cebral, R. Mullick, H. Marcos, and P. Choyke. Vessel surface reconstruction with a tubular deformable model. *Medical Imaging, IEEE Transactions on*, 20(12):1411–1421, 2001.

[268] P. J. Yim, M. Kayton, W. Miller, S. Libutti, and P. L. Choyke. Automated detection of blood vessels using dynamic programming. *Pattern Recognition Letters*, 24(14):2471 – 2478, 2003.

[269] Y. Yuan, Y. Luo, and A. Chung. Ve-lli-vo: Vessel enhancement using local line integrals and variational optimization. *Image Processing, IEEE Transactions on*, 20(7):1912 –1924, July 2011.

[270] F. Zana and J.-C. Klein. Segmentation of vessel-like patterns using mathematical morphology and curvature evaluation. *Image Processing, IEEE Transactions on*, 10(7):1010–1019, 2001.

[271] D. Zhang, L. Risser, O. Friman, C. Metz, L. Neefjes, N. Mollet, W. Niessen, and D. Rueckert. Nonrigid registration and template matching for coronary motion modeling from 4d cta. In B. Fischer, B. Dawant, and C. Lorenz, editors, *Biomedical Image Registration*, volume 6204 of *Lecture Notes in Computer Science*, pages 210–221. Springer Berlin Heidelberg, 2010.

[272] D. Zikic, M. Groher, A. Khamene, and N. Navab. Deformable registration of 3d vessel structures to a single projection image. In J. Reinhardt and J. Pluim, editors, *Proc. SPIE 6914, Medical Imaging 2008: Image Processing*, volume 6914, page 69146937. SPIE, 2008.

[273] S. W. Zucker. Early orientation selection: Tangent fields and the dimensionality of their support. *Computer Vision, Graphics, and Image Processing*, 32(1):74 – 103, 1985.